DTU Electrical Engineering
Department of Electrical Engineering

Degradation Rates of Photovoltaic Plants in Northern Latitudes

Master Thesis

By: Raúl Alcácer Galán

Degradation Rates of Photovoltaic Plants in Northern Latitudes

Master Thesis
March 6, 2023

By
Raúl Alcácer Galán

Published by: DTU, Department of Electrical Engineering, Ørsteds Plads Building 348, 2800 Kgs. Lyngby Denmark
www.elektro.dtu.dk/

Approval

This thesis has been prepared over five months at the Department of Electrical Engineering, at the Technical University of Denmark, DTU, in partial fulfilment for the degree Master in Sustainable Energy.

It is assumed that the reader has a basic knowledge of the solar energy field.

Raúl Alcácer Galán - s212748

.....

Signature

.....

Date

Abstract

The degradation rate plays an essential role in predicting and assessing the long-term energy generation of photovoltaic (PV) systems. Although there is a wide literature on the topic, the precise rate at which PV plants degrade is not trivial to predict because it is influenced by numerous factors. Also, there is not as much information regarding bifacial modules due to their recent introduction into the market. In this thesis, the long-term monitoring data of two different PV systems in northern latitudes are analyzed to gain insight into the degradation rate of their performance over time. The main degradation modes and sources of uncertainty are first discussed. Then, measurements from on-site sensors and other modelled parameters are filtered, and the Year on Year methodology is applied to both systems. System A is a 13.1 MWp PV plant located in England with fixed-tilt monofacial modules, while System B is a 236.3 kWp PV plant in Denmark with different string mounting orientations (fixed-tilt/ tracker) and bill of materials (monofacial/bifacial). It is found that the median degradation rate for System A is -0.46 %/year and for System B is -0.65 %/year, which is in line with historical and recent findings. A comparison between the degradation rates of different strings in System B is also presented. Additionally, visual inspection, flash tests, and electroluminescence (EL) imaging were performed to validate the degradation rate calculated with field data and identify the degradation modes that significantly impact the performance loss. All in all, this research provides valuable information for understanding the long-term performance of different system configurations and helps identify the main degradation causes.

Acknowledgements

I would like to thank my parents Raúl and Nuria, and my sister Laura, whose unconditional support despite the distance has helped me overcome any circumstances. I especially dedicate to them this project that marks the culmination of my university stage.

Also, I would like to thank my admirable friends Jaume and Dario for their unwavering source of motivation. I am truly grateful for the positive impact they have had on my life, encouraging me to be the best version of myself.

Finally, I would like to express my gratitude and appreciation to my thesis supervisor, PhD Nicholas Riedel-Lyngskær, for all his support and help during the project. His advice has guided me through this thesis, and without his assistance and dedicated involvement, this thesis would have never been accomplished.

Contents

List of Figures

List of Tables

1 Introduction

1.1 Background and motivation

Solar energy's enormous potential as one of the main renewable energy sources is clearly seen in the rapid growth of the solar market in recent years. The use of solar energy has grown significantly, with global installed capacity increasing from around 102 GW in 2012 to over 840 GW in 2021 [1]. This trend is favoured by a levelling of module prices coupled with a reduction in production costs and efficiency improvement, making it increasingly competitive with fossil fuels. Regarding the photovoltaic market, worldwide PV installations represent investments that can be measured as a percentage of the gross domestic product of some countries. At this magnitude, it is critical for all stakeholders to determine and predict long-term performance accurately.

Consequently, there has been an increasing demand for data monitoring and performance certainty during the entire plant's life. The degradation rate quantifies the gradual loss of performance, typically expressed in %/year, of a PV module (or system) over time. Accurate performance modelling of PV plants is a crucial factor that affects their economic viability and environmental impact. Moreover, the determination of the degradation rate and the underlying factors has vital financial and technical importance.

Financially, being able to predict the performance of PV plants over time gives a great advantage when developing a business model and studying the feasibility of an investment in a given project. A higher degradation rate means less yield, which leads to higher LCOE and ultimately a loss of cash flow in future years. As a result, the economic return on investment of PV systems depends greatly on its degradation rate, making it the third most important factor influencing the LCOE, after the discount rate and the initial cost [2]. Besides, the inaccurate determination of the degradation rate leads to inaccuracies in the business case which increase the financial risk.

From the technical point of view, understanding the main drivers of the degradation and how they affect the performance of PV modules is essential to improve their reliability and maintenance procedures, as they may gradually lead to failure. Determining the underlying physical processes is also crucial in the development of accelerated test protocols, in improving the service life and optimizing the system's performance. For instance, one of the challenges of accelerated testing is identifying and accounting for hidden degradation modes which could only become apparent under specific field conditions [3]. Therefore, reliable performance metrics, statistical methods and common filtering techniques exploiting continuous outdoor measurements are needed.

Overall, understanding the degradation rates of PV systems and accurately predicting the power delivery over its lifetime is of vital importance to the growth of the photovoltaic industry and to ensure the long-term success of solar energy.

1.2 The aim of the project

The aim of this thesis is to analyse long-term monitoring data and quantify the degradation rate of PV modules operating in a Nordic climate. The degradation analysis will be performed in Python, taking advantage of the packages and functions available for PV systems performance simulation (PVlib Python and RdTools [4, 5]). To do so, long-term production, irradiance and module temperature data from two PV plants will be filtered and analysed using the Year on

Year methodology [6]. Using real data is crucial for understanding the long-term behaviour and lifespan of PV systems, as it represents the actual operating conditions of the system.

Because degradation can differ between modules within the same model, it is more useful to refer to a population of modules. This study focuses on individual components (inverters or strings) which operate under the same weather conditions but have a different bill of materials and mounting orientation. Through this, it is possible to determine how the type of module or the system design influences the degradation.

An additional objective is to pinpoint the underlying degradation modes and investigate how they are impacted by the Nordic climate. This can be accomplished through visual inspection and flash testing selected modules in the laboratory, and analysing how each of the I-V curve's key parameters degrades over time. Furthermore, by determining the total insolation received (as a proxy for UV exposure) and studying the average cell temperature of the systems over time, it is possible to gain deeper insights into the degradation process.

Finally, the number of publications on long-term performance has been growing rapidly in recent years, reflecting the importance of the subject. However, to the author's knowledge, there are little to no reports on PV module degradation for tracking and bifacial systems. This thesis is one of the first contributions to address this issue and provide insights into the degradation in bifacial modules.

All in all, this research will lead to a better understanding of how PV modules in northern climates degrade during their lifetime and will increase yield prediction models' accuracy for the long-term evaluation of PV plants.

2 Degradation rates in PV plants. Theoretical background

The degradation rate of a photovoltaic plant refers to the rate (%/year) at which the performance of the plant declines steadily over time, being a negative value in case of degradation. This can be caused by a variety of factors, such as the bill of materials (and the properties of these materials), the quality of the PV modules and control system of the production line, the local climate conditions, and the level of maintenance the plant receives [7].

When deployed outdoors, PV modules are affected by continuous cycles of irradiation, temperature, humidity and mechanical stress, which are the factors behind their performance degradation [8]. These factors can cause one or more types of degradation that are detailed in the section below. This chapter also includes a literature review of the existing research on the degradation rates of PV systems and an evaluation of their findings.

2.1 Degradation modes

Degradation modes can significantly affect the performance and lifespan of PV modules, so it is important to understand and address these factors to ensure the long-term reliability and efficiency of a PV plant. They can be divided into material degradation (e.g., corrosion, delamination, cracks, etc.) and factors that depend on the operating conditions and act directly on its electric performance such as soiling, shading, module and cell mismatch, etc. The latter are performance-reducing events, which may be reversible or even preventable through good O&M practices, but may not necessarily relate to the temporal performance loss of the system [9]. In fact, according to the National Renewable Energy Laboratory (NREL), the most common degradation modes in modules for the last 10 years were hot spots (33%) followed by internal circuit discoloration (20%), glass breakage (12%), encapsulant discoloration (10%), cell breakage (9%), and potential-induced degradation (PID, 8%) [10, 11]. It is important to note that degradation modes may not occur independently of each other, making it difficult to isolate the root cause.

2.1.1 Front Surface Soiling

Surface soiling refers to the accumulation of dirt on the module's top surface. It is extremely location dependent and can be detected by visual inspection of the module [12]. Despite being a situation which can be reversed with proper maintenance or self-cleaning by wind and rain, the accumulated dirt may partially shade a cell in the module causing it to produce less current than the other string cells, which can lead to irreversible hot-spot damage and even module failure [13].

2.1.2 Optical degradation

Optical degradation may result from discoloration of the encapsulating material, usually Ethylene Vinyl Acetate (EVA). It is important to note that not all EVA products are the same. Different manufacturers may add various additives, such as ultraviolet (UV) stabilizers, anti-oxidants, and flame retardants, to enhance the performance and durability of the encapsulant. Besides, due to UV exposure, elevated temperatures, or humidity, yellowing of the encapsulating material can occur after extended exposure periods. It can also occur due to the diffusion of dirt from the front surface soiling and moisture ingress from the edge seals. However, in [14] it is pointed out that the chief cause of EVA deprivation is the UV radiation produced by water at temperatures higher than 50ºC.

As the discoloration progresses, the EVA changes color from light yellow to dark brown due to the formation of acetic acid from the UV stabilizers [15]. The brown EVA absorbs a significant fraction of sunlight, thereby reducing the photon availability required for the current generation. This browning of the encapsulant can cause the short-circuit current (I_{sc}) of the PV module to deteriorate up to a 13% lower of the nominal values for complete discoloration [16], so the maximum power of the PV module is correspondingly reduced.

2.1.3 Cell's internal circuit degradation

Solar cell's internal circuit degradation is mainly linked to three factors which result in a gradual degradation in module performance. These factors are an increase in the cell's series resistance, R_s; a decrease in the cell's shunt resistance, R_{sh}; and an anti-reflection coating (ARCs) deterioration [12]. Figure 2.1 shows the one-diode equivalent circuit model of a solar cell, illustrating the series and shunt resistances. These modes can gradually degrade module performance over extended operational periods and are discussed below.

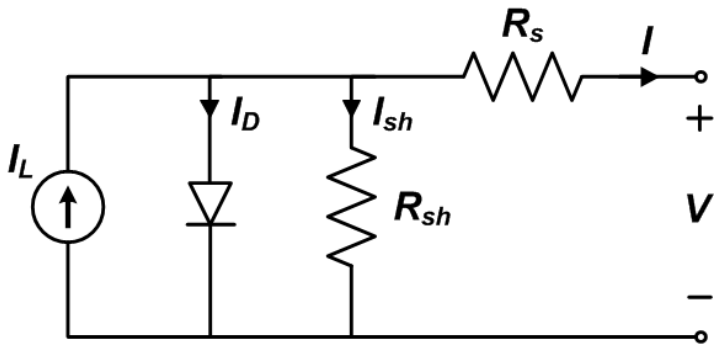

Figure 2.1: Equivalent circuit model of a solar cell

Series Resistance

In the one-diode model of a solar cell, R_s represents the resistance of the photo-generated current (I_L) as it flows through the cell in series. It arises from metallization, bus bar contact to the cell, resistances in cell solder bonds, and resistances in junction-box terminations [17]. The series resistance reduces the voltage produced by the cell, which ultimately reduces the performance of the PV cell, and hence the module. Although cell and module designers minimize series resistance losses as much as possible with advanced manufacturing techniques, daily thermal cycling of modules deployed outdoors inevitably results in a gradual increase in series resistance.

Shunt Resistance

The shunt resistance represents any parallel high-conductivity paths (shunts) through the solar cell or on the cell edges. These are due to Si manufacturing defects and impurities in and near the junction, and provide an alternate current path (I_{sh}) that leads the current away from the intended load. The number of shunts may grow after prolonged exposure to light [18], which increases the effective shunt current in the cell. This has a detrimental effect on the module performance, especially at low-intensity levels [12].

Figure 2.2 and 2.3 show the undesired effect of increasing R_s and decreasing R_{sh} on the I-V curve.

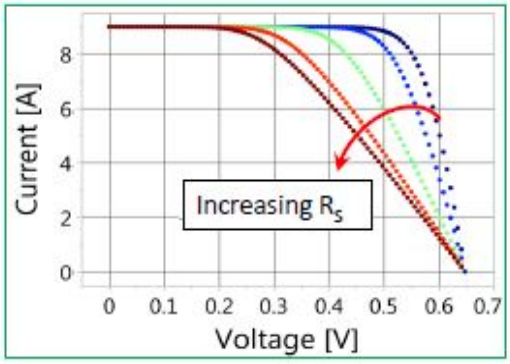

Figure 2.2: Effect of increasing Series resistance on the I-V curve [19]

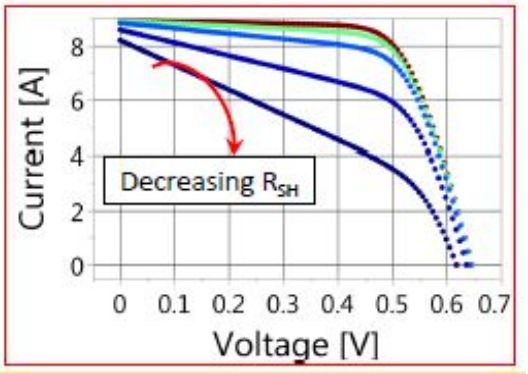

Figure 2.3: Effect of decreasing Shunt resistance on the I-V curve [19]

Anti-Reflective Coating

Anti-reflective coatings are thin films applied to the surface of PV modules to reduce the amount of light that is reflected by the module. For example, Silicon nitride (SiNx) is an anti-reflective coating known for its high transparency and low absorption in the visible and near-infrared spectral ranges. A low reflectivity allows more light to pass through the surface of the module and reach the solar cells, improving both short-circuit current and open-circuit voltage, which in turn enhances the conversion efficiency of a PV cell [20].

AR coatings are usually transparent oxides whose degradation after time may be attributed to the inter-diffusion of species from the cell's emitter region to the AR coating and vice versa [12]. The effect of the degradation of the AR coating of a cell in a series connected string is that the cell will now absorb fewer incoming photons and hence produce less current than the other string cells. The result is a mismatched cell, which is discussed in the next section.

2.1.4 Mismatched cells

Mismatched cells are caused by the aforementioned degradation modes (front surface soiling, encapsulant degradation, AR coating deterioration) and also manufacturing defects, cell cracking and partial shading of the PV cell [12]. When a cell in a module is producing less current than the other module cells, and they are all connected in series, the latter cells act to reverse bias the former, mismatched cell. This causes the defective cell to operate in the negative voltage region where it dissipates power and degrades module performance [21].

Cracked cells

Cracked cells can be caused by several factors, including thermal and mechanical stress, manufacturing defects or impact damage during the mounting of the PV module. The damaged cell can still operate but it will have the effect of a reduced current produced by the cell and increase the risk of moisture penetration. The loss in power is related to the loss in current flow and depends on the direction of the cracks as well as the integrity of the metallization [2]. In a PV module that is already in operation, it is generally difficult to identify a crack with the naked eye, so optical methods such as EL testing can be used [22].

Broken glass significantly degrades photovoltaic modules. Most of the time, this occurs during the mounting of the PV module, but also thermal stress and hail damage can cause the cracking of glass.

Delamination

Mismatched conditions in solar cells cause the lowest-performing cell in a sub-string to heat up. When the mismatched cell is under high-humidity and high-temperature conditions, degradation of the adhesion between the encapsulation polymer and the solar cell may occur [21]. This is

known as delamination and leads to a decrease in the transmittance of light and current. As delamination gets more severe, the probability of moisture intrusion increases, causing extensive physical and chemical damage such as corrosion. Moreover, delamination disturbs efficient heat removal from the cells and changes in temperature cause thermochemical stresses on the solder joints between ribbons. This can lead among others to loose contacts, increased series resistance and increased heating of surrounding cells decreasing both the fill factor (FF) and the open circuit voltage (V_{oc}) [8].

Another consequence of high temperatures is the increase in the possibility of reverse cell operation, which can lead to the formation of hot spots in the cell.

Hot spots
Hot spots are areas on the surface of the cell where the temperature is significantly higher than the surrounding areas. They are formed in high heat-dissipation positions due to a reverse voltage caused by fractional shadows, cell mismatches, or interrupted connections between cells [11]. Nowadays, modules integrate bypass diodes in their interconnection circuits to prevent a mismatched cell to cause irreversible hot spot damage. In the event of bypass diode failure, the high reverse bias can exceed the cell's breakdown voltage and the cell may be irreversibly damaged by thermal breakdown.

Indeed, hot spots can cause the module to fail prematurely if the high temperatures cause the cells or other components to degrade. From the electrical point of view, hot spot formation not only lowers the efficiency of the module, but also influences the open circuit voltage, the short circuit current, the maximum power (P_{mp}), and the fill factor.

Overall, mismatched cells can usually be detected by visual inspection, I-V measurements, hot-spot endurance testing and/or individual cell temperature monitoring when the module is forward biased [12].

2.1.5 Light-induced degradation
Light-induced degradation (LID) is a phenomenon in which the efficiency of the module decreases in the first months of deployment due to exposure to light. The boron-oxygen complex is one of the primary causes of LID and refers to a defect in the PV cell that is caused by the presence of boron and oxygen impurities in the semiconductor material. When exposed to light, this complex can trap electrons and holes, leading to the recombination of the charge carriers. This, which affects especially amorphous/crystalline silicon cells, can lead to a permanent reduction in the power output of the module driven by a strong degradation of I_{sc} and V_{oc} and to an increase in the resistance of the cells, leading to higher temperatures and further degradation [23].

2.1.6 Temperature-Induced Degradation
PV modules are rated by their power as measured at standard test conditions (STC: 1000 W/m^2 irradiance, 25ºC cell temperature and Air Mass 1.5 global spectrum). However, when a module is operating outdoors, a large fraction of the incident energy is transformed into heat. It is therefore obvious that a module, operating outdoors, will most likely have a temperature above 25ºC.

At these elevated temperatures, band gap energy decreases so consequently I_{sc} and the saturation current increase exponentially with the increase in temperature. This acts to reduce the cell's V_{oc} more rapidly than the increase in I_{sc} resulting in an overall reduction in the cell's fill factor, and hence, efficiency when the temperature increases. High temperatures followed by low temperatures can also cause the cells and busbars to expand and contract, which can lead to mechanical stress and permanent degradation of the cell's electrical properties.

It is therefore imperative that elevated temperatures influence the performance of all modules. For this reason, a temperature coefficient is given in the manufacturer's specifications for each model and used to explain the behaviour of the modules when operating outdoors. It is usually a power loss of around -0.3% to -0.5% per degree Celsius above 25ºC and a gain when the temperature is below 25ºC. Figure 2.4 shows the effect that cell temperature has on the I-V curve [19].

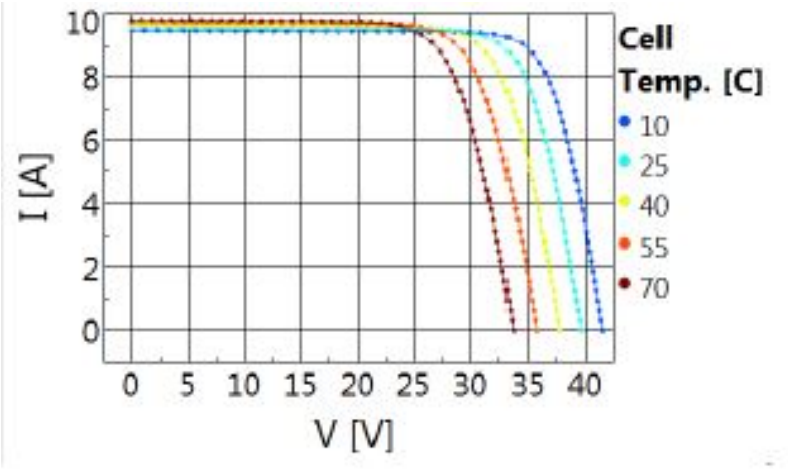

Figure 2.4: Effect of cell temperature on the I-V curve [19]

2.1.7 Light and elevate temperature induced degradation

Another degradation effect caused by the exposure of the cell to light, is the Light and elevate Temperature Degradation (LeTID). This degradation causes loss in module performance when the cells are exposed to both light and elevated temperature (>50 ºC) for a long period.

Similarly to LID, LeTID is a prevalent failure mode in PERC cells (i.e., the cells studied) [24]. However, studies have shown that LeTID happens at a much slower degradation rate than what has been experienced with LID [25] and it can take years of exposure to sunlight and elevate temperature until the cell start showing sings of LeTID. Regarding the bifacial panels, more research on the effects of LeTID is needed. Based on [26] it can be expected that the LeTID effects on bifacial modules will be less significant.

2.1.8 Potential-Induced Degradation

The typical system voltage is around 1000V DC. In the most negative section of a string, there is a high potential difference between the PV module and its structure (acting as ground). When the protection between the structure and the high-voltage layer deteriorates, a leakage current from the cells to the ground can be created, allowing the electrons in the PV module material escape through the soil [27]. This can cause cause localised stacking faults (i.e. short circuits). Also, PID causes a reduction in the shunt resistance and, once the effect takes place, the leakage current is most likely to keep increasing leading to further degradation [28]. According to [29, 30], the leakage current increases with moisture, so PID is more likely to occur in moist weather than in warm and dry climates.

2.1.9 Corrosion

The deterioration of any PV-module component can facilitate corrosion, permitting the penetration of water and oxygen into the solar cell. Then, corrosion can be related to other degradation modes and initiated and accelerated by several factors simultaneously, having a reciprocal cause-and-effect relationship [31]. According to [32], the back sheet and encapsulant are the most influential factors related to corrosion.

To sum up, solar modules do not usually fail in a catastrophic way but experience steady power degradation over time. In this sense, all the described degradation modes affect to a greater or lesser extent a gradual power loss in the PV system. Figure 2.5 shows typical power loss from the different mechanisms over time [33]. The overall degradation rate can vary widely, so the next section will evaluate the most recent PV module degradation studies and their results.

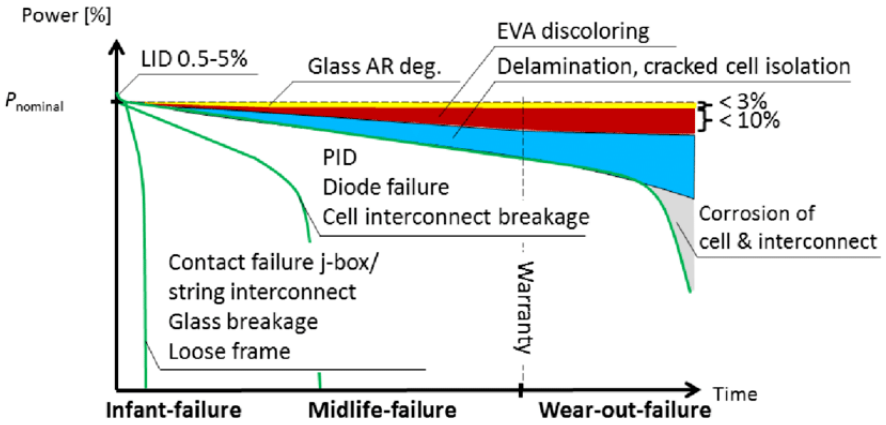

Figure 2.5: Power loss due to typical failure scenarios over time [33]

2.2 Degradation studies. Literature review

The degradation at the module level has been extensively studied since the construction of the first PV plants. Over the years, numerous studies ([34, 35, 36] among others) have focused on understanding the causes of degradation and finding ways to mitigate it. The main conclusion of these studies is that PV degradation is typically caused by a combination of factors, which depend on the type of cell or modules' technology and the specific conditions to which the cells or modules are exposed (location, climate, maintenance, measurement uncertainty, etc.). In fact, accurate modelling of the degradation rate requires an exhaustive understanding of PV module properties and a physical modeling framework, which is not the focus of this work.

To assess the status and the health of the industry in general, a representative sample is essential. In 2012, Jordan and Kurtz summarized 2128 degradation rates reported in published literature from field testing [37]. It was found that modules appear to lose a median of -0.5% per year (average of -0.8% per year). Figure 2.6 shows the distribution of these degradation rates, where 78% lie below -1% per year. A similar skewed graph is to be expected when looking at a specific system, as most modules will degrade slowly while there will be few other modules that decay faster [38]. Then, in 2016, more than 11,000 degradation rates in almost 200 studies from 40 different countries were aggregated and re-examined by the same authors [39]. It was found a median degradation for x-Si technologies in the 0.5–0.6%/year range with the mean in the 0.8–0.9%/year range.

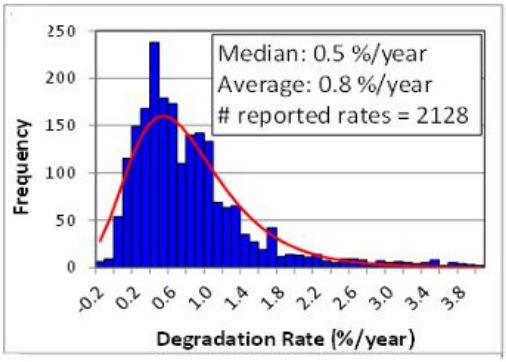

Figure 2.6: Histogram of reported degradation rates [37]. Note: Positive values mean degradation.

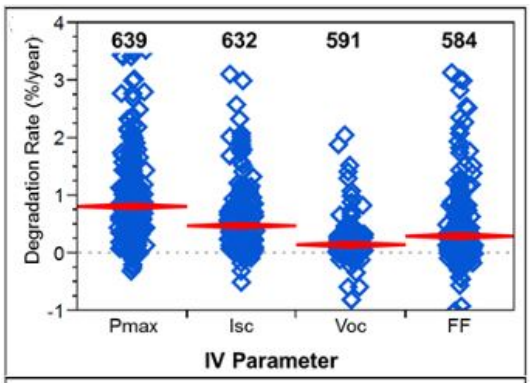

Figure 2.7: P_{mp}, I_{sc}, FF and V_{oc} degradation rates for mono-Si cells [37]. Note: Positive values mean degradation.

Additionally, in [39] more than 1100 reported rates included some or all I-V parameters. Figure 2.7 shows the annualized degradation rate for P_{mp}, I_{sc}, FF and V_{oc} in mono-Si cells. It is seen that the largest contributor to maximum power decline is short circuit current degradation, which can be attributed to delamination, discoloration and cracked individual cells as discussed in section 2.1. Significantly less degradation comes from FF, typically associated with corrosion and solder-bond breakage. Finally, relatively small changes are appreciated in open-circuit voltage, so these modules were not likely affected by PID.

Since this compendium, new degradation rates from field testing have been reported globally. Table 2.1 presents a synopsis of the latest reported degradation rates, including those in bifacial modules.

Table 2.1: Summary of recent studies on PV module field degradation

#	Location	Cell/Module Technology	Mounting configuration	Period (years)	Median Deg. rate (%/year)	Reference
1	Florida	Poly-Si monofacial	Fixed tilt	4-5.5	-1 $\pm$ 1	[40]
2	All over US	Mono-Si, Poly-Si CdTe, PERC monofacial	Fixed tilt, Tracking	2 minimum	-0.75	[41]
3	Unknown. Hot and moderate climate	Poly-Si monofacial	Fixed tilt	5	-1.4 (hot) -0.94 (moderate)	[42]
4	Nicosia	Mono-Si, Poly-Si CdTe, CIGS monofacial	Fixed tilt	8	-0.83	[43]
5	All over Europe	Not specified monofacial	Fixed tilt	2-4	-0.67	[36]
6	Dubai	Not specified bifacial	Fixed tilt	4+	-1.57 (front) -0.64 (back)	[44]
7	Unknown	Mono-Si Al-BSF, PERC monofacial Mono- Si PERC bifacial	Fixed tilt	2.5	-0.55 (Al-BSF) -0.62 (PERC mono.) -0.95 (PERC bif.)	[45]

A summary of the seven studies in table 2.1 is provided below:

1. The Florida Solar Energy Center evaluated the performance of two nominally-identical grid-connected PV systems (3960 Wp) in Florida. They were operational since 2003 and evident power reduction differences were measured in the monitoring period 2003-2008. Both systems were analysed using PR as a metric, with monthly values and 15-minute

increments. The study was conducted on the DC and AC sides. The degradation rates were all in the range -1 $\pm$ 1% /year. Then, the I-V curves were measured showing a higher degradation (between -1.8 and -2.2 %/year) but the source of this higher degradation was not identified.

2. In the PV Fleet Performance Data Initiative, data from more than 1700 sites in the US were collected to examine the degradation at a fleet scale. An overall median of system degradation of -0.75 %/year was found. This study got other relevant conclusions: Inverter degradation did not contribute to system degradation, tracked systems showed no statistical difference versus fixed tilt systems and higher degradation was found in hotter temperature zones.

3. In 2021, Scott W. Adler used the Year on Year methodology to perform a comparison between 2 utility-scale plants with the same technology but located in different climates. The median of the nominal system degradation rate measured on the DC side of the inverters in the hotter and more humid climate was found to be −1.4 %/year whereas, in the temperate climate, the median rate was −0.94%/year. These results suggest that climate zones must be included when evaluating the long-term performance of PV plants. It also remarks that the YOY method as implemented in RdTools is a robust approach for calculating degradation rates where multiple years of reliable data are available.

4. This work carried out by Marios Theristis in 2020 presents a new methodology to detect and calculate non-linear degradation rates based on PV performance time series from nine different systems over an eight-year period. The median degradation rate of these systems using the YoY methodology was found to be -0.83 %/year. Thin-film technologies demonstrated non-linear behaviour, so it highlights the importance of applying ”non-conventional” models to estimate the long-term degradation due to its impact on the LCOE.

5. The COST Action PEARL PV analysed data of 8400 small residential systems across Europe. The degradation is calculated using 3 different statistical approaches (statistical clear-sky fitting, Year on Year and seasonal and trend decomposition). With the YoY methodology, the median degradation rate was found to be -0.67 %/year. This study also concludes that a minimum of 3 years of data is required to get sensible results and that the longer the time series, the more trustworthy the results tend to be.

6. This study investigates the degradation of bifacial PV modules installed under desert climatic conditions for more than four years. The degradation rate and mechanisms are analysed through indoor characterization, including IV measurement under STC conditions, electroluminescence imaging and visual inspection. It is concluded that the front side of the bifacial modules shows a higher degradation rate (1.3-1.88%/year) compared to the back side (0.39-0.78%/year). The degradation was mainly driven by the reduction in I_{sc} and Fill Factor, being EVA discoloration the main contributor due to the high temperatures of the desert climate.

7. This work is focused on the effect that temperature and mounting structure have on the degradation of different types of cells. Among other studies, a mono-Si Al-BSF control module, a mono-Si PERC module, and a mono-Si PERC bifacial module from the same manufacturer were monitored for 2.5 years. It was shown that the bifacial PERC module showed slightly higher, yet not statistically significant degradation associated with I_{sc}, FF and V_{oc} loss. Also, it is concluded that degradation rates are technology and quality dependent, yet the details of the mounting also play a significant role.

In light of the above, it is seen that degradation rates have been investigated by many authors in

recent years. However, in spite of much research, the precise rate at which PV plants degrade is not trivial to predict and studies only provide a temporary glimpse into the state of systems that may be subject to change. The final observation drawn from this literature review is that not only technical factors such as the cell technology, climate, and mounting configuration influence PV system degradation rates, but also the method and details of the analysis itself introduce significant variation in the result.

2.3 Uncertainties

Every analysis described in the previous section has some degree of uncertainty linked to it which can be usually understood and quantified. The main goal of this section is to explore the uncertainties related to the whole degradation rate calculation process and their main drivers. The uncertainty of the measuring sensors and calculation methodology are described below, followed by additional uncertainties that can exist.

2.3.1 Sensor uncertainties

The limited accuracy of measurement equipment represents one of the systematic uncertainties linked to solar energy. Besides, physical sensors tend to lose accuracy over time in the field and are prone to sensor drifting, which can occur gradually and make degradation appear significantly higher or lower than it actually is. Moreover, depending on the location and surroundings of a PV power plant, all the objects are exposed to dirt accumulation or soiling. This can limit the transmittance of light into the module and irradiance sensor (e.g. pyranometer) thus the power output and reported irradiance values.

According to [46, 47], sensor and module soiling behaviour are similar when reference cells are used as sensors. However, soiling rates are likely lower on pyranometers compared to flat plate reference cells due to their dome shape [47]. In the systems under consideration, the pyranometers have been regularly calibrated and cleaned, so incorrect results due to sensor soiling losses are minimized and therefore soiling effects are not seen as decisive for the result of the degradation analysis. Additionally, the uncertainty of the three main parameters measured in the field are the following:

Electrical parameters

The uncertainties of measured current and voltage are dependent on their actual magnitude since the accuracy of data acquisition units depends on the input signal [46]. In fact, the measurement uncertainties for the energy parameters are relatively low and lay below 1% for DC according to [46, 48]. Another uncertainty is the nameplate power of the installed modules, which can differ up to 5 W (approx. 1.7%) from the actual DC capacity. However, this is not considered a problem for determining long-term degradation because all performance ratios will be shifted up or down without changing the rate of change. Finally, the uncertainty in cabling and inverter losses is considered less than 1% [38].

Temperature

The temperature is used to normalize the measured power as if the module was operating at 25ºC (STC) using a temperature coefficient which can be found in the module's datasheet. Studies report and uncertainty for module temperature between $\pm$1% and $\pm$1.7% [35, 46, 48]. Incorrect measurements occur when the sensors became partially or completely detached from the modules, as was appreciated in one of System B's sensors. In fact, a detached sensor will measure lower temperatures due to poor thermal contact, which makes the expected power increase, thus appearing as degradation.

Irradiance

The most critical uncertainties are those related to the irradiance measurement due to the weight it has in the performance calculations. The measurement uncertainty of a pyranometer in use depends on many parameters, some relating to the instrument performance and some specific

to the measurement location. According to [49], pyranometers are divided into three classes (A, B or C) depending on their properties (calibration uncertainty, response time, resolution, thermal response, offset, etc.). Indeed, the pyranometers used in both systems studied are class A (best in quality), with a daily total uncertainty of 2% [50]. The uncertainty of irradiance data increases significantly if reference cells or satellite data is used for the analysis, which will be discussed in section 4.1.2. However, for an accurate result of a degradation analysis, it is especially important that the irradiance sensor is stable, as the resulting rate of change would not be affected by a constant offset because of a wrong calibration [46].

2.3.2 Methodology uncertainties

Besides periodic I-V curves in the lab, the most accurate way to obtain the degradation rate of a PV system/component is to use on-site monitoring data after passing the aforementioned quality checks. Also, it is imperative that the calculation is more accurate, the more the applied performance metrics, statistical methods and filtering techniques succeed in minimizing seasonal oscillation and eliminating outliers. There is, however, a lack of agreed rules on data filtering, outlier removal and data averaging strategies. These different methods lead to different results.

In spite of the traditional approach of performing a linear regression against time, the Year on Year methodology is less susceptible to outliers or marked seasonality. This makes it the preferred methodology in terms of accuracy although several studies recommend a minimum period of three years of continuous outdoor data to perform a reliable degradation rate evaluation [7]. The results shown in the YoY calculation include a Monte Carlo-derived confidence interval which is set to 68.2% as default.

2.3.3 Other uncertainties

Next to these hardware-related variables, there are additional uncertainties in the overall calculation of degradation rates. These refer to the models applied when some of the variables are not monitored on-site (conversion from global horizontal to POA irradiance, cell temperature, IAM losses, etc.) and need to be modelled. All the models applied during the analysis, although widely accepted in the analysts' community, are just statistical, analytical or semi-empirical procedures that could differ to a greater or lesser extent from the real situation on the PV plant.

Regarding the flash test method (section 5.6), although the flasher has a 3% expanded uncertainty for P_{mp} measurements of c-Si panels, all the modules are flashed with the same flasher and, when the test is repeated multiple times, the results are consistently within a narrow range, indicating that the test is repeatable. However, the degradation rate obtained from the results of the flash test is subject to high uncertainty regarding two main aspects:

- **Reference:** Ideally, modules should have been flashed prior to their installation but this was not the case. When it is possible, a reference module (i.e., a PV module of the same model as the tested ones) is used to compare with the fielded one. When a reference module is not available, the comparison is made directly with the datasheet.
- **Power tolerance:** Modules from the same batch have a positive power tolerance of +5W, which is around 1.7% of the nominal power. When comparing with a reference module or the datasheet, this can bias the results.

Overall, the fundamental difficulty is that the true degradation rate is unknown, making the accuracy assessment difficult. Even with indoor IV measurements the true degradation rate value and thus the uncertainty of the whole process can only be estimated.

3 Description of PV systems analysed

3.1 System A

System A is a 13.104 MWp solar power plant located in the North-East of Aylesbury, England. Figures 3.1 and 3.2 show an aerial view and the location of the PV plant.

Figure 3.1: System A aerial view

Figure 3.2: System A location

Covering an area of approximately 0.25 km^2, the PV plant has been operational since March 2015. Figure 3.3 shows the eleven sub-fields (A to K) in which the plant is divided, each of which corresponds to a central inverter. The strings of each area are grouped into string combiner boxes, which are the inverter's inputs. The inverters are then connected to a transformer which connects the plant to a 33 kV overhead transmission line that runs close to the site.

Figure 3.3: System A layout. Each zone corresponds to a central inverter

3.1.1 PV modules

The 48,936 PV modules used in System A are the REC260PE, from the manufacturer REC Solar. They have a nominal power rating of 260 Wp and are made of polycrystalline silicon. All the modules are rack-mounted facing south with a fixed angle of 20º. Table 3.1 below summarises the PV module's key technical specifications. The annual linear degradation rate that is covered under warranty according to the data sheet and the parameters that will be used for the module temperature calculation in section 4.1.3 are also detailed in table 3.1. The Sandia thermal model's parameters a, b and ΔT depend on the module construction materials (Glass/-cell/polymer sheet) and the mounting configuration (open rack) [51].

Table 3.1: System A modules technical specifications

Specification	Data	Unit
Construction	Glass-Polymer	-
Cell type	Polycrystalline silicon	-
Number of cells	60	-
P_{mp} at STC	260	W
I_{sc} at STC	9.01	A
I_{mp} at STC	8.5	A
V_{oc} at STC	37.8	V
V_{mp} at STC	30.7	V
P_{mp} temperature coefficient	-0.4	%/ºC
Linear degradation rate (warranty)	-0.7	%/year
Parameter "a" in Sandia model	-3.56	-
Parameter "b" in Sandia model	-0.075	-
Parameter "ΔT" in Sandia model	3	ºC

3.1.2 Inverters

Additionally, the 11 inverters are the Sunny Central 900CP XT, manufactured by SMA Solar Technologies. The main technical specifications of this outdoor inverter are presented in table 3.2

Table 3.2: System A inverter technical specifications

Specification	Data	Unit
Max. DC input power	1010	kW
Max. input voltage	1000	V
Max. input current	1400	A
Number of MPPT inputs	1	-
Rated output power	900	kW
Rated output voltage	405	V AC
Max. output current	1411	A
Max. efficiency	98.6	%
European efficiency	98.4	%

It is important to note that, according to the number of strings combined, each inverter has different DC capacities. These are detailed in table 3.3.

Table 3.3: Inverter DC capacities System A

Inverter ID	Combiner boxes	Strings	DC cap (kW)
1.1	14	181	1,129.44
1.2	14	185	1,154.40
2.1	16	200	1,248.00
3.1	16	190	1,185.60
3.2	16	194	1,210.56
4.1	14	186	1,160.64
4.2	14	182	1,135.68
5.1	14	184	1,148.16
5.2	14	185	1,154.40
6.1	18	207	1,291.68
6.2	16	206	1,285.44
PLANT	**1434**	**2100**	**13,104.00**

3.1.3 Sensors

For the data monitoring, System A is equipped with 4 pyranometers SMP11 from Kipp & Zonen (Class A according to ISO 9060:2018 [49]). From these, 3 are tilted measuring plane of array irradiance and the other one is horizontal, measuring the global horizontal irradiance (GHI). The pyranometers have been calibrated every 2 years, so it is expected a high precision in their measurements during the whole period analysed. Moreover, back-of-module temperature is monitored with 2 PT1000 temperature sensors. Also, a weather station in the plant is equipped with an ambient temperature sensor and a wind speed and direction sensor. Finally, different electrical meters measure DC current and voltage as well as AC energy output. The monitoring system is provided by Sunergy and an overview is presented in fig. 3.4.

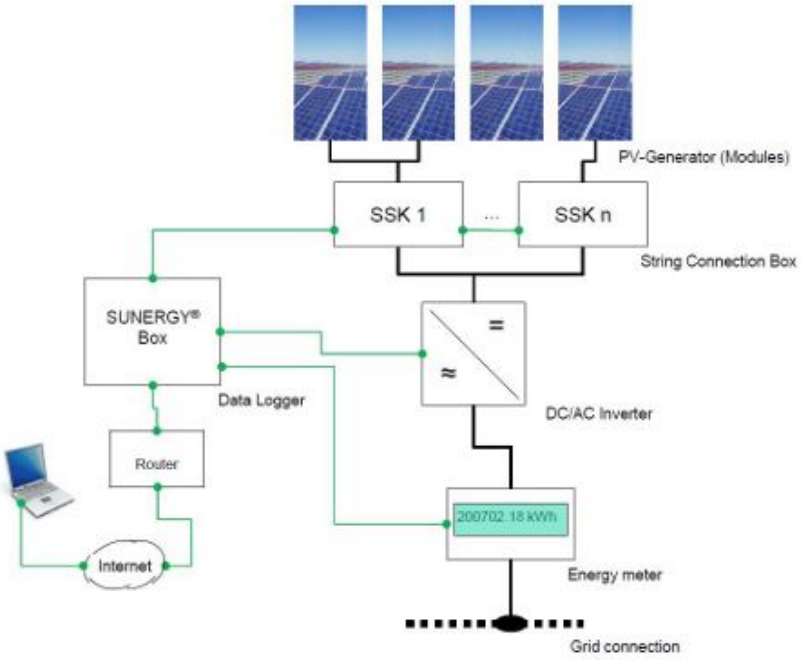

Figure 3.4: System A monitoring system overview

3.1.4 Data availability

Since the plant is operational, DC and AC power (kW) have been recorded for every string in a 15-minute resolution. However, because of the high number of strings, only data at an inverter level is considered for the analysis of this system.

Despite the long monitoring period System A has, the main limitation is that, due to a change in the monitoring system, from 2015 to 2018 the irradiation measurements are only available on a daily basis. This information is obtained from the O&M's monthly reports of the plant, so there is no access to the intraday weather data in this period. From May 2018 onward, irradiance (W/m^2) measured from the pyranometers is available with 15-minute resolution, which allows an intraday and more precise data filtering. In the same way, module temperature (ºC) from the sensors is only available from 2018 in 15-minutes resolution, as it was not included in the O&M's monthly reports. Chapter 4 makes a deeper insight into these data limitations and the approach to cover them to obtain reliable results.

3.2 System B

System B is a 236.3 kWp PV park built in the summer of 2018. It is located in the north of Roskilde, Denmark, and is operated by DTU. Figures 3.5 and 3.6 show an aerial view and the location of the PV plant. Rather than a purely grid-connected PV plant, its main purpose is, among other experiments, to study bifacial energy gains under various installation conditions in the Danish climate.

Figure 3.5: System B aerial view

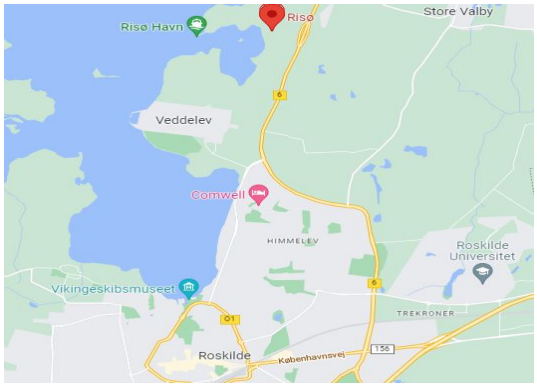

Figure 3.6: System B location

Figure 3.7 illustrates the plant layout of System B. As it is shown, there are 8 horizontal single-axis trackers facing east-west and 8 south-facing trackers with a fixed-tilt angle which is adjustable, but set to 25º during the analysis period. The PV tracker facility features monofacial and bifacial strings of similar front-side power mounted side-by-side. To the east of the plant, there is an extra string on a single-axis tracker as well as a dual-axis tracker system. In total, there are 10 operational inverters connected to the grid. Figure 3.7 also shows where the different monitoring sensors are located. These will be further detailed in section 3.2.4.

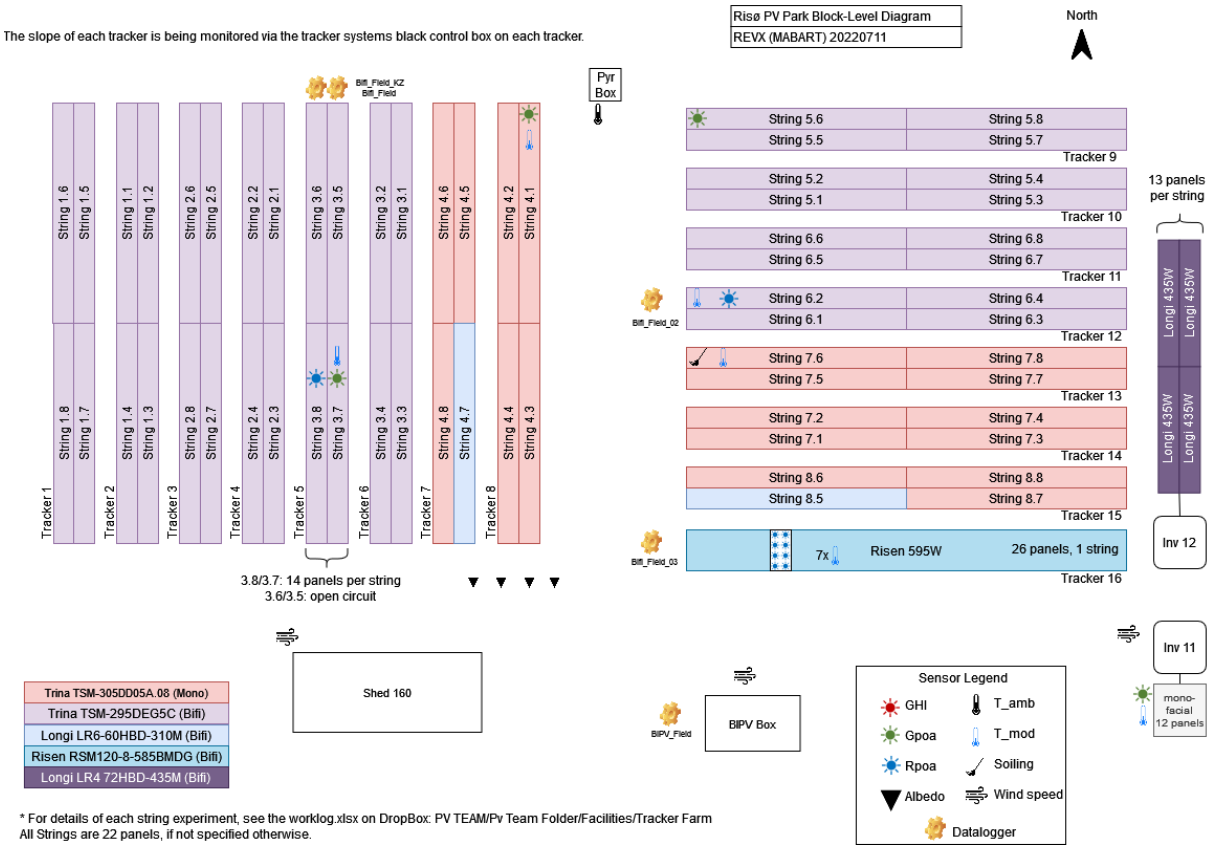

Figure 3.7: Plant layout System B (Figure by Martin Bartholomaus)

3.2.1 Trackers

Regarding the tracking system, all contain four strings (in two rows) of 22 panels in portrait mode. The only exceptions are the eastern tracker (Inverter 12), which consists of two strings of 13 modules each, and the 2-axis tracker, consisting of 12 modules.

On the one-axis trackers, the rotation is varied from −60º in the morning (facing east) to +60º in the evening (facing west) by an algorithm that uses astronomical equations to track the sun in azimuth. The angular position is monitored by inclinometer sensors mounted on the back of the trackers. The row spacing varies between 12 and 15 m.

On the other hand, the fixed-tilt system has an adjustable tilt from 0 to 60 degrees but is usually set to 25º oriented towards south.

Table 3.4: System B tracker specifications

Specification	Single axis tracker	Fixed tilt	Units
Manufacturer	Soltec	Soltec	-
Tracking angle	±60	25	º
Azimuth	90 or 270	180	º
Back tracking	Yes	NA	-
Tracker pitch	12	7.6	m
Hub height	1.95	2.3	m

3.2.2 PV modules

The main two types of panels installed are monofacial Trina 305 Wp and bifacial Trina 295 Wp panels, which are both made with passivated emitter and rear contact (PERC) cell. Over time, some strings have been replaced with other panels, but these will not be considered in the long-term degradation analysis because they all had been operating for less than three years at the start of this thesis project. Table 3.5 summarises the technical specifications of these two module types in System B. The parameters a, b and ΔT used in the Sandia thermal model explained in section 4.1.3 are also included. These parameters are chosen according to [51] and differ from each other because they depend on the module construction type (glass/cell/polymer for monofacial or glass/cell/glass for bifacial) and mount combination (open-rack in both cases).

Table 3.5: System B module specifications

Specification	Monofacial	Bifacial	Units
Model name	TSM-305DD05A.08	TSM-295DEG5C	-
Construction	Glass-Polymer	Glass-Glass	-
Cell type	mono PERC	mono PERC	-
Number of cells	60	60	-
P_{mp} at STC	305	295	W
I_{sc} at STC	9.85	9.58	A
I_{mp} at STC	9.28	8.97	A
V_{oc} at STC	40	39.9	V
V_{mp} at STC	32.9	32.9	V
Temp. coefficient of power	-0.39	-0.39	%/ºC
Linear degradation rate (warranty)	-0.71	-0.5	%/year
Parameter ”a” in Sandia model	-3.56	-3.47	-
Parameter ”b” in Sandia model	-0.075	-0.0594	-
Parameter ”ΔT” in Sandia model	3	1	ºC

3.2.3 Inverters

System B is equipped with Delta RPI M50A-12s inverters, each of which MPPT tracks all 4 parallel strings mounted every two trackers. In fact, a DC box is installed between each inverter and the panels, which includes Gantner string bloxx 208 for monitoring string current and array voltage. This is where the electrical data for this analysis is obtained from. Also, behind the inverter, a Gantner AC measurement box is installed.

Table 3.6: System B inverter technical specifications

Specification	Data	Units
Max. DC input power	58	kW
Max. input voltage	1100	V
Max. input current	100	A
Number of MPPT inputs	2	-
Rated output power	50	kW
Rated output voltage	400	V AC
Max. output current	100	A
Max. efficiency	98.6	%
European efficiency	98.4	%

The following table gives an overview of all the inverters in System B and the string connected to each of them, their capacity and configuration.

Table 3.7: System B inverter configuration

Inverter	Tracker	Strings connected	String DC-cap (W)	Module type	Tracker configuration
1	1,2	1.1-1.8	6490	Bifacial	1-axis tracker
2	3,4	2.1-2.8	6490	Bifacial	1-axis tracker
3	5,6	3.1-3.8	6490	Bifacial	1-axis tracker
4	7,8	4.1-4.8	6710	Monofacial	1-axis tracker
5	9,10	5.1-5.8	6490	Bifacial	Fixed-tilt
6	11,12	6.1-6.8	6490	Bifacial	Fixed-tilt
7	13,14	7.1-7.8	6710	Monofacial	Fixed-tilt
8	15,16	8.1-8.8	6710	Monofacial	Fixed-tilt
11	-	11.1	3660	Monofacial	2-axis tracker
12	-	12.1	5665	Bifacial	1-axis tracker

3.2.4 Sensors

In System B, an independent weather station provides data of the three solar components (GHI, DHI and DNI) with a frequency of ten seconds, which is then averaged to a one-minute resolution to reduce the variability. The measurement of solar irradiance components is crucial, so these sensors are systematically cleaned and periodically calibrated. Figures 3.8 and 3.9 were taken from the weather station 400 m south of System B.

Figure 3.8: DHI pyranometer and DNI pyrheliometer in System B's weather station

Figure 3.9: Horizontal solar radiation sensors in System B's weather station

On site, the irradiance is measured with two high-precision pyranometers which are tilted in the plane of the array. As is shown in fig. 3.7, they are located in Tracker 8 for the tracking strings (fig. 3.10a) and in Tracker 9 for the fixed tilt modules. Regarding the module temperature measurements, there are three sensors located on the back side of different modules. The first one installed was the sensor in Tracker 8 (fig. 3.10b), which measures the temperature of a monofacial tracking module. At the beginning of 2021, sensors were installed in the fixed-tilt systems (Tracker 12 and 13), which are shown in figs. 3.10c and 3.10d. It is worth mentioning that during the site visit, the sensor in Tracker 13 which measures temperature for bifacial fixed

tilt systems appeared to be loose from the back side of the module. The measurements of this detached temperature sensor are detailed in section 4.2.4.

(a) POA pyranometer on Tracker 8

(b) Temperature sensor on Tracker 8

(c) Temperature sensor on Tracker 12

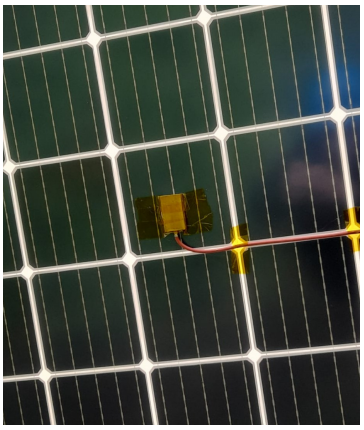

(d) Temperature sensor on Tracker 13

Figure 3.10: Sensors on-site System B

Moreover, the DC-side electrical parameters of each array are measured every 1 min by the combiner boxes, which assure a good level of accuracy in current and voltage. In this case, the voltage (V_{mp}) is recorded for each of the MPPTs (one voltage for 4 strings) while the current (I_{mp}) is available for every string, which provides a different power measurement in every string and therefore allows to perform an individual string analysis. The AC side is measured by the inverters and AC boxes, but will not be considered in this analysis. On the site, there are also ambient temperature, wind speed, soiling and albedo sensors, whose information will be used for modelling the missing parameters in chapter 4.

3.2.5 Data availability

Thanks to the sensors and monitoring devices in System B, weather data has been recorded since August 2018. However, string-level electrical data is available from February 2019, so this is when the analysis period starts. Due to its experimental purpose, System B has experienced lots of changes in hardware and software configurations which have induced numerous data shifts that need to be considered in the analysis. In the forthcoming chapter 4 all the data limitations and their modelling are detailed.

4 Data limitations and modelling

Data quantity and quality are both determinant factors when obtaining the long-term degradation rate of a component in a PV plant. In this sense, different measures have been taken in both systems to guarantee data reliability as much as possible. This chapter covers the encountered data limitations and the different approaches to solving them.

4.1 System A

Figure 4.1 shows an overview of the workflow process that has been followed. After the data collection and initial checks, the availability of intraday data for the three main parameters is evaluated. To make the maximum of the data available, two main approaches will be followed: 1) a *Daily analysis* with data since the plant is operational and 2) a *Detailed analysis* with 15-minute resolution data from March 2018 until September 2022. These approaches will be explained in chapter 5.

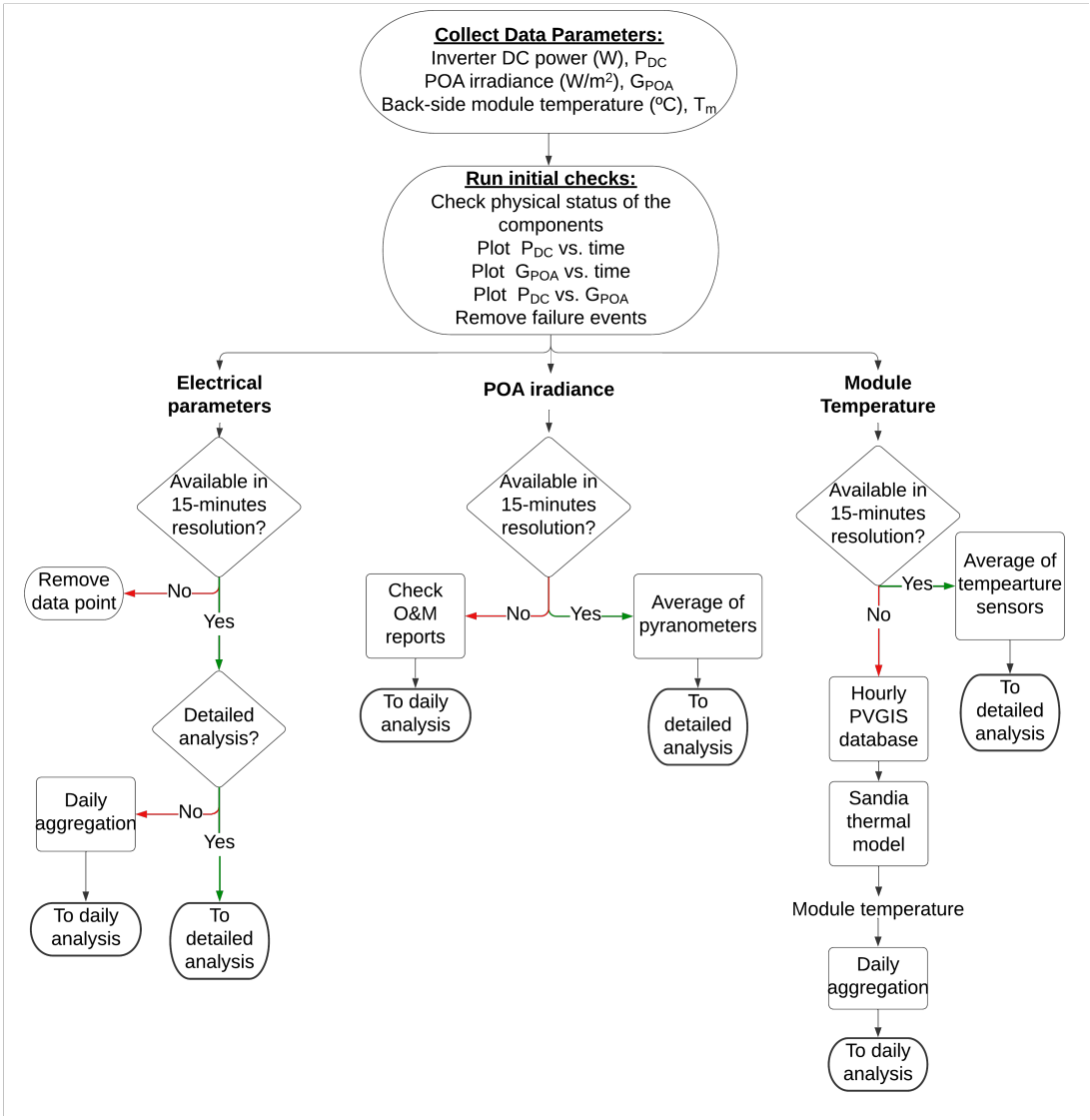

Figure 4.1: Workflow chart data modelling System A

Presently, System A has been operational for 8 years. As PV systems age, they are more likely to accumulate outages or degradation in irradiance or temperature sensors [6]. In order to ensure data integrity and stability, a graphical inspection of every parameter took place as a first approach to detect data gaps, shifts or outliers [52]. Then, POA irradiance and module temperature in the period 2015-2018 are modelled.

4.1.1 Data gaps and shifts

Data shifts and missing data were easily identified by a time series graph of meteorological and production data. The failure conditions were then cross-checked with the O&M reports and the cause was identified in most of the cases. This is detailed in table 4.1. As a consequence, these days have not been taken into consideration in the analysis, as only data points at comparable and failure-free conditions must be selected.

Table 4.1: Failure events System A

Failure start	Failure end	Components	Failure	Cause
22-09-15	22-09-15	Plant	Outage from 10am	DNO Protection relay tripped out
30-10-15	9-11-15	Inverter 3.1	Low production	Low insulation resistance
6-1-16	7-1-16	Plant	Outage	Fast change of the grid frequency
11-1-16	12-1-16	Inverter 5.2	Low production	Mice nests inside DC cables pipes
18-7-16	22-7-16	Plant	Intermittent outages	Strings measurements
15-6-17	20-6-17	Plant	Outage	FAC Test measurements
11-11-17	4-1-18	Inverter 4.1	Reduced power	One combiner box burned out
10-12-17	10-12-17	Plant	Outage	Plant outage due to snowfall
15-4-18	27-9-18	Inverter 1.1, 1.2	Low production	Cable fires and rodent damage
2-6-18	3-9-18	Inverter 6.1	Low production	Cable fires and rodent damage
19-2-19	27-2-19	Plant	Intermittent outages	Preventive LV & HV Maintenance
12-3-19	13-3-19	Inverter 2.1	Outage	DC isolation fault
29-11-19	1-12-19	Plant	Outage	Scheduled DNO outage
22-12-19	30-12-19	Inverter 6.1	Low production	Cables damaged by rodents
9-2-20	13-2-20	Inverter 4.2	Low production	Underground cable fault
1-8-20	2-8-20	Plant	Outage	Main CB has tripped
28-12-20	6-1-21	Inverter 1.2	Lower production	Strings check for isolation faults
28-5-21	2-6-21	Plant	No data	Communication issue
21-9-21	27-10-21	Inverter 4.2	No data	No communication
11-10-21	15-10-21	Plant	No data	DNO outage
15-10-21	24-10-21	Inverter 6.1	Intermittent outages	Ducts replacement
26-12-21	26-12-21	Inverter 3.1	Outage	Unknown
6-2-22	21-2-22	Inverter 5.1	Low production	Low insulation resistance value
19-7-22	22-7-22	Plant	Outage	DNO outage

4.1.2 Intradaily POA irradiance

Besides these temporal failures, as described in chapter 3, the main limitation for System A is that irradiance measurements are only available in a daily resolution for the period 2015-2018. This is a limiting factor regarding the later filtering, which requires intraday values.

The Photovoltaic Geographical Information System (PVGIS) is an online tool which provides information about solar radiation for any location in Europe and Africa, as well as a large part of Asia and America [53]. This tool serves as an alternative to sensor measurements when these are not available or do not fulfil quality conditions in terms of calibration or cleaning, among others. Instead, it uses satellite data from geostationary meteorological satellites to estimate the solar radiation arriving at the earth's surface [54]. The satellite solar radiation data used in PVGIS has been compared with ground station measurements and validated in [55]. Figure

4.2 shows the different solar radiation data sets used in PVGIS. SARAH2 is available until 2020 and will be used for System A's modelling.

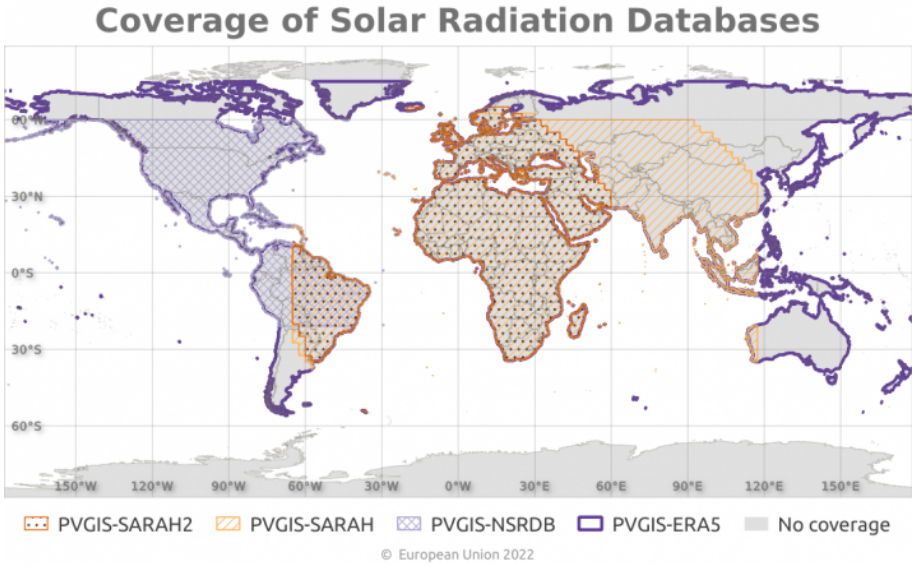

Figure 4.2: PVGIS Coverage of Solar Radiation Database

Then, given as input the location, mounting type, tilt angle of the panels and azimuth, the POA irradiance (W/m^2), wind speed and ambient temperature are obtained for every hour in the period 2015-2018. The simulated values of POA irradiance (G_{sim}) were validated against the corresponding measured values (G_{meas}) using the method described in [7, 56] for the period 2019–2020. A scatter plot of measured vs PVGIS values is shown in fig. 4.3. The statistical parameters used to evaluate the quality of the simulations are the mean absolute error (MAE), and the root mean square error (RMSE) which are defined in eqs. (4.1) and (4.2). Both parameters are then normalized to the mean of the measured irradiance without considering night hours ($G_{meas} > 0 W/m^2$). Results are given in table 4.2.

$$MAE = \frac{1}{n} \cdot \sum_{i=1}^{n} (G_{sim} - G_{meas}) \tag{4.1}$$

$$RMSE = \sqrt{\frac{1}{n} \cdot \sum_{i=1}^{n} (G_{sim} - G_{meas})^2} \tag{4.2}$$

Table 4.2: Statistical parameters associated to measured and PVGIS irradiance in the POA

MAE (W/m^2)	MAE (%)	RMSE (W/m^2)	RMSE (%)
38.38	16.44	81.28	34.82

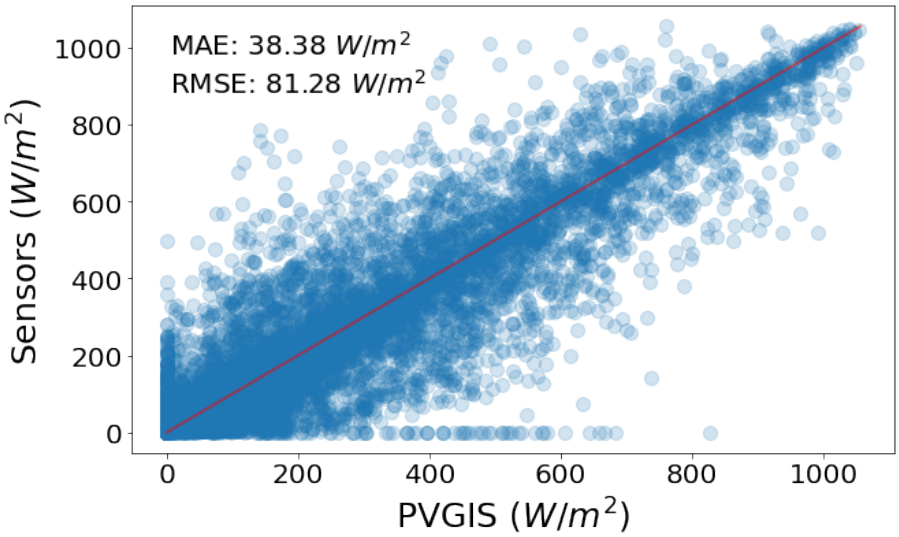

Figure 4.3: Scatter plot of measured vs PVGIS irradiance for the period 2019-2020

After the irradiance is obtained, three different approaches are considered:

1. **Daily values from plant's sensors for the entire period (2015-2022)**.
   This approach will guarantee that all the operational years of the plant are considered and that only data from the plant's sensors are used. However, it doesn't allow intraday filtering, so other filtering methods will be considered.
2. **Hourly data from PVGIS in period 2015-2018 and sensor data from 2019 to 2022**.
   Despite using an external source for the POA irradiance in the first years of operation, this approach will allow the use of intraday filtering. However, as it is seen fig. 4.3, there is a great dispersion between the sensor POA irradiance and the satellite data in an hourly resolution, especially on cloudy days. This error gets lower on a daily basis, but with an RMSE of 34.82% it is decided not to use the PVGIS POA irradiance database to apply the intraday filtering because, due to the weight of irradiance in the PR calculation, it may introduce lots of outliers and noise to the analysis.
3. **15-minutes sensor data from March 2018 to 2022**.
   This last approach reduces significantly the data quantity, as it is just considering half of the operational period of the plant. However, it provides 15-minute data from the plant's sensor for the three main variables: DC power, irradiance and module temperature. With them, it is ensured that intraday filtering is applied and the reliability of this sensor-based analysis is higher.

Overall, as it is mentioned in section 2.2, [36] concludes that the longer the time series, the more reliable the results tend to be, but a minimum of three years of data are required. In this sense, the results obtained in approaches 1 and 3 will be compared in chapter 6 to get an understanding of the importance of data quantity against data quality.

4.1.3 Module temperature

Additionally, a modelling of the module temperature is required due to the lack of back-of-module temperature measurements available during the period 2015-2018. To do so, the Sandia module temperature model will be used to estimate the module temperature during this period. The modelled temperature will be used for the daily analysis of the period 2015-2022.

The Sandia Array Performance Model (SAPM) for the modelling of PV modules and arrays has

been developed at the Sandia National Laboratories since 1992 [57]. It proposes the model in eq. (4.3) to estimate module temperature T_m [51]:

$$T_m = G_{POA} \cdot (e^{a+b \cdot WS}) + T_a \tag{4.3}$$

Where G_{POA} is the solar irradiance incident on the module POA (W/m^2), T_a is the ambient air temperature (°C) and WS is the wind speed (m/s). These 3 variables are the outputs of the PVGIS satellite database. Then, parameter a is a coefficient describing the module's linear thermal response to solar radiation and b is a coefficient describing its response to the wind (forced convection) [57]. These depend on the module type and for System A are detailed in table 3.1.

Therefore, applying the Sandia model, the hourly module temperature for the period 2015-2018 is obtained. It is important to mention that this temperature will be later aggregated into daily values so, although the PVGIS database is considered not accurate enough for the hourly analysis, it is valid in a daily analysis. Also, the influence of temperature in the PR calculation is much lower than irradiation as PV modules are less sensitive to temperature than irradiance. Figure 4.4 shows the daily temperature profile during the whole period (2015-2018) remarking when the PVGIS database and sensors are used.

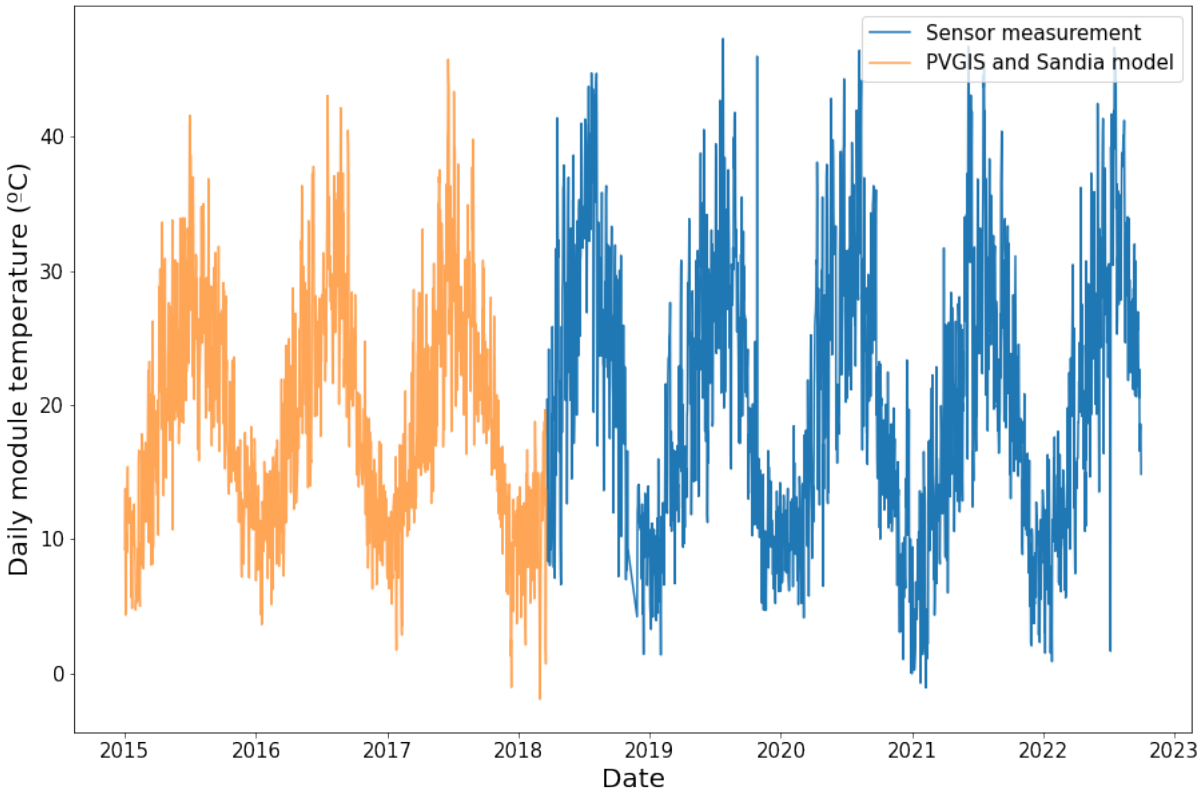

Figure 4.4: Daily temperature in System A for the daily analysis

4.2 System B

Despite the high resolution of the data, System B also presented some limitations in terms of data acquisition mainly driven by changes in the hardware of the PV plant. Also, not all the parameters for the different configurations have been measured with on-site sensors, so modelling is required. Figure 4.5 summarises the workflow process in System B.

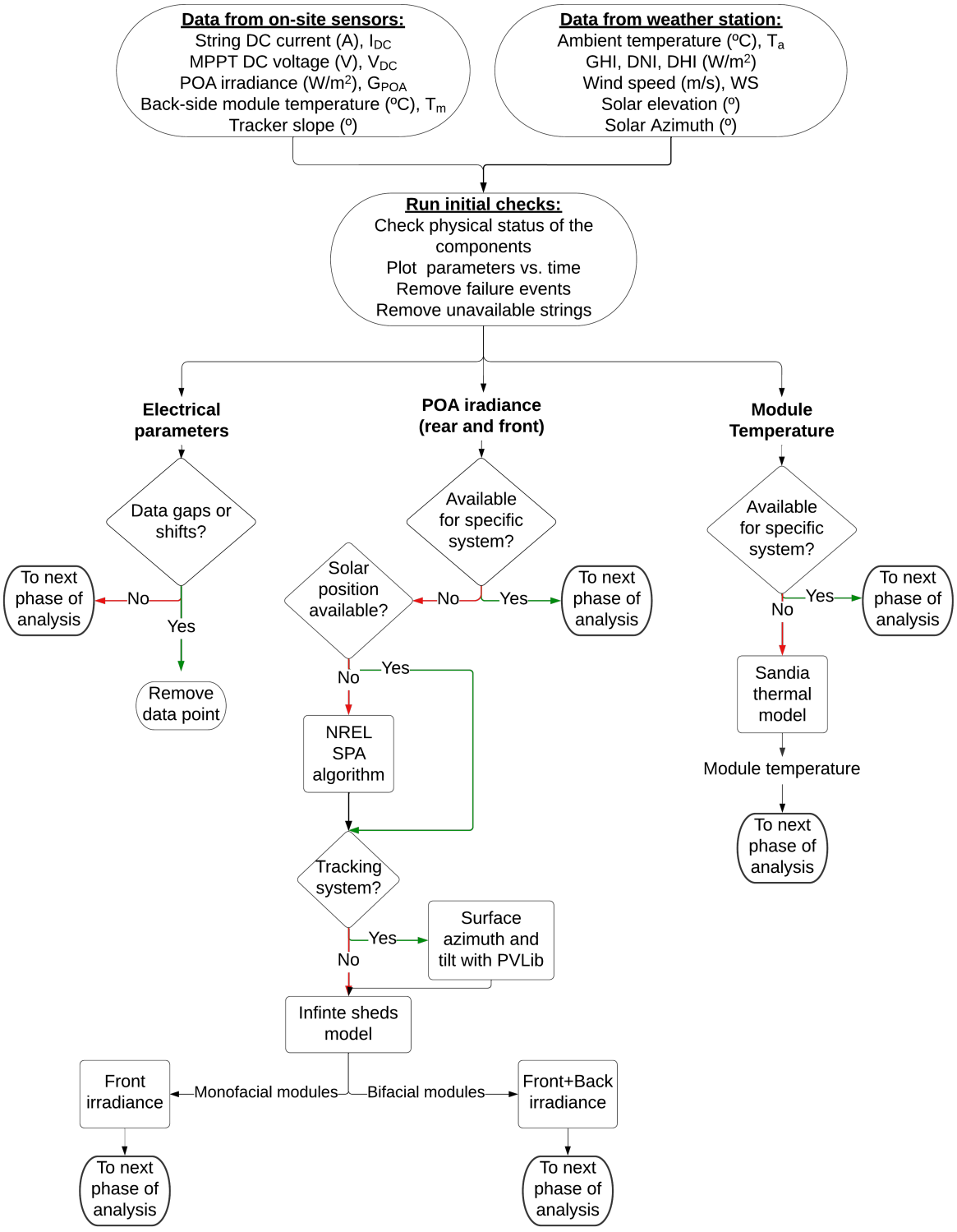

Figure 4.5: Workflow chart data modelling System B

4.2.1 String conditions

Figure 4.6 details the situation of every string between February 2019 and September 2022. Each of the colors represents the status of the string during that month. The main changes have been regularly monitored and are: Changes in tilt angle for the fixed tit systems, changes in module type and changes in the albedo by changing the reflectivity of the ground. Also, periods with no data availability are included in fig. 4.6.

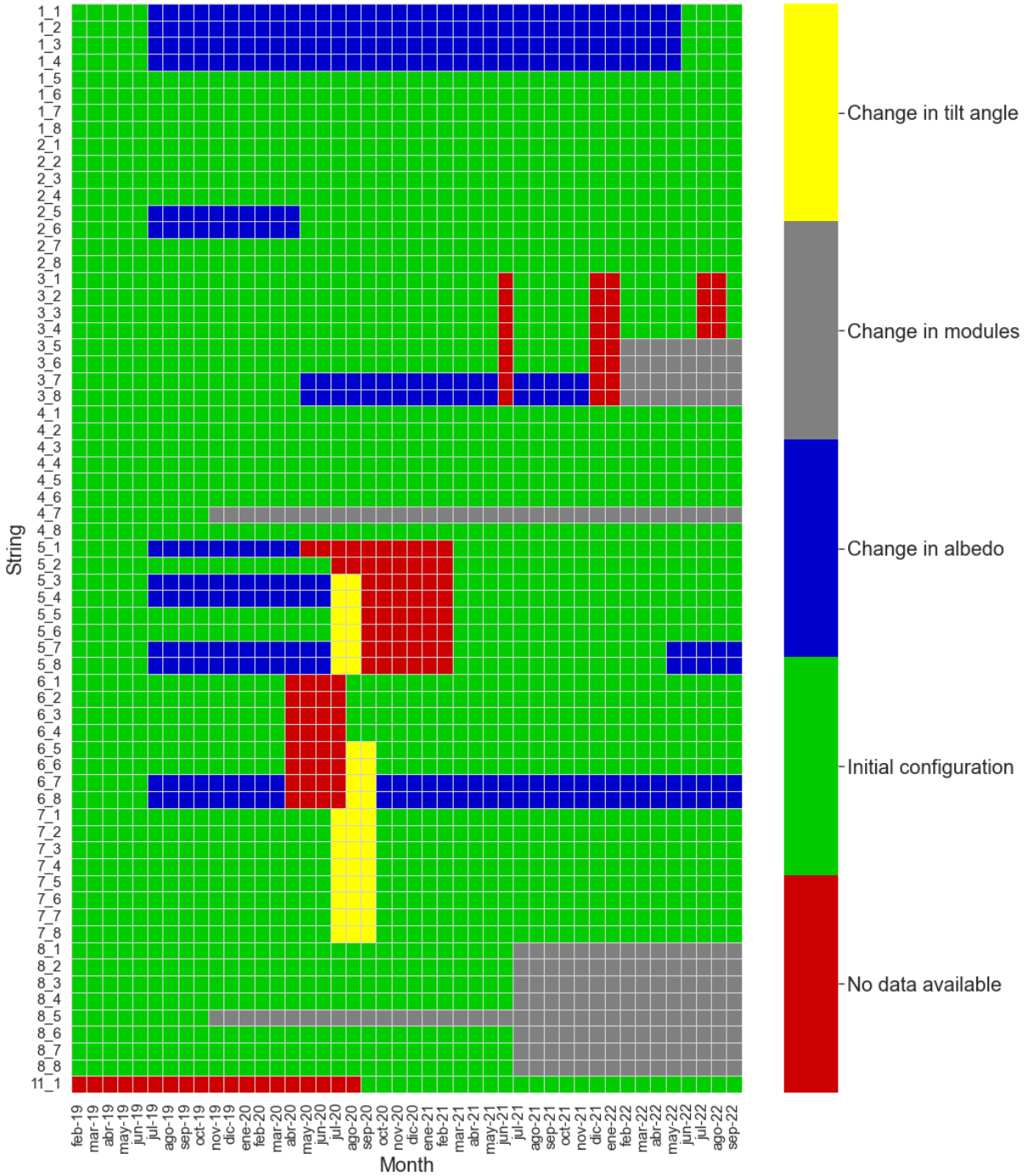

Figure 4.6: String availability System B

As a criteria, only the periods colored in Green are considered during the analysis in order to ensure that the conditions are the same during the whole analysis. Strings with less than

two years of available data are directly removed as this is a requirement to apply the Year on Year methodology. Additionally, the data gaps coloured in Red are either component faults or communication issues that led to missing data. As an example, fig. 4.7 shows a fault that occurred in inverter 3 during the 2022 summer. In fig. 4.8 it is seen the data gap between May 2020 and March 2021. This was also due to an inverter failure which could not be replaced because of the pandemic situation.

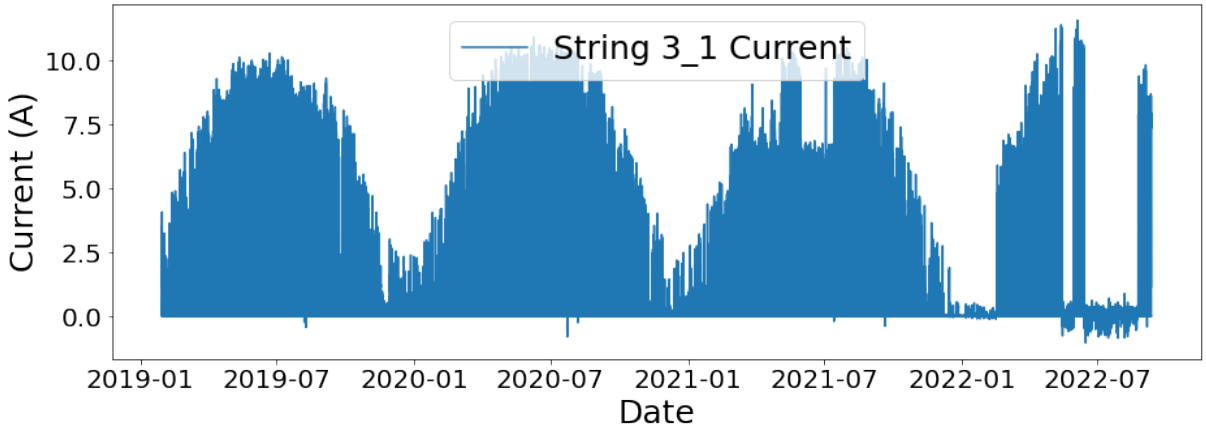

Figure 4.7: Current of the string 3_1 in System B during 2019-2022

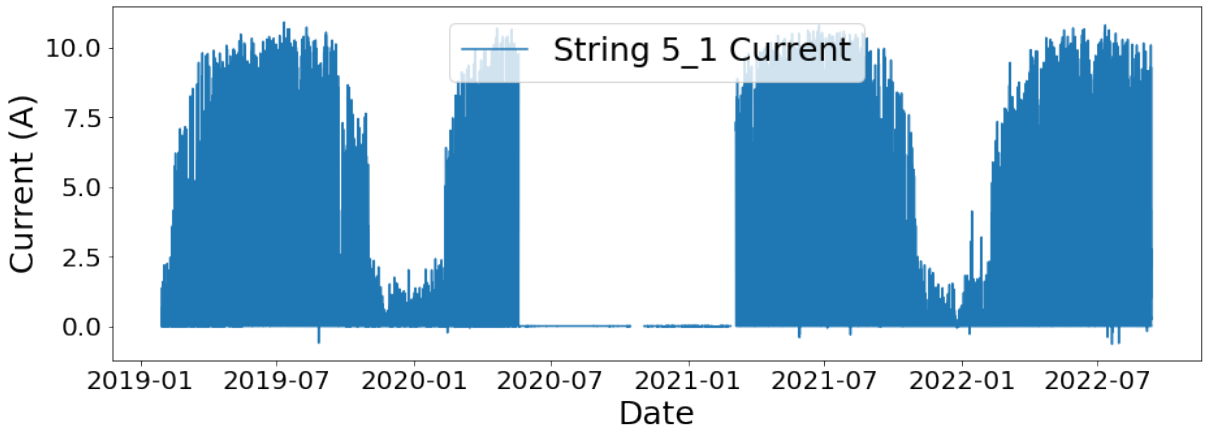

Figure 4.8: Current of the string 5_1 in System B during 2019-2022

In such cases where the energy yield is not available, a data shift correction is not possible because it requires the knowledge of the degradation curve and this is exactly the parameter that will be analysed. Consequently, the removal of these data shifts needed to take place to guarantee uniformity and failure-free conditions [6]. By contrast, other missing parameters such as the solar position or irradiance components can be modelled and this is done in the forthcoming sections.

Finally, from May 2022 Tracker 8 (where the pyranometer is located) was stuck facing west. Consequently, only during half of the day the POA irradiance was correctly measured. Figure 4.9 shows how the slope of Tracker 8 oscillates until the 23rd of May when it gets stuck and remains constant. Then, fig. 4.10 shows the current of another bifacial tracked system (not stuck) against the measured POA irradiance. This period had to be thus removed from the analysis.

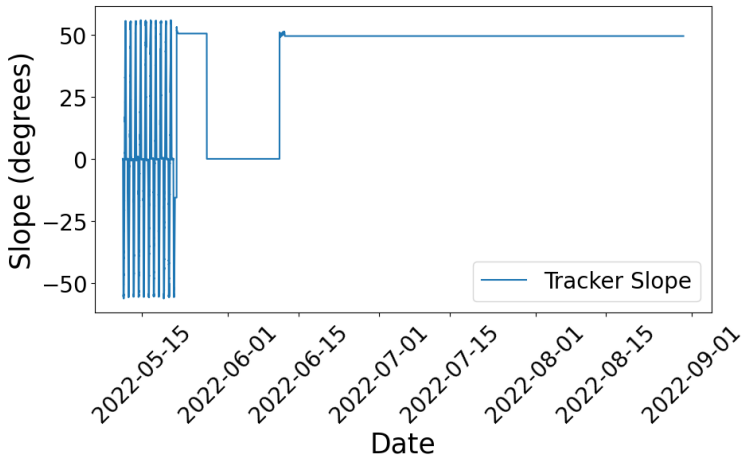

Figure 4.9: Tracker 8 slope before and after being stuck

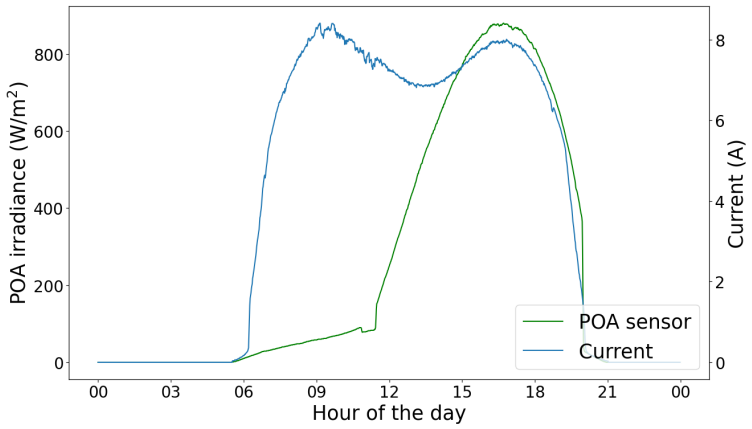

Figure 4.10: Bifacial current and irradiance when the tracker is stuck

4.2.2 Solar position

From System B's weather station, solar zenith and azimuth are obtained. However, some data gaps are observed during the first months of 2019 and 2020 as observed in fig. 4.11. To fill these gaps, PVlib-python functions are used [4].

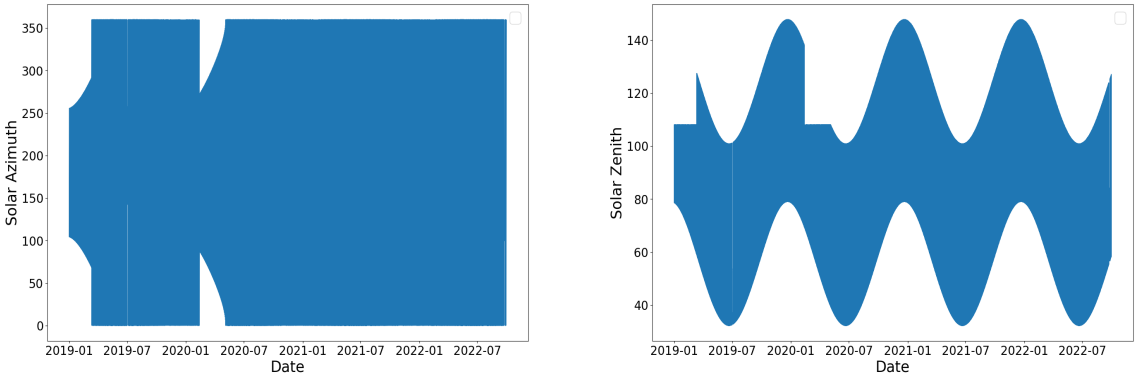

(a) Solar Azimuth

(b) Solar Zenith

Figure 4.11: System B solar azimuth and zenith data from weather station

The PVlib function *solarposition.get_solarposition* implements the NREL SPA algorithm [58], which calculates the solar zenith and azimuth angles with uncertainties of ± 0.0003 degrees based on the date, time, and location on Earth applying the methodology described in [59].

After the modelled azimuth and zenith are obtained, the results are compared with the data from the weather station. It is important to mention that the data logger runs the NREL's SPA to obtain the solar azimuth and zenith. As shown in fig. 4.12, there are only a few outliers in which the PVlib azimuth differs from the measured one. This confirms the reliability of the NREL SPA algorithm and justifies the use of these solar position values during the analysis.

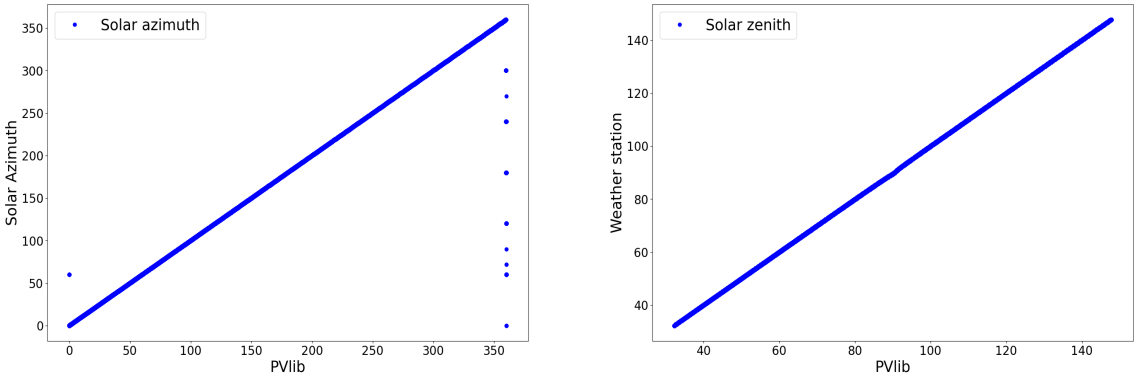

(a) Solar Azimuth (b) Solar Zenith

Figure 4.12: Solar Azimuth and Zenith modelled VS weather station

4.2.3 Tracking system

Another main data absence is the back irradiance that the bifacial modules receive. In the case of the tracking system, the module surface tilt and azimuth vary during the day, so they need to be calculated for every time step prior to the back irradiance modelling.

Surface azimuth and tilt angles

Firstly, the PVlib function *tracking.singleaxis* is used to determine the rotation angle of a single-axis tracker using the equations in [60] for a given sun zenith and azimuth angle. Other inputs to the function are the axis tilt, axis azimuth, maximum rotation angle and GCR of the tracker system. Also, the backtracking to avoid row-to-row shading is activated. The results of the surface tilt and azimuth are shown in fig. 4.13. As expected, the surface azimuth is either 90 or 270 degrees and the surface tilt varies between 0 and 60 degrees.

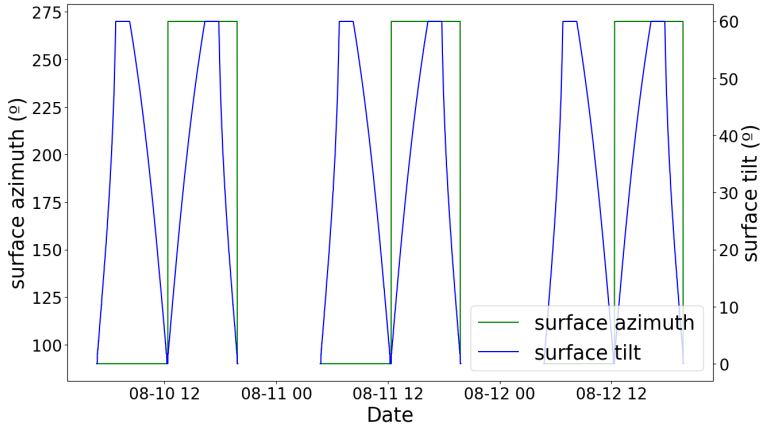

Figure 4.13: Surface azimuth and tilt angles for the tracking system

Back irradiance

Then, an additional PVlib function is needed to model the back irradiance for tracking systems with bifacial modules. The function *bifacial.infinite_sheds.get_irradiance* calculates the front and rear irradiance using the infinite sheds model detailed in [61]. The model assumes that the PV system comprises parallel and evenly spaced rows on a horizontal surface, and calculates the irradiance at a location far from the ends of any rows assuming that the rows (sheds) are infinitely long. This function is also used for the bifacial fixed-tilt modules (section 4.2.4) so the input parameters given to the model are included in table 4.3.

Table 4.3: Back irradiance modelling inputs

Parameter	Fixed-tilt	Tracker
Surface tilt (º)	25	From section 4.2.3
Surface azimuth (º)	180	From section 4.2.3
Solar zenith (º)	From section 4.2.2	
Solar azimuth (º)	From section 4.2.2	
GCR (-)	0.4603	0.2915
Axis height (m)	2.3	1.95
Pitch (m)	7.6	12
GHI (W/m^2)	From weather station	
DHI (W/m^2)	From weather station	
DNI (W/m^2)	From weather station	
Albedo (-)	0.2	
Bifaciality (-)	0.67	

The GCR is the ratio between array length and row pitch, calculated as in eq. (4.4) for fixed-tilt and tracking systems:

$$GCR = \frac{N°modules\_portrait \cdot Module\_lenght + Space\_modules}{Row\_pitch} \tag{4.4}$$

Given these inputs, the model accounts for the restricted view of the sky and ground from module surfaces due to the nearby rows. It also implicitly assumes that diffuse irradiance from the sky is isotropic and that module surfaces do not allow irradiance to transmit through the module to the ground through gaps between cells.

The results of the infinite sheds model are shown in fig. 4.14 and fig. 4.15. The outliers seen in fig. 4.14 between February and Match of 2021 are due to the calibration of the GHI sensor during this period. For this reason, this period will be deleted from the analysis. In fig. 4.15 it is shown a detailed comparison of the front and back POA irradiation in the tracking system during three days in August 2020. These days were chosen as an example to illustrate the results of the modelling. Similar to other studies [62, 63], the back irradiance represents around 10% of the front irradiance, confirming the reliability of the results.

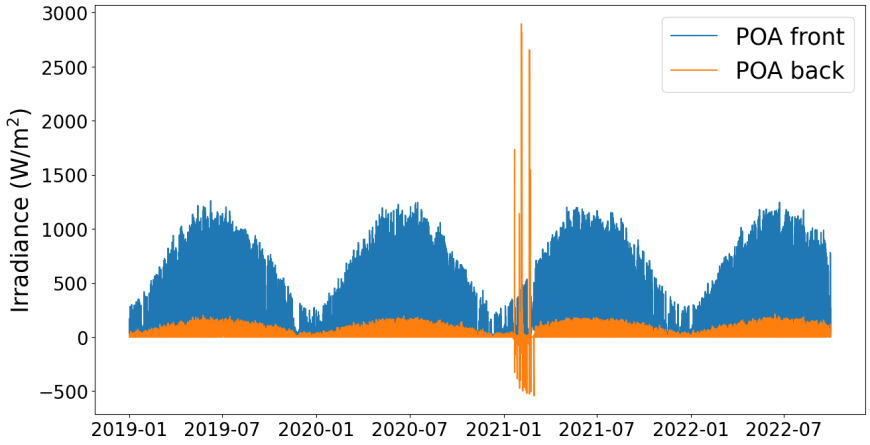

Figure 4.14: Front and back POA irradiance for the tracking system

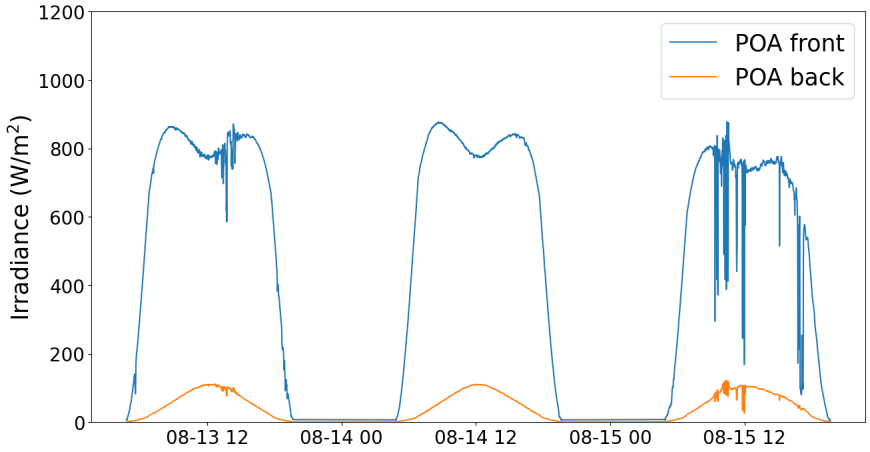

Figure 4.15: Front and back POA irradiance for the tracking system detailed

4.2.4 Fixed-tilt system

In the case of the fixed-tilt systems, the back-side irradiance had to be modelled for the bifacial modules. This was following the method described in section 4.2.3 with the inputs in table 4.3. The detailed results are shown in fig. 4.16. Being a fixed-tilt system the peak in irradiance occurs at solar noon, differing from the tracking system (fig. 4.15). A graph that shows the complete period has been omitted because it is almost identical to fig. 4.14.

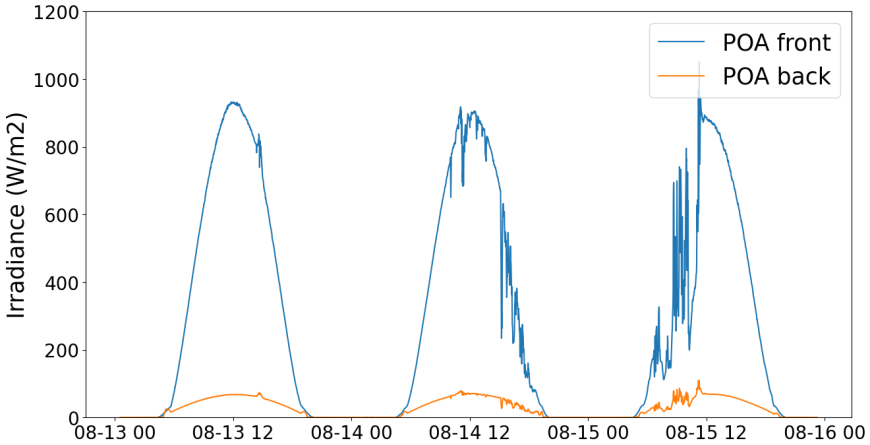

Figure 4.16: Front and back POA irradiance for the fixed-tilt system detailed

Module temperature

As it is explained in section 3.2.5, the on-site module temperature sensor installed in System B at the beginning of the plant's operation was on the tracking system. Therefore, the module temperature for fixed-tilt systems is not available and needs to be modelled. This was done with the Sandia model using eq. (4.3) (detailed in section 4.1.3). In this case, as there are two different construction methods for monofacial (glass/polymer) and bifacial (glass/glass) modules, the parameters a and b in eq. (4.3) are set according to the recommended coefficient values for these bill of materials (table 3.5). A comparison between the back-sheet temperature for monofacial and bifacial fixed-tilt modules for a sunny summer day and cloudy winter day is shown in figs. 4.17 and 4.18. It is seen that bifacial modules reach higher temperatures on days with higher irradiance. Especially in solar noon, the difference between both is the highest. On the other hand, both have similar temperatures on cloudy days with lower irradiance. In [64] it is suggested that only at rear irradiance fractions beyond 15%, the additional heat input from the back side can cause the glass/glass bifacial modules to be hotter than the white back sheet monofacial ones. This mismatch between [64] and the results shown in fig. 4.17 may be driven by the assumptions considered in the temperature modelling.

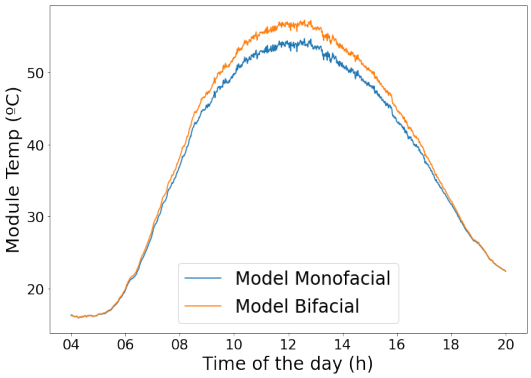

Figure 4.17: Modelled module temperature for monofacial and bifacial modules on a sunny summer day (16-8-2020)

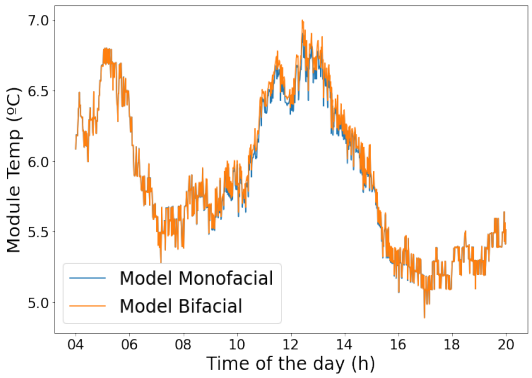

Figure 4.18: Modelled module temperature for monofacial and bifacial modules on a cloudy winter day (24-1-2022)

Additionally, two new module temperature sensors were installed in System B's fixed-tilt modules in April 2021. These sensors were installed in both, monofacial and bifacial systems. Thanks to them, the temperature modelling can be tested and its reliability verified.

Firstly, fig. 4.19 shows a comparison of the monofacial sensor and the modelled module temperature. It is observed that the modelled temperature is higher during night hours and at the beginning of the day, but they both reach similar values around noon. One of the Sandia Model's disadvantages is reflected here, as it is designed for steady-state conditions and does not take into account the thermal capacitance of the module, which makes the module warm up and cool down slower than in the modelling. However, taking into account the slight difference between the model and the sensor's measurement and the impact that the temperature will have on the power correction, the simulation is considered a reliable source for the module temperature.

Regarding the bifacial modules, fig. 4.20 shows the great difference between the modelled temperature and the sensor measurement. As it is mentioned in section 3.2.4, this sensor was found to be loose from the back-sheet of the module, so lower measurements from the sensor are seen in fig. 4.18 as expected. Applying a temperature which was measured with a constantly detaching sensor would lead to incorrect results as PR decreases with higher temperatures. In the cases in which a period with the fully attached sensor is found, a correction can be made

by fitting the modelled temperature to the measured one in this period [46]. However, slow detaching occurred since the beginning of its installation, so in this case, the only reliable source for module temperature is the modelled one.

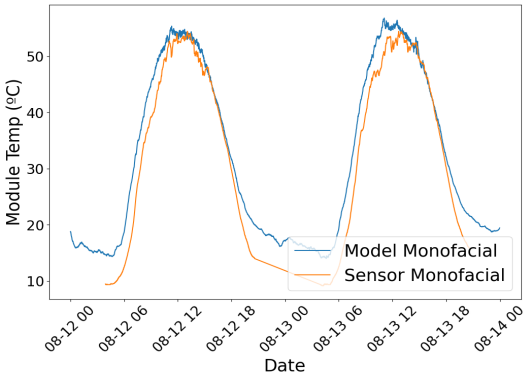

Figure 4.19: Modelled and sensor module temperature monofacial

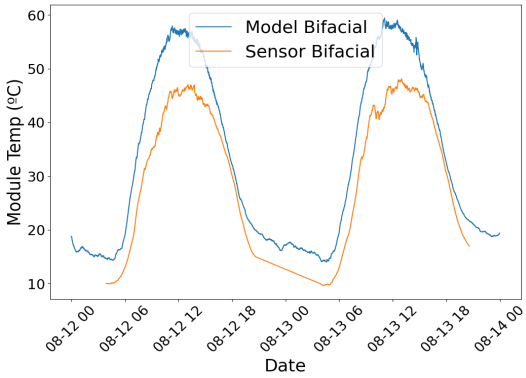

Figure 4.20: Modelled and sensor module temperature bifacial

The temperature distribution of temperatures in System B is shown in fig. 4.21. For the tracking systems, although the sensor is located in a monofacial module, the same temperature is considered for the bifacial tracking module. Each of the system's average temperature is also included, being slightly higher the measured tracker monofacial temperature.

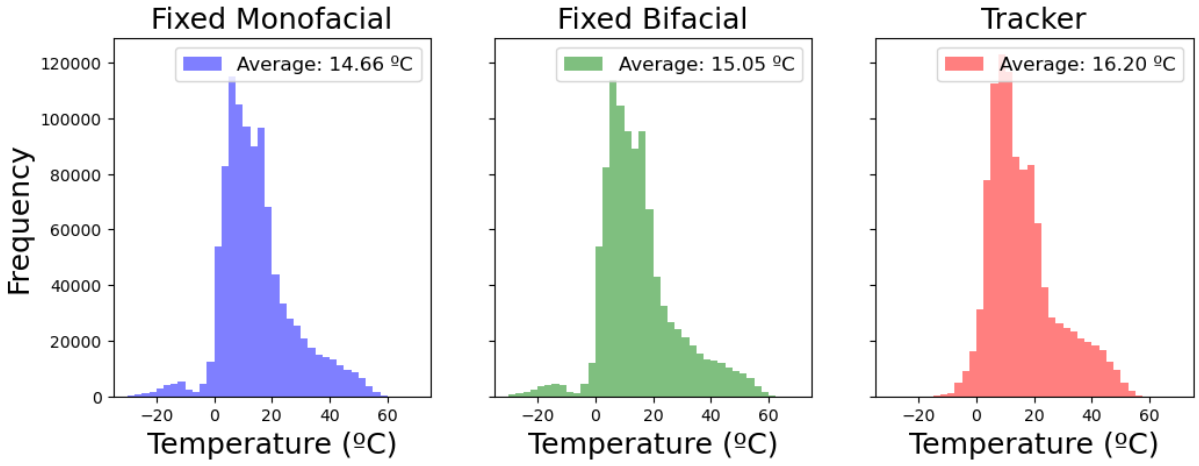

Figure 4.21: Fixed monofacial (modelled), bifacial (modelled) and tracker monofacial (sensors) histogram of module temperatures

In conclusion, this chapter highlighted the various challenges that can arise when working with limited data sets from the sensors and the use of certain modelling techniques to overcome these limitations and improve the accuracy and reliability of the data. Chapter 5 delves deeper into the specific steps taken to obtain the degradation rate of each component of the systems.

5 Methodology

This section will describe how the Year on Year (YoY) method from RdTools [5] is applied to both systems to obtain the degradation rate of their components.

This method has been put forward as a standard for calculating performance degradation rates [42]. By measuring the median, outlier effects due to seasonal variation and data errors are mitigated [34]. In this way, this method has been shown to be less susceptible to outliers, marked seasonality, or strong soiling events compared to traditional regression-based methods [65]. Also, less stringent data filtering may be required so it is less sensitive to the leverage of start and end points in the analysis.

However, two years of data are the minimum requirement for this approach in contrast to the regression, so this could limit the application if there is a non-linear degradation and it is desired to calculate the degradation for shorter time periods [66]. Figure 5.1 shows a graphical overview of the workflow process that is described below.

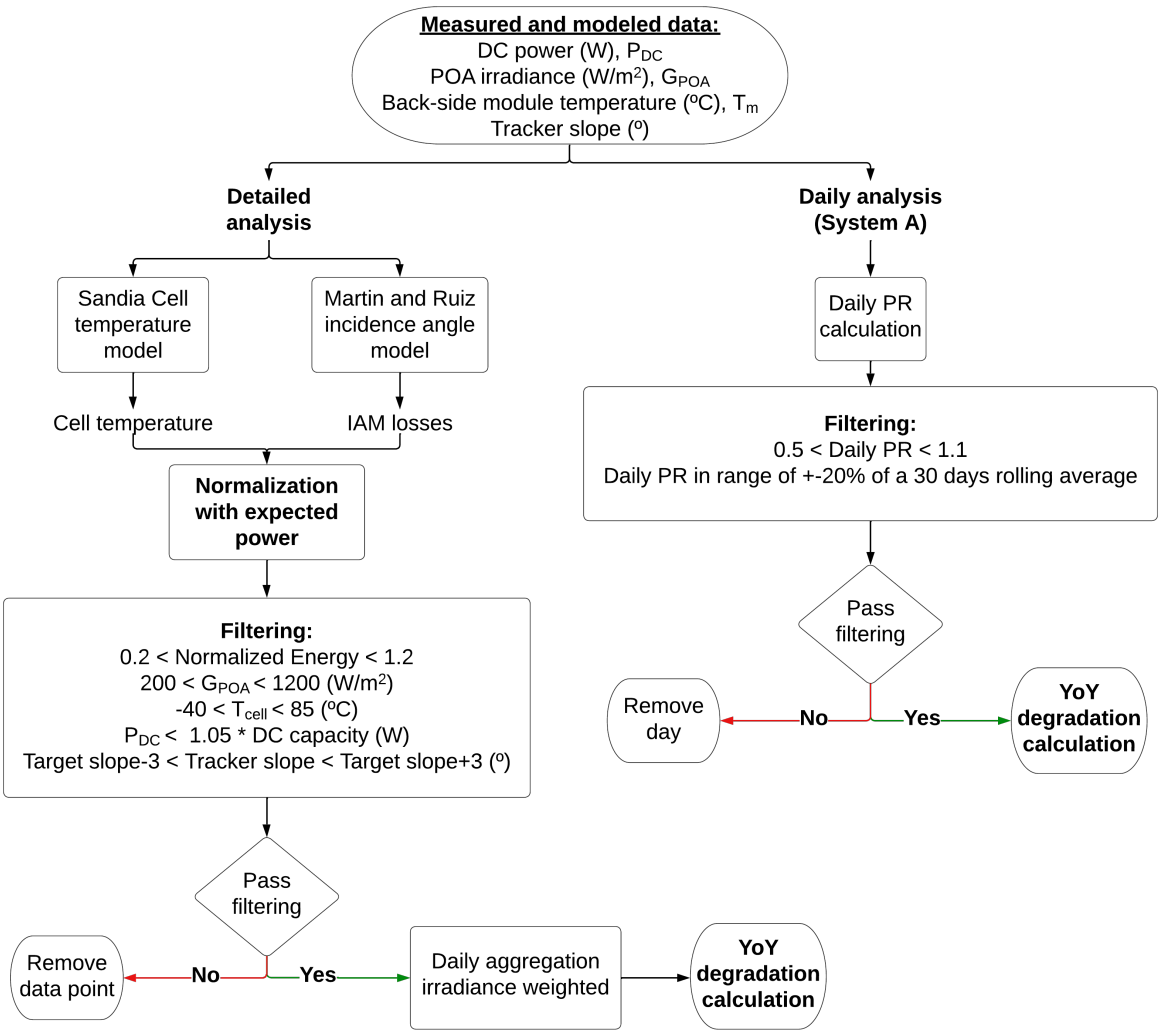

Figure 5.1: Workflow YoY methodology

The main four steps of this methodology are: Data acquisition and preliminary calculations, normalization, filtering and degradation calculation. These steps will be applied identically to System A's inverters from March 2018 to September 2022 and to System B's strings in the period between February 2019 and September 2022. Then, in section section 5.5 a modified version of this methodology with daily values will be applied to system A from the beginning of its operation (2015-2022).

5.1 Data acquisition and preliminary calculations

This section prepares the necessary data for the RdTools YoY calculation. The next step of the method is normalization, which requires a time series of energy yield, cell temperature and irradiance. In order to minimize inverter effects, the analysis is based on DC power data for both systems. POA irradiance and module temperature raw data are imported as described in the previous sections. To be fully consistent with the method, cell temperature must be obtained before the degradation rate calculation. Also, despite not being required by the RdTools developers, angle of incidence losses will be considered to remove variability at low sun angles.

5.1.1 Cell temperature

Sensor and modelled temperatures refer to the back-sheet module temperature. For the power correction, both module temperature data sources are converted into estimated cell temperature. Therefore, the Sandia cell temperature model [67] will be used, which derives the cell temperature from module temperature, T_m, the plane of array irradiance, G_{POA}, and a temperature difference parameter, ΔT. This difference parameter represents the higher operating temperature of a cell compared with the module back sheet at a reference irradiance. According to [68], PV cell temperatures are estimated by adding 3.0°C per 1000 W/m^2 irradiance to the PV module back-surface temperature. Other authors [40, 69] estimate ΔT to be 2.5ºC. In this case, ΔT is defined in tables 3.1 and 3.5 independently for monofacial and bifacial modules based on the recommended literature [51]. The model uses eq. (5.1) to calculate the cell temperature T_c:

$$T_c = T_m + \frac{G_{POA}}{G_{STC}} \cdot \Delta T \tag{5.1}$$

Where G_{STC} is the Standard Test Conditions irradiance (1000 W/m^2).

The cell temperature is calculated for every time step in each of the components of both systems and it will be used for the corrections instead of the module temperature.

5.1.2 Angular response correction

The angle of incidence (AOI) correction accounts for increased reflection losses when the incident angle of the solar radiation impinging the module surface increases [68]. A correction based on Martin and Ruiz incident angle model is used to calculate a derating factor, IAM, which provides the useable fraction of the POA irradiance not lost due to AOI effects.

Martin and Ruiz establish in [70] that the angular losses of PV modules are a function of the solar angle of incidence and the angular losses coefficient (a_r). Firstly, the AOI is obtained for every system, considering the surface tilt and azimuth (different for fixed tilt and trackers), with the PVlib function *pvlib.irradiance.aoi*. Figure 5.2 shows the differences between the AOI for fixed tilt and trackers in System B. Then, Martin and Ruiz incident angle model is applied with *pvlib.iam.martin_ruiz*, which uses eq. (5.2) as described in [70]:

$$IAM = \frac{1 - exp(-cos(\frac{AOI}{a_r}))}{1 - exp(\frac{-1}{a_r})} \tag{5.2}$$

The coefficient a_r is set to 0.16 by default. It is also important to note that eq. (5.2) is only valid for AOI between -90 and 90 degrees and IAM is constrained to 0 outside this interval. Thus, IAM=1 at AOI=0º, and IAM=0 at AOI=90º. Figure 5.3 shows the IAM losses factor as a function of the AOI.

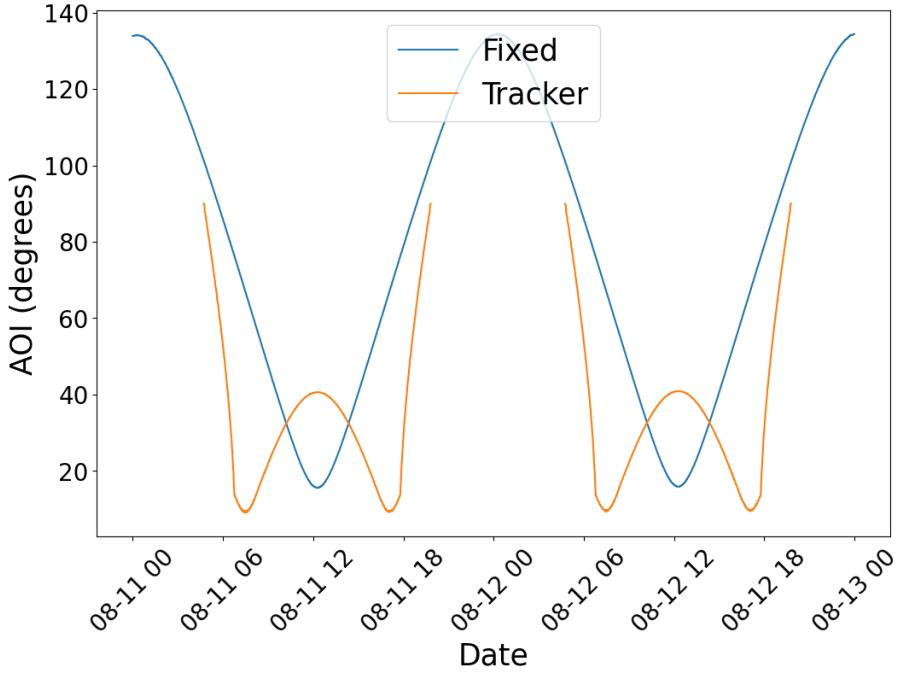

Figure 5.2: Example of the AOI for fixed tilt and tracker

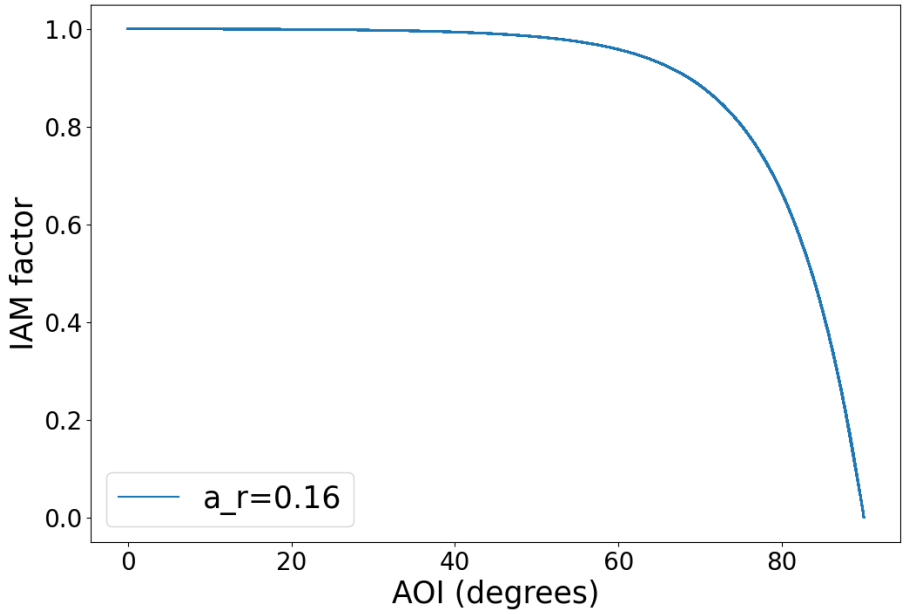

Figure 5.3: IAM factor with respect to the AOI. It is based on Martin and Ruiz model

As it is a reflection loss, the most precise way to apply the IAM loss coefficient is on the direct normal irradiance (DNI). However, as the input data is based on tilted pyranometers in the POA, separate measurements of diffuse irradiance in POA or direct normal irradiance are not

available. Therefore, instead of applying the IAM losses to the DNI, the IAM correction factor is only applied on the global POA irradiance on the individual clear-sky (CS) time steps [68, 71]. In these clear-sky situations, most part of the irradiation comes from the DNI component, so it is considered a valid approach when applying the angular response correction.

To identify the clear-sky time steps, the PVlib library *Location.get_clearsky* calculates the clear sky estimates of GHI, DNI, and DHI at a specific location. Then, *irradiance.get_total_irradiance* transposes GHI clear-sky data to POA irradiance so that it is now comparable with the POA measured from the pyranometers on site. To differentiate between clear and cloudy-sky time steps, the clear-sky (CS) index in eq. (5.3) is defined as the ratio between the irradiance measured with the pyranometer and the simulated clear-sky irradiance in the POA at a ground level calculated with the PVlib library. Although the clear-sky index is usually calculated for a horizontal surface, it can also be calculated for an inclined surface [72]. In accordance with [52, 71], a threshold value of 0.5 is used to separate clear and cloudy sky periods. That means that irradiance measurements with CS index values bigger than 0.5 are classified as clear-sky values, while those below 0.5 belong to cloudy skies.

$$CS = \frac{G_{meas,pyr}}{G_{clearsky}} \tag{5.3}$$

The clear sky index is computed and plotted for the whole data set. Figure 5.4 shows data for two example days. Figure 5.4.a is a sunny day which exhibits a smooth sinusoidal-shaped solar radiation profile. By contrast, fig. 5.4.b's POA irradiance profile is full of vertical perturbations indicating the presence of clouds and with a CS index below 0.5 during most of the day. It is important to mention that the clear-sky index should always be between 0 and 1. In fig. 5.4.a it is higher than one, which can be linked to measurement errors from the pyranometers or a transposition error of the PVlib clear-sky horizontal irradiance.

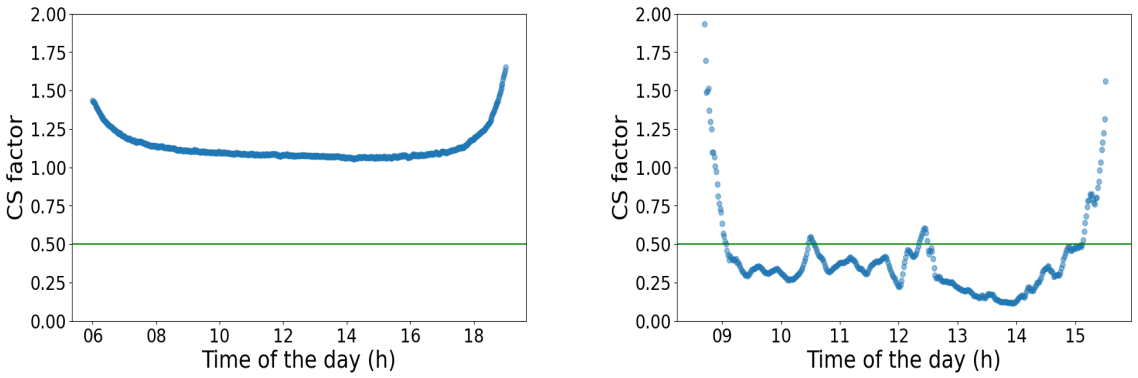

(a) Clear-sky day (11/8/2022)

(b) Cloudy day (12/12/2021)

Figure 5.4: Example of clear-sky index for a clear and cloudy-sky day in System B

Finally, the Incident Angle Modifier losses are multiplied by the front POA irradiance only in the time steps in which the clear sky conditions are met. For the time steps in which the CS index is lower than 0.5, the IAM losses coefficient is set to 1, so no angle of incidence correction is applied.

5.2 Normalization

Once the required data is prepared, normalization is achieved by calculating the expected power, P_{dc} (W), for every time step using the NREL's PVWatts DC power model [73]:

$$P_{dc} = \frac{G_{POA}}{G_{STC}} P_{dc0}(1 + \gamma_{pdc}(T_{cell} - T_{ref})) \tag{5.4}$$

Where the input parameters are:

- **G_{POA}**: The effective irradiance (W/m^2) transmitted to the PV cell. In the case of bifacial modules, the front and back irradiance are considered. Angle incidence losses are applied to the front irradiance as described in section 5.1.2.
- **P_{dc0}**: The nominal DC capacity (W) of each string or inverter.
- **γ_{pdc}**: The temperature coefficient in power (%/ºC). It is based on each module's data sheet (chapter 3).
- **T_{cell}**: Cell temperature (ºC) according to section 5.1.1.
- **T_{ref}**: Cell reference temperature (ºC). PVWatts defines it to be 25ºC, which corresponds to standard test conditions (STC). Despite being a discussion topic between analysts, using STC reference temperature is also recommended in [6, 7, 42].

After the expected power is obtained, the produced power is normalized to the expected power with the function *rdtools.normalize_with_expected_power* [5], which applies eq. (5.5) after converting the power to energy (Wh) based on the frequency of the data.

$$E_{norm} = \frac{E_{produced}}{E_{expected}} \tag{5.5}$$

This normalized energy is equivalent to a temperature, irradiance, and AOI-corrected performance index. Figure 5.5.a shows the unfiltered normalized energy for one of the strings in system B.

5.3 Filtering

Data filtering is used to exclude data points that represent invalid data, create bias in the analysis, or introduce significant noise. It is imperative that filtering is a crucial step in the degradation rate calculation, as it involves many decisions which can lead to a large range of possible outcomes. Due to the lack of standard filtering criteria [65], the recommended four RdTools filters along with other system-specific filters will be applied. As it is mentioned in section 2.3, soiling is difficult to measure but using the YoY method instead of linear regression reduces the effect associated with seasonal soiling. Therefore, no soiling filtering is considered.

Firstly, the normalized energy is filtered between 0.2 and 1.2. This filter removes outages and ensures that the data makes physical sense. If the normalized energy is lower than 0.2 means that either there has been an outage or a failure in some of the components which may bias the analysis. As the main interest is on module degradation, outages are a temporary abnormality and may be removed to determine the typical performance [65]. Second, low irradiance conditions are often associated with night time, errors due to inverter start-up and non-linearity between power and irradiance [7]. Therefore, a low POA irradiance cutoff is set in 200 W/m^2 to remove early morning and late evening periods with these start-up issues, without removing winter data [6]. Also, an upper limit to the POA irradiance is set at 1200 W/m^2 to avoid

cloud brightening or measurement errors from the sensor. Third, the anomalous temperatures outside the range of -40ºC and 85ºC, which are the minimum and maximum operating temperatures according to the module datasheet, are removed. Then, inverter clipping is filtered out by excluding periods during which the power was higher than 105% of the nominal capacity. If the region of inverter saturation is not excluded from the evaluation, the analysis can be significantly biased towards lower degradation [66]. Finally, a filter only for the tracking systems is included. The tracker angular position is compared with the target angular position for every time step. This filter removes periods in which the difference between the tracker's slopes is higher than 3 degrees. An overview of all these filters is included in fig. 5.1.

It is important to mention that as the filtering increases around the median of the filtering parameter, so does the "cleanliness" of the data set meanwhile the uncertainty decreases. If the filtering continues to tighten, a greater number of data points are removed from the data set, ultimately resulting in an increase in uncertainty again. Between those two extremes is a region where the uncertainty is relatively constant [52]. Table 5.1 summarises the different filters applied and the remaining data after each of them. It is seen that the irradiance threshold filter is the most determinant and that temperature and clipping filters did not lead to any exclusion data points. In fig. 5.5 it can be appreciated the daily normalized energy before and after the filtering.

Table 5.1: Effect of the filtering on the analysis

Filter	No filter	Norm. Energy	Irradiance	Temp + Clip	Tracker
Days to analyse (%)	100	96.95	80.40	80.40	76.98

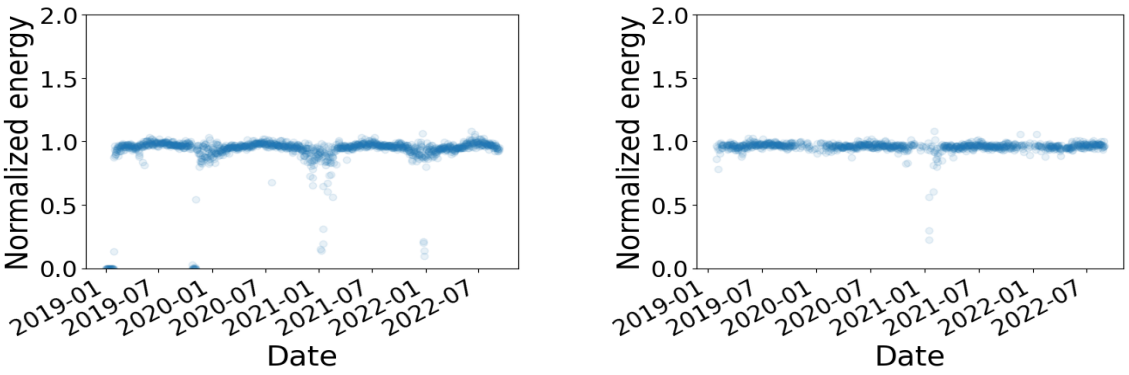

(a) Before the filtering

(b) After the filtering

Figure 5.5: Daily normalized energy in String 4.3 of System B

5.4 Degradation rate analysis

Once the filtering is completed for every component, the filtered normalized energy time series are aggregated to daily values using irradiance weighted averages. Using a weighted average helps to reduce the impact of high-error data points with low irradiation (morning and evening) thus smoothing the normalized energy signal. A longer aggregation would lead to a big reduction in the number of points to be analysed.

The normalized daily values are then analysed to estimate the degradation rate representing the PV system behaviour. In the YoY decomposition approach, a line between daily aggregated

points in subsequent years is drawn to determine a rate of change between these two specific points. This procedure is repeated for the remaining data points of that year and subsequently all years. The result is a histogram of degradation rates in which the median represents the long-term system performance, which is normalized to the first year's median system capacity [6, 36, 66]. The results are visualized as a histogram including a Monte Carlo-derived 68.2% confidence interval of the slope, which depends on the number of data points and the standard deviation of the distribution [34].

5.5 Daily analysis System A

As it is explained in section 4.1, the POA irradiation from the pyranometers in System A is only available in a daily resolution in the first 3.5 years of operation. Daily values don't allow the intraday filtering detailed previously so, in order to utilize this data, it has been decided to use the temperature-corrected daily Performance Ratio (PR) as the parameter to analyse. The PR is a unitless parameter between 0 and 1, which describes the relationship between incoming irradiation and produced energy, indicating the overall effect of losses. As DC energy is used, only losses attributable to the PV array are accounted for, while losses attributable to BOS inefficiencies or failures (e.g. inverter losses) are excluded.

DC energy, irradiation and module temperature in 15-minute resolution from the period 2018-2022 have also been aggregated daily to be consistent during the whole analysis period (2015-2022). The weather-corrected PR is calculated with eq. (5.6) for every day:

$$PR_{corr} = \frac{\frac{E_{produced}}{P_{dc0}}}{\frac{G_{POA}}{G_{STC}} \cdot (1 + \gamma_{pdc} \cdot (T_m - T_{ref}))} \tag{5.6}$$

Where all the parameters have been already defined in previous eqs. (5.4) and (5.5).

Once the daily performance ratios are calculated, the first step is to delete the days which were not under failure-free conditions, detailed in table 4.1. Regarding the filtering, the range of daily PR has been set between 0.5 and 1.1 to exclude other possible failures or incorrect measurements. Then, an additional filter is applied to remove outliers. This second filter considers only points whose daily PR is within the range of $\pm$ 20% of a 30-day rolling average. This range was selected because taking into account the seasonal oscillation of the PR, there is no physical reason apart from malfunctions or measurement uncertainty, why PR should differ more from the last 30 days' average. In this way, around 92% of data points are validated.

Finally, the Year on Year degradation analysis is applied to the PR daily values as described in the previous section. The results of the daily analysis of System A in the period 2015-2022 will be compared to the detailed analysis in a shorter period (2018-2022) in chapter 6.

5.6 Site visit and module testing

After the results were obtained, a site visit to System B took place. During this site visit, PV panels, inverters, tracking systems and other measuring equipment were inspected to ensure that everything is working properly. This involved checking for any visible damage or wear and tear on the panels, inspecting the wiring and connections, and verifying that the tracking systems were functioning correctly. Also, the thermocouples were inspected to ensure that they were still properly adhered to the back of the modules. In fact, during this visual inspection in the field, it was found out that the module temperature sensor in the bifacial fixed tilt module was unattached from the back sheet of the module.

(a) 5 modules dismounted before during site visit

(b) Cable disconnection before module dismounting

Figure 5.6: System B during the site visit and module dismounting

Additionally, the main objective of the site visit was the flash and EL testing of some modules in a controlled laboratory environment. This was done to verify that the modules meet certain performance standards, identify any potential issues, quantify the real degradation of its main parameters and check the reliability of the results obtained from the data analysis. To do so, 5 modules from each type of string were dismounted and taken to the laboratory. A total of 20 modules were tested from the following strings: 3.3, bifacial and tracker; 4.6, monofacial and tracker; 6.1, bifacial and fixed tilt; and 7.5, monofacial and fixed tilt.

Unfortunately, the modules were not flash-tested before their outdoor deployment in 2018, so the reference to compare the results from the flash tests had to be either an unfielded module from the same batch or the datasheet. In the case of bifacial modules, there was a spare module available which had never been in the field, so this was used as a reference. It is assumed that the reference panel has no degradation. By contrast, the only spare monofacial Trina module in the laboratory had different characteristics so the reference used in this case is the module's datasheet.

Once the modules were in the lab, the first step was their cleaning and labelling to remove any residue that could have accumulated. In the case of bifacial ones, the cleaning was done in both glass covers. Then, a visual inspection of the used module against the reference one took place prior to the flash testing.

5.6.1 Comprehensive visual inspection

Modules were thoroughly inspected for visual defects such as small cracks, interconnect imperfections, "browning" of the encapsulant or the formation of hot spots. During the visual inspection, no signs of physical damage to the module's surface or corrosion were detected. A slight brightening in the color of the monofacial module's glass was observed, which may be linked to a partial loss of the anti-reflective coatings. However, there is no definite evidence to ensure a change in the thickness of the AR coating just by shining a white light on the surface, so a more precise inspection method is needed.

Figure 5.7: Visual inspection of the monofacial module. Left: Fielded module. Right: Reference module

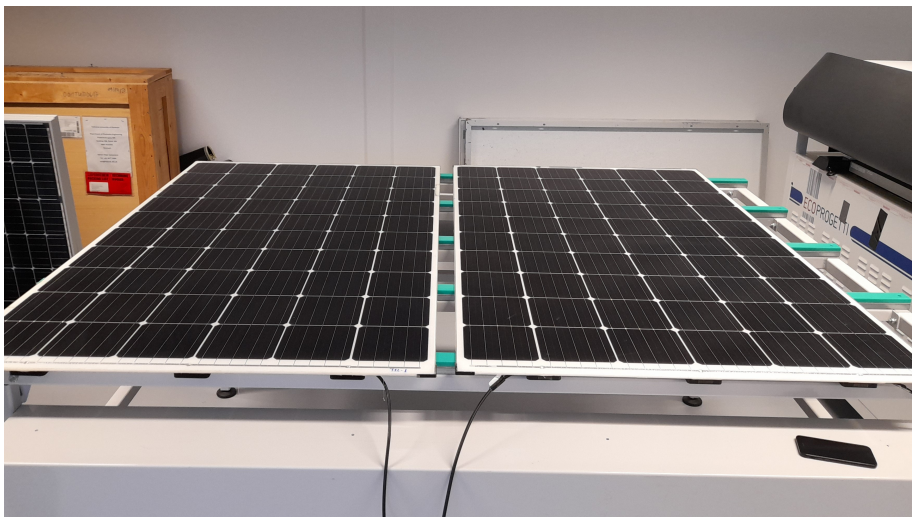

Figure 5.8: Visual inspection of the bifacial module. Left: Fielded module. Right: Reference module

5.6.2 I-V measurement

Then, the I-V characteristics of the modules were measured in the flasher. I-V curves are essential to detect any degradation of the module performance and can also be used to identify any issues in the cells that may need to be addressed. The PV modules were connected to the flasher, which measured their electrical performance under different irradiance conditions. For each of the 20 modules tested, three flashes at 1000 W/m^2 (then averaged) and one test at 200 W/m^2 were taken. In the case of bifacial modules, the back side was flashed once at 1000 W/m^2 and once at 200 W/m^2. Figure 5.9 shows the inside and outside of the flasher used in DTU's facilities.

(a) Outside (b) Inside

Figure 5.9: Flasher in DTU's facilities

The main outputs from the flash tests that are analysed are P_{mp}, I_{sc}, I_{mp}, V_{oc}, V_{mp}, the slope near I_{sc} and the slope near V_{oc}. The annual degradation rate for both the front and back sides was obtained by calculating the difference (in %) between the measured panel and the reference and then averaged over the number of years in the field. Since the commissioning was in the summer of 2018, the number of years of the modules in System B is 4.5. The degradation of the series and shunt resistance is obtained as the inverse to the slope of V_{oc} and I_{sc} respectively.

5.6.3 Electroluminescence testing

After the flash tests, an electroluminescence (EL) test was done on four different modules (two monofacial and two bifacial, one of which was the reference one). EL testing is a method used by solar panel installers and maintenance technicians to assess the quality and performance of PV cells. During an EL test, the solar module is forward-biased at I_{sc}, and the resulting emission of light is used to identify any defects or damage in the cells such as cracks, possible hot spots, and areas of high resistance.

Figure 5.10 shows the picture from the EL test for the two monofacial panels, which were chosen because they had the lowest P_{mp} out of the sample tested. Moreover, Figures 5.11 and 5.12 show the front and back sides of the reference and fielded bifacial module. In the case of the used module (fig. 5.12), it is appreciated that some of the cells in the upper centre part are darker than others. This can indicate a variety of defects, including that these cells have poor electrical connections or that they have been damaged by sunlight or other environmental factors.

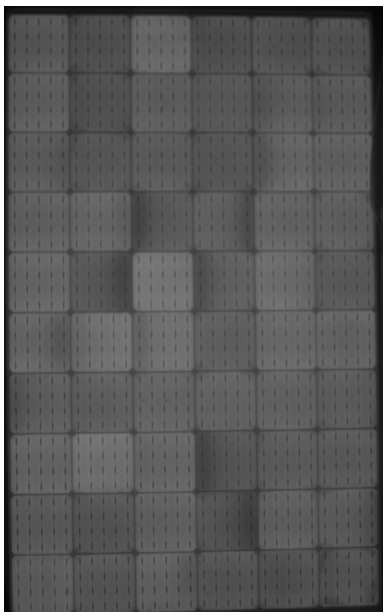

(a) Monofacial module 1 in string 7.5

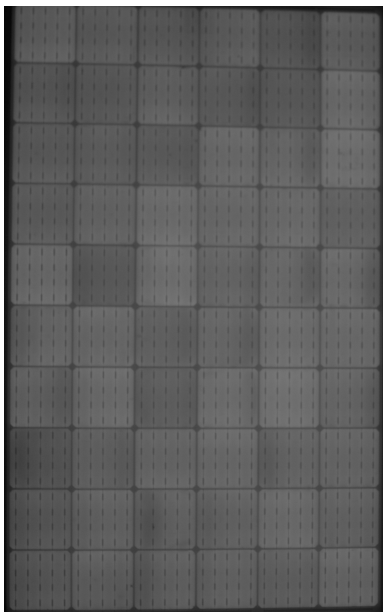

(b) Monofacial module 2 in string 7.5

Figure 5.10: EL testing of monofacial panels. They had the highest power degradation rate out of the sample tested.

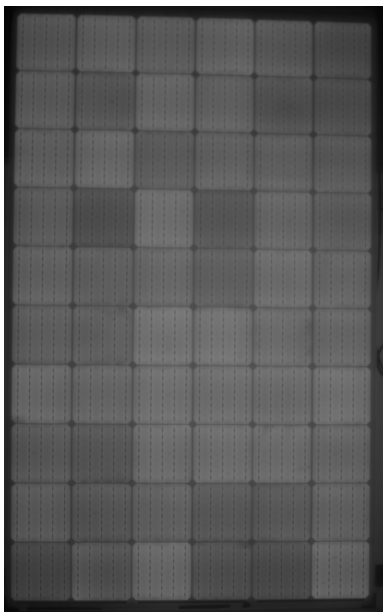

(a) Front side

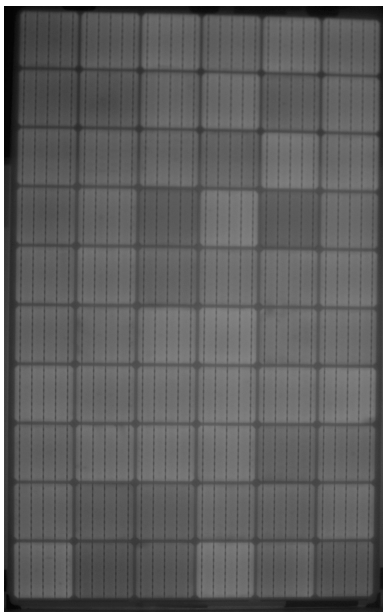

(b) Back side

Figure 5.11: EL testing bifacial reference panel. It has never been fielded.

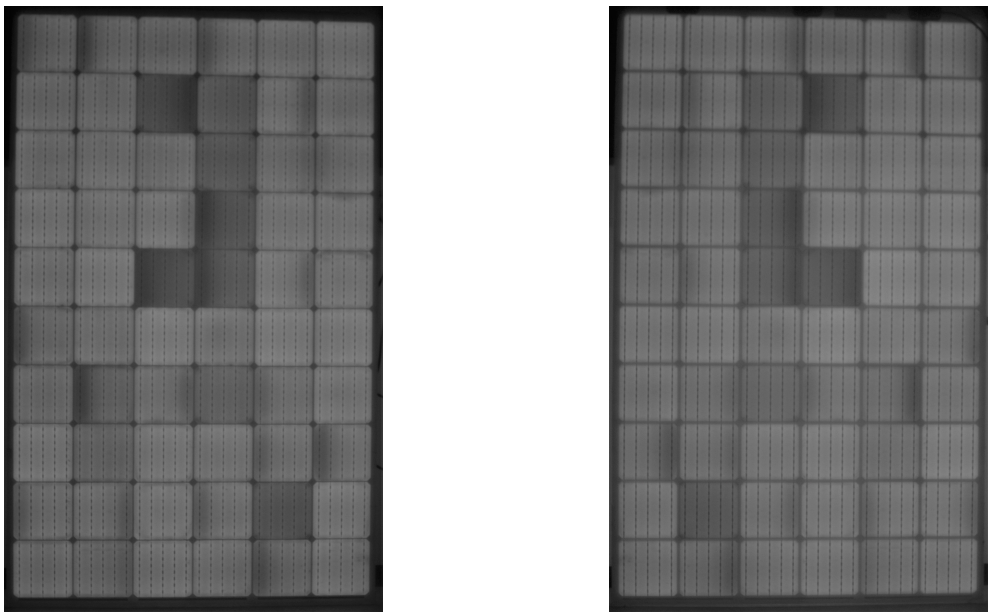

(a) Front side (b) Back side

Figure 5.12: EL testing bifacial fielded panel during 4.5 years. This module had the highest power degradation rate out of the sample tested.

6 Results and discussion

This final chapter presents the results of the degradation rate analysis performed on both systems, which are then discussed and compared with other studies in the field described in section 2.2. Finally, laboratory test results will aid in identifying the main degradation modes in System B's modules.

6.1 System A

In System A, two different approaches were used to obtain the degradation rate, an 8-years daily analysis and a 4-years detailed analysis. Figures 6.1 and 6.2 represent an example of the results. In this case there is little difference in the estimated degradation rate, but this is not the case for all the inverters in the park (discussed below). The model draws a trend line to each day of the year (i.e., to each January 1st, 2nd, etc.) and the median of these trend lines represents the estimated degradation rate. On the left side of the results' figure, a daily renormalized energy with the fitted degradation trend is shown. The normalized energy is renormalized by recentering the data so that the y-intercept of the linear degradation rate equals one at the beginning of the time series. On the right side, there is a histogram of the estimated YoY rates for each day of the year based on the renormalized energy, which includes the estimated degradation rate value (R_d) and the 68.2% confidence interval range. This histogram contains the estimated degradation rate for each day of the year (365/366 points).

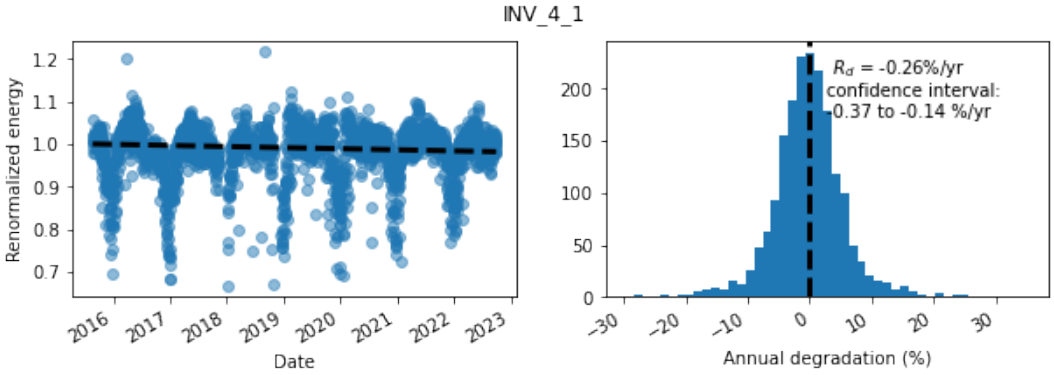

Figure 6.1: Degradation rate for Inverter 4.1 in System A in daily analysis

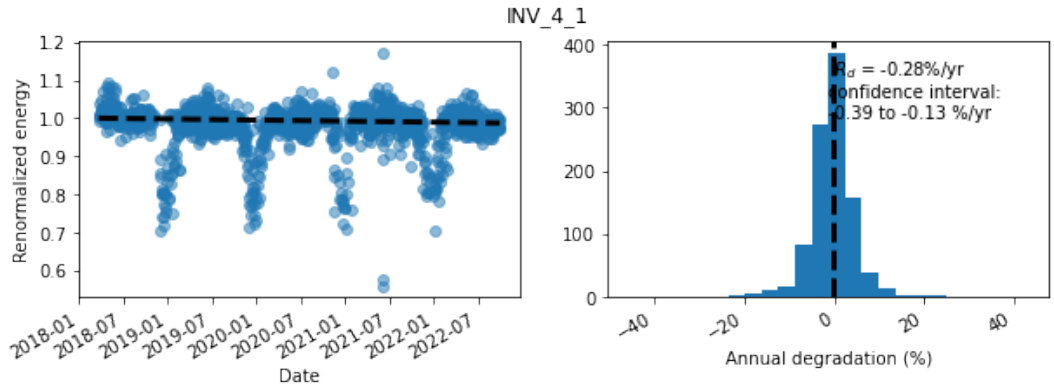

Figure 6.2: Degradation rate for Inverter 4.1 in System A in detailed analysis

Moreover, figs. 6.1 and 6.2 show the difference between the daily and detailed analyses. In this specific inverter, the annual degradation rate is very similar in both analyses (-0.26 %/year and -0.28 %/year). The more evident difference is that the daily analysis has a longer time series, thus more data points. This usually improves the accuracy of the calculation and decreases the associated confidence intervals [42]. However, the absence of intraday filtering increases the spread of the points over the renormalized energy, which makes the confidence intervals in both analyses very similar.

Also, a persisting seasonal component can be observed for both analyses. Although a low irradiation threshold and IAM correction factor have been applied in the detailed analysis, the lower peaks in the renormalized energy seen during the winter months are characteristic of PV plants in northern latitudes. This is mainly linked to the shadowing between rows in the winter due to the fact that the sun's elevation is lesser during the day. This system is designed to maximize the annual energy yield, so the summer period with higher irradiance is prioritized when deciding the tilt angle and the distance between rows, whereas the winter production is sacrificed as it represents a low percentage of the yearly energy output. Nevertheless, this marked seasonality doesn't influence the calculation of the degradation rate because it creates a trend line for each day of the year and the renormalized energy on a given day of the year is assumed to be similar over multiple years. This remarks the benefit of using the YoY method.

The degradation analysis was run for all the inverters in System A. A box plot of System A's results is shown in fig. 6.3, while the individual results for each inverter are in Appendix A. The median degradation of System A's inverters using a daily analysis is -0.41 %/year, with a maximum of -0.65 %/year and a minimum of -0.05 %/year. With the detailed analysis, the median degradation rate is -0.51 %/year, with a maximum of -0.95 %/year and a minimum of -0.10 %/year. Indeed, the median degradation rates obtained with both methods are within the manufacturer warranty limits.

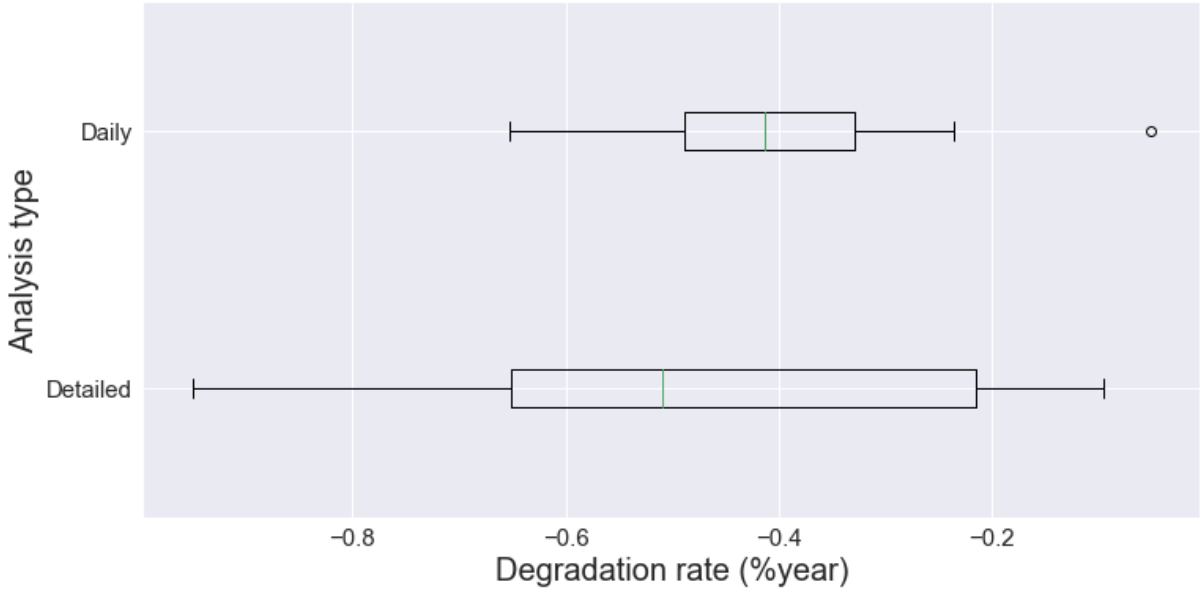

Figure 6.3: Degradation rates of the 11 inverters in System A. Daily is an 8-year analysis and Detailed a 4-year analysis

The fact that both approaches lead to a similar median, which is in the range of other degradation rate studies (section 2.2), indicates that both analyses are valid and comparable when

calculating the degradation rate of a fleet of modules and inverters. However, when analysing a single PV system, bigger differences are seen between methods. Figure 6.4 shows the absolute difference in the degradation rate between the daily and the detailed analysis for each inverter. A clear pattern in the behaviour of both approaches is not observed. As has been stated previously, the real degradation of each inverter is unknown, so the best solution is to consider the median of a fleet that has been operating under the same conditions. Being unbiased in the median, this distribution is expected to be a good measure of System A's degradation rate as a whole and should be considered in its business case.

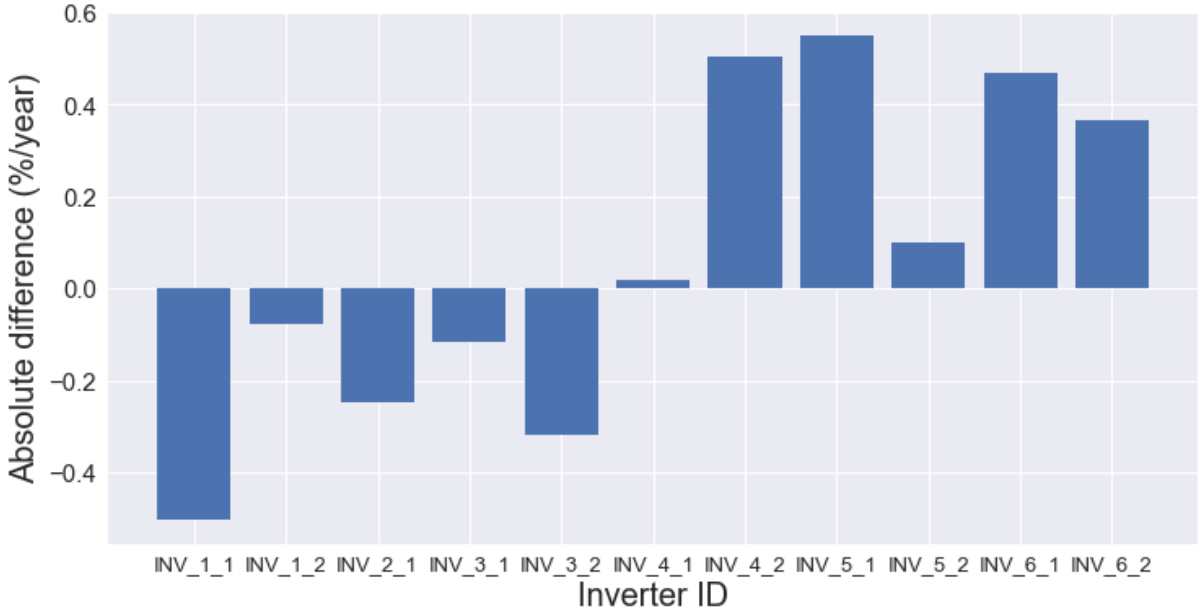

Figure 6.4: Difference in detailed and daily approaches for calculating the degradation rate of each inverter in System A

6.2 System B

6.2.1 Data analysis

On the other hand, the yearly degradation rate is obtained for 42 strings in System B, which can be divided into 4 groups according to their PV technology and mounting configuration (monofacial/bifacial and fixed-tilt/trackers). Figure 6.5 shows the distribution of the degradation rates of all the strings in System B. The median for System B is -0.65 %/year, with a maximum of -1.08 %/year and a minimum of +0.35 %/year (which means a gain in performance). Positive degradation rates have also been reported when analysing a large number of modules [39, 36]. This distribution is very similar to the results of single modules in [37] (fig. 2.6), but in this analysis only strings are studied.

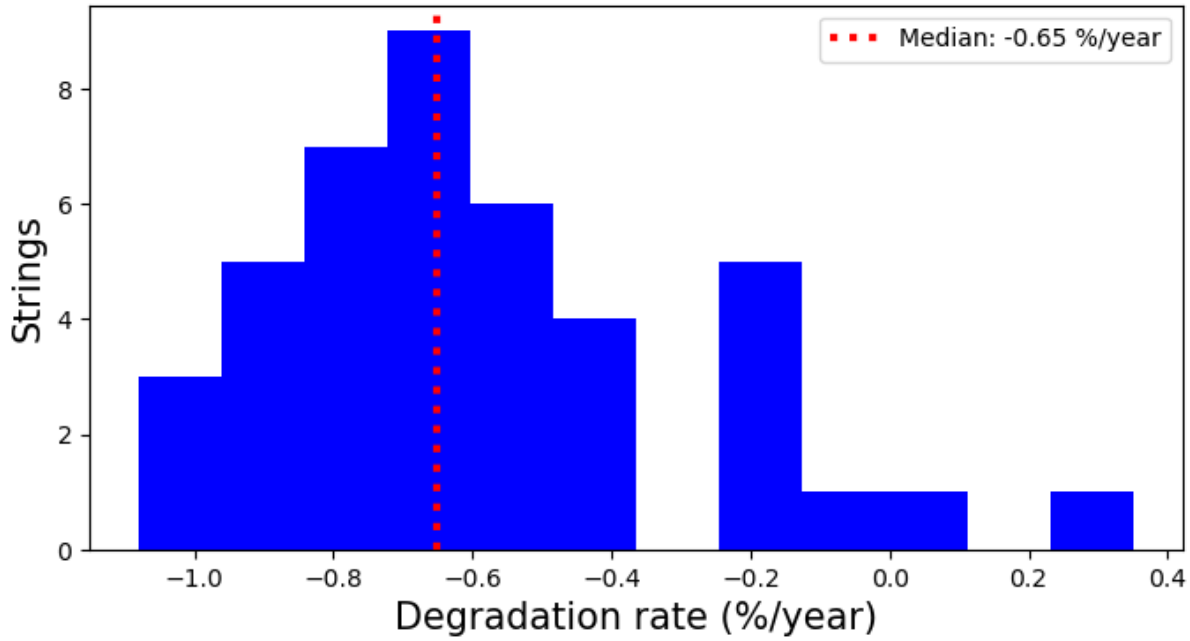

Figure 6.5: Histogram of degradation rates obtained for 42 strings in System B

Additionally, the degradation results for each system configuration are shown in fig. 6.6.

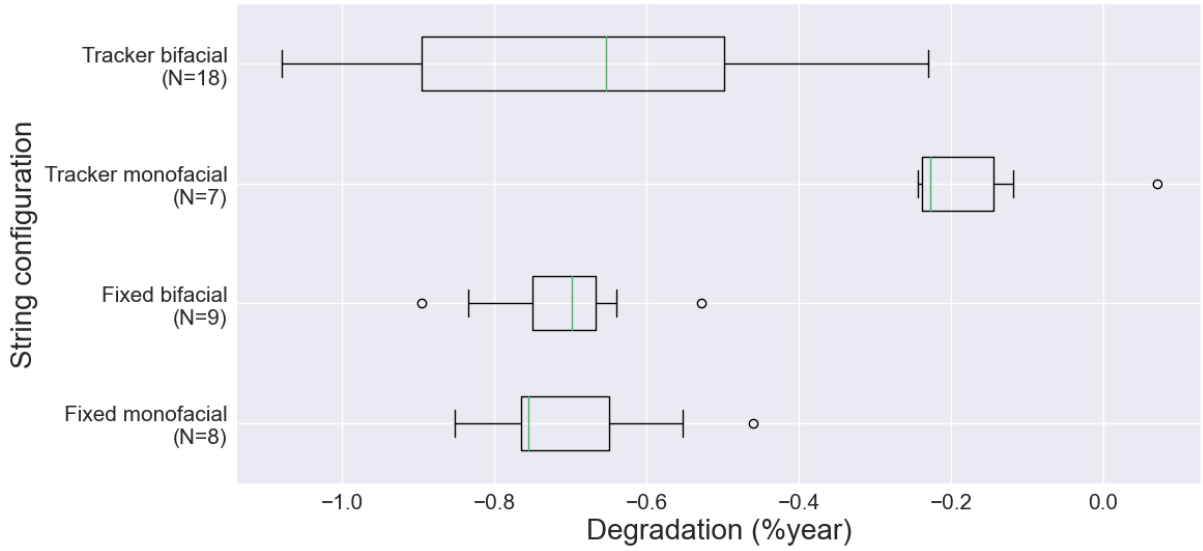

Figure 6.6: Distribution of degradation rates for each PV technology and mounting configuration in System B

Firstly, the tracked bifacial strings have the widest spread of results, which is linked to the fact that 18 strings out of 42 represent this configuration. The median for the tracker bifacial strings is -0.65 %/year. System B is one of the first PV plants with bifacial tracking modules, so no literature was found. This median is similar to the one obtained for the bifacial fixed strings (-0.69 %/year), which is lower than the reported ones in the literature regarding bifacial panels. The fact of being a relatively new technology and not being operational for a long time period makes bifacial module degradation still uncertain. In fact, the datasheet of these modules guarantees a

degradation of -0.5 %/year, which is optimistic considering the results obtained in this analysis.

As to monofacial modules, big differences are seen in comparing the tracker with the fixed-tilt configurations. In this case, the tracking monofacial strings showed the lowest degradation in the whole system, with a median of -0.22 %/year. A possible reason behind this is the position of these strings in System B's layout. As they are in the first 2 rows of the trackers' area, the shadows from the front row are considerably less. Still, only 7 strings have this configuration, so a wider sample would lead to more solid conclusions. Finally, the fixed-tilt monofacial modules have a median degradation rate of -0.75 %/year, which is matching within <0.1%/year with the literature [36].

Moreover, fig. 6.7 shows an example of how the effect of the shadowing between rows creates seasonality in the renormalized energy. String 7.7 (lower row) and String 7.8 (upper row) are two parallel strings located one on top of the other whose estimated degradation rates are -0.76 %/year and -0.75 %/year respectively. As it is seen, the trend for String 7.8 fits better with the renormalized energy, whereas the seasonality that String 7.7 exhibits makes fewer points fall on the linear trend line. This shows the big impact that shadows have on the module's energy output. In the case of tracking systems, backtracking allows to reduce this shadowing, so the effect is higher in fixed-tilt systems.

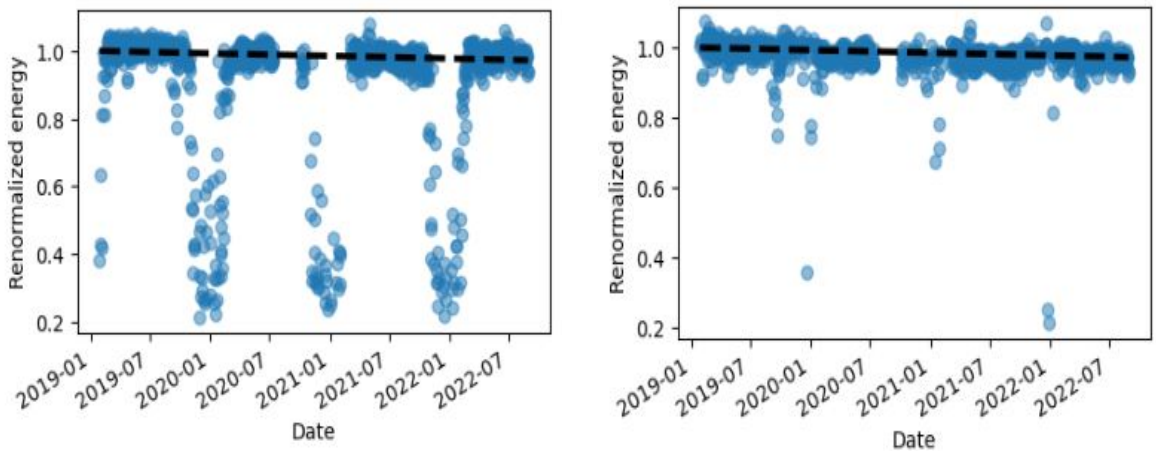

(a) String 7.7 - Lower row

(b) String 7.8 - Upper row

Figure 6.7: Renormalized energy time-series for 2 parallel strings

It is important to mention that, even though shadows are a stress factor for solar modules that can lead to higher degradation, the degradation rate calculation is not affected by the seasonality thanks to the use of the Year on Year methodology. This is the case of strings 7.7 and 7.8, which have a very close degradation rate despite having different energy time series. The individual results for each string can be checked in appendix A, but the same behaviour is seen in the strings that are in the lower row (odd numbers).

6.2.2 Flash tests

Figure 6.8 shows the degradation in power obtained from the flash tests in STC conditions. In this figure, the median of the analysis with the YoY method is also represented to ease the comparison with the previous results. As mentioned in section 2.3, the results from the flash tests are subject to two main uncertainties: The reference considered for comparison and the +5W power tolerance within modules from the same batch.

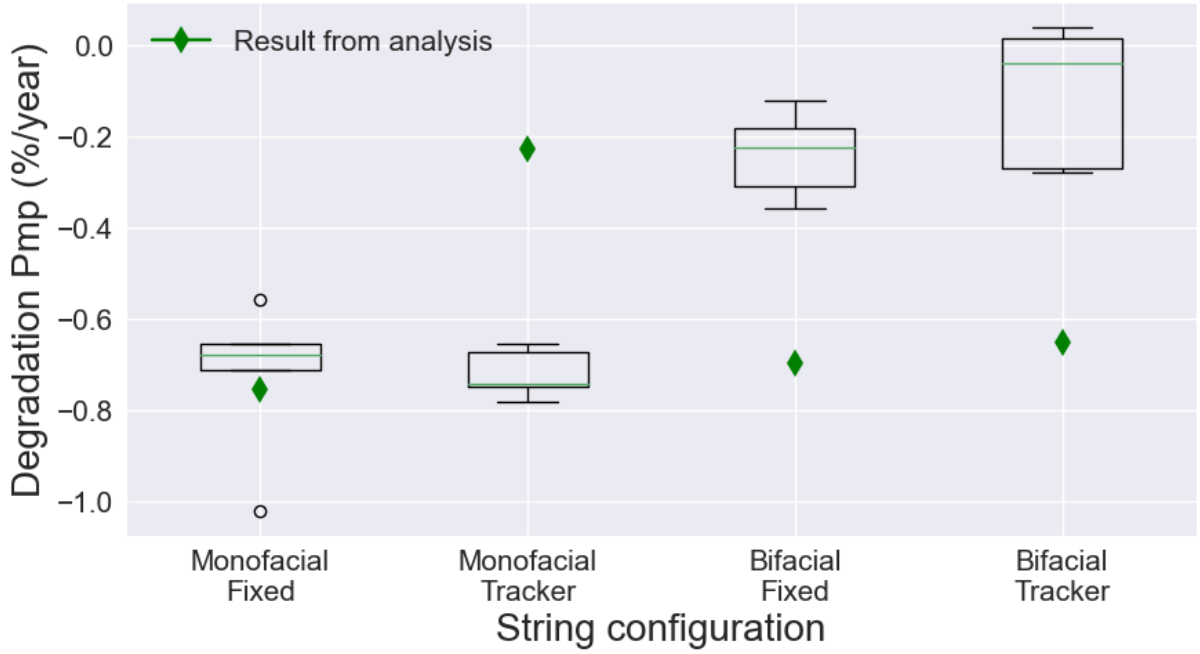

Figure 6.8: Degradation according to flash tests for each system configuration. The green diamonds represent the results with the YoY method

In this sense, a mismatch is seen between the results obtained from the flash tests and the data analysis in all the cases except for the monofacial fixed systems. It is important to recall that the monofacial modules are compared to their nameplate capacity (305W), whereas the bifacial modules are compared to a reference module that has never been in the field and whose measurement was close to its nameplate rating (295 W). In this sense, the forthcoming analysis is conducted assuming the reliability of the bifacial reference module. Table 6.1 illustrates the results of the rest of the parameters analysed for every string configuration:

Table 6.1: Degradation (%/year) of each parameter according to flash tests

	Monofacial Fixed	Monofacial Tracker	Bifacial Fixed	Bifacial Tracker
P_{mp}	-0.68	-0.74	-0.23	-0.04
I_{mp}	-0.39	-0.40	-0.33	-0.27
I_{sc}	-0.49	-0.43	-0.51	-0.49
V_{mp}	-0.32	-0.38	+0.12	+0.19
V_{oc}	-0.34	-0.27	-0.06	-0.01
R_s	NA	NA	+0.56	+0.66
R_{sh}	NA	NA	-8.49	-10.06

Monofacial modules

In the case of monofacial modules, similar behaviour is observed for fixed-tilt and tracking systems. It is found that the short-circuit current (I_{sc}) and, to a lesser extent, the maximum power current (I_{mp}) are the largest contributors to power degradation. During the visual inspection, partial loss of the AR coating was observed in the monofacial modules, which typically reduces the I_{sc} and V_{oc}. As expected, these symptoms are observed in the results. The series and shunt resistances could not be evaluated because they don't appear in the datasheet. Finally, there

is an overall degradation in all the parameters studied in the monofacial panels, which may also be linked to PID (characteristic of northern latitudes with moist weather). However, no strong evidence of PID was observed in the EL images.

Bifacial modules

Regarding the bifacial modules, fixed-tilt systems appear to have slightly more degradation than tracking ones, which is also seen in fig. 6.6. In both cases, the maximum power reduction is dominated by an I_{sc} decline of around -0.50 %/year. The reduction in I_{sc} points to optical losses on the front side such as discoloration due to the humidity. The V_{mp} and the V_{oc} display relative stability, with even a slight increase in the V_{mp} which can be linked to the unsuitability of the reference module or to temperature variations of the flash room at the time of measurement. Moreover, there is a small increase in the series resistance, which is inevitable for modules deployed outdoors due to thermal cycling. Also, series resistance increase can be attributed to mechanical fatigue of solder joints in the case of the tracking systems. Finally, the big degradation of the shunt resistance (linked to the slope of the I_{sc}) can be associated with manufacturing defects or impurities near the junction due to poor module cleaning and maintenance.

7 Conclusions

In conclusion, this thesis has investigated the degradation rates of two PV plants located in Northern Latitudes based on the DC power and long-term monitoring data. On the one hand, two different approaches were followed in System A: daily and intraday analyses. The median of the estimated degradation rates was similar for both approaches (-0.41 %/year and -0.51 %/year respectively), so it is suggested that both methods provide reliable results as far as a fleet of components (11 inverters in this case) is tested and the median is considered. On the other hand, System B has strings with different technologies and designs. After modelling some of the main parameters, it was found a median degradation rate of -0.65 %/year, but with different distributions according to the string configuration. Then, indoor characterization including visual inspection, I-V measurement under STC conditions and electroluminescence imaging was performed to verify these findings and analyse the degradation mechanisms. Some mismatches were found with respect to the initial analysis that can be linked to the lack of a reliable base to compare the results of the flash tests. Finally, although fielded modules often display a variety of degradation modes, it was possible to correlate the gradual performance loss to some of the main degradation modes described.

During the development of the analysis, it has been evidenced the importance of storing high-resolution data of the main parameters that define the performance of a PV system (mainly power produced, POA irradiance and module temperature). Especially, when the data is intended to be used in a degradation rate analysis, it is crucial that the irradiance sensors are calibrated regularly to lower the uncertainty and reduce data shifts in the calculation. Also, in a PV plant with different string configurations, each one should have its own measuring sensors to avoid the modelling of crucial variables in the calculation. In System B this was not the case, so the assumptions taken during the modelling can also influence the results. For instance, in the correction of angular losses, instead of a separation between clear and cloudy time steps, the diffuse fraction of the irradiance could be used to calculate a correction for every individual time step.

Moreover, different methodologies can lead to variable results even when using the same data set, so the estimated annual performance loss mainly depends on the analysis methodology and filtering techniques used for its assessment. In this study, the Year on Year methodology and conservative filters based on previous studies have been applied. However, it is imperative the need of a common and unambiguous approach that can be applied to large data sets, reducing the variability and increasing confidence in the results.

Ultimately, I-V testing appears to be the most solid method to approximate the real degradation rate of a specific set of modules. Therefore, it is highlighted the importance of flash testing before they are installed and then using this as a basis for comparison in the future. Despite the lack of initial flash tests, it has been observed that the degradation in northern latitudes may be driven by optical losses linked to moisture, causing a reduction in the short-circuit current. Besides, a more detailed analysis should be performed to accurately determine the most significant degradation modes in these latitudes.

In light of the above, this study contributes to a closer understanding of the causes and calculation methodology of the degradation rate in PV plants. Further research on this topic is desired, as it provides insight into their long-term performance and reliability, which have a significant impact on the overall technical and financial evaluation of a project.

Further work

This study serves as a first evaluation of the degradation rates on both systems. As the systems are still operational, it is recommended to keep increasing the data collection and repeat the process in the future to draw stronger conclusions and gain better insight into the long-term degradation rate for new plants in close locations. In the same way, now that some modules have been flash tested, repeating the tests under the same conditions in the future would give very useful information about their real performance loss.

Additionally, uncertainty plays an important role when reporting values for degradation because high measurement uncertainties increase the statistical spread of the data. Another opportunity for improvement is to place more emphasis on comprehensive uncertainty analysis, as uncertainty is directly correlated to financial risk.

Moreover, the implicit assumption in the analysis above is the linearity of the long-term degradation curve. However, depending on the degradation modes, PV degradation may not be linear over the life of the system, especially at the beginning of life or during the wear-out phase. Outdoor data usually contain considerable noise making it difficult to discern subtle deviations from linearity, and that is why non-linearities are typically more easily observed in accelerated tests where changes are easier to detect. Despite this, it is suggested a partition of continuous data into shorter time intervals, which allows the determination of several degradation rates which could provide more information than one overall degradation rate. It is imperative that quantifying the non-linearity in degradation curves can have a significant impact on the financial aspects of a PV project so, in the future, measuring and including linear degradation rates in models may not be sufficiently accurate.

Finally, although it is evident that proper maintenance can help reduce the degradation rate of a PV plant, this study suggests further research on the causes of degradation in cold and humid climates in order to develop effective strategies for mitigating it.

Bibliography

[1] bp. *Statistical Review of World Energy*. 2022. URL: https://www.bp.com/en/global/corporate/energy-economics/statistical-review-of-world-energy.html.

[2] Dirk Jordan et al. “PV degradation curves: Non-linearities and failure modes”. In: *Progress in Photovoltaics: Research and Applications* 25 (Sept. 2016). DOI: 10.1002/pip.2835.

[3] C. Osterwald and T. McMahon. “History of Accelerated and Qualification Testing of Terrestrial Photovoltaic Modules: A Literature Review”. In: *Progress in Photovoltaics: Research and Applications* 17 (Jan. 2009), pp. 11–33. DOI: 10.1002/pip.861.

[4] William Holmgren, Clifford Hansen, and Mark Mikofski. “pvlib python: a python package for modeling solar energy systems”. In: *Journal of Open Source Software* 3 (Sept. 2018), p. 884. DOI: 10.21105/joss.00884.

[5] Michael G. Deceglie et al. *RdTools*. Version 2.2.0. DOI: 10.5281/zenodo.7411201. URL: https://github.com/NREL/rdtools.

[6] Dirk Jordan et al. “Robust PV Degradation Methodology and Application”. In: *IEEE Journal of Photovoltaics* PP (Dec. 2017), pp. 1–7. DOI: 10.1109/JPHOTOV.2017.2779779.

[7] Giorgio Belluardo et al. “Novel method for the improvement in the evaluation of outdoor performance loss rate in different PV technologies and comparison with two other methods”. In: *Solar Energy* 117 (July 2015). DOI: 10.1016/j.solener.2015.04.030.

[8] M.A. Quintana et al. “Commonly observed degradation in field-aged photovoltaic modules”. In: *Conference Record of the Twenty-Ninth IEEE Photovoltaic Specialists Conference, 2002.* 2002, pp. 1436–1439. DOI: 10.1109/PVSC.2002.1190879.

[9] Sascha Lindig et al. “International collaboration framework for the calculation of performance loss rates: Data quality, benchmarks, and trends (towards a uniform methodology)”. In: *Progress in Photovoltaics Research and Applications* 29 (Mar. 2021), pp. 573–602. DOI: 10.1002/pip.3397.

[10] Dirk C Jordan et al. “Photovoltaic failure and degradation modes”. In: *Progress in Photovoltaics: Research and Applications* 25.4 (2017), pp. 318–326.

[11] Jaeun Kim et al. “A review of the degradation of photovoltaic modules for life expectancy”. In: *Energies* 14.14 (2021), p. 4278.

[12] E.L. Meyer and E.E. van Dyk. “Assessing the reliability and degradation of photovoltaic module performance parameters”. In: *IEEE Transactions on Reliability* 53.1 (2004), pp. 83–92. DOI: 10.1109/TR.2004.824831.

[13] Jeffrey A. Mazer. “Solar Cells: An Introduction to Crystalline Photovoltaic Technology”. In: 1996, pp. 151–153.

[14] G. Oreski and G.M. Wallner. “Evaluation of the aging behavior of ethylene copolymer films for solar applications under accelerated weathering conditions”. In: *Solar Energy* 83.7 (2009), pp. 1040–1047. ISSN: 0038-092X. DOI: https://doi.org/10.1016/j.solener.2009.01.009. URL: https://www.sciencedirect.com/science/article/pii/S0038092X09000115.

[15] F. J. Pern and A. W. Czanderna. “EVA degradation mechanisms simulating those in PV modules”. In: *AIP Conference Proceedings* 268.1 (1992), pp. 445–452. DOI: 10.1063/1.42901. URL: https://aip.scitation.org/doi/abs/10.1063/1.42901.

[16] N.C. Park et al. “The effect of encapsulant discoloration and delamination on the electrical characteristics of photovoltaic module”. In: *Microelectronics Reliability* 53.9 (2013). European Symposium on Reliability of Electron Devices, Failure Physics and Analysis, pp. 1818–1822. ISSN: 0026-2714. DOI: https://doi.org/10.1016/j.microrel.2013.07.062. URL: https://www.sciencedirect.com/science/article/pii/S0026271413002370.

[17] S. R. Wenham, M. A. Green, and M. E. Watt. *Applied Photovotlaics*. Third Edition. Routledge, 2011.
[18] S. R. Rummel and T. J. McMahon. “Effect of cell shunt resistance on PV module performance at reduced light levels”. In: *AIP Conference Proceedings* 353.1 (1996), pp. 581–586. DOI: 10.1063/1.49388. URL: https://aip.scitation.org/doi/abs/10.1063/1.49388.
[19] S. Thorsteinsson, S. Spataru, and N.R. Lyngskær. *Lecture 3.3: I-V Curves and Equivalent Circuit Models*. University Lecture. 2021.
[20] S. M. Sze and Kwok K. Ng. *Physics of Semiconductor Devices*. Third Edition. John Wiley and Sons, 2006.
[21] W. Herrmann, W. Wiesner, and W. Vaassen. “Hot spot investigations on PV modules-new concepts for a test standard and consequences for module design with respect to bypass diodes”. In: *Conference Record of the Twenty Sixth IEEE Photovoltaic Specialists Conference - 1997*. 1997, pp. 1129–1132. DOI: 10.1109/PVSC.1997.654287.
[22] E. Rueland et al. “Optical μ-crack detection in combination with stability testing for in-line inspection of wafers and cells”. In: 2005.
[23] J Yang et al. “Recent progress in amorphous silicon alloy leading to 13% stable cell efficiency”. In: (Dec. 1997). ISSN: 0160-8371. URL: https://www.osti.gov/biblio/304322.
[24] Michelle Kitayama da Silva. “Photovoltaic Module Degradation”. In: *Encyclopedia* (2021). URL: https://encyclopedia.pub/entry/16779.
[25] Mauro Pravettoni. “Module Deployment and Energy Rating”. In: *Solar Cells and Modules*. Springer International Publishing, 2020, pp. 249–283. DOI: 10.1007/978-3-030-46487-5_10. URL: https://doi.org/10.1007/978-3-030-46487-5_10.
[26] Daqi Zhang et al. “Comparison of Letid in Monofacial and Bifacial Multicrystalline PERC cells and modules”. In: Sept. 2020.
[27] M. Schütze et al. “Laboratory study of potential induced degradation of silicon photovoltaic modules”. In: *2011 37th IEEE Photovoltaic Specialists Conference*. 2011, pp. 821–826. DOI: 10.1109/PVSC.2011.6186080.
[28] Pietro Tumino. *Causes and Solutions of the Potential Induced Degradation (PID) Effect in PV Modules*. 2020. URL: https://eepower.com/technical-articles/causes-and-solutions-of-the-potential-induced-degradation-effect-in-pv-modules/#.
[29] Matthias Schütze et al. “Investigations of potential induced degradation of silicon photovoltaic modules”. In: *26th EU PVSEC* (Jan. 2011), pp. 3097–3102.
[30] Peter Hacke et al. “System voltage potential-induced degradation mechanisms in PV modules and methods for test”. In: *2011 37th IEEE Photovoltaic Specialists Conference*. 2011, pp. 814–820. DOI: 10.1109/PVSC.2011.6186079.
[31] Jichao Li et al. “Electrochemical mechanisms of leakage-current-enhanced delamination and corrosion in Si photovoltaic modules”. In: *Solar Energy Materials and Solar Cells* 188 (2018), pp. 273–279. ISSN: 0927-0248. DOI: https://doi.org/10.1016/j.solmat.2018.09.010. URL: https://www.sciencedirect.com/science/article/pii/S0927024818304525.
[32] A. Omazic et al. “Relation between degradation of polymeric components in crystalline silicon PV module and climatic conditions: A literature review”. In: *Solar Energy Materials and Solar Cells* 192 (2019), pp. 123–133. ISSN: 0927-0248. DOI: https://doi.org/10.1016/j.solmat.2018.12.027. URL: https://www.sciencedirect.com/science/article/pii/S0927024818305956.
[33] IEA Pvps. “Task 13: Review of Failures of PV Modules”. In: (Mar. 2014).
[34] Ernest Hasselbrink et al. “Validation of the PVLife model using 3 million module-years of live site data”. In: June 2013, pp. 7–12. ISBN: 978-1-4799-3299-3. DOI: 10.1109/PVSC.2013.6744087.

[35] Nils H. Reich et al. “System performance analysis and estimation of degradation rates based on 500 years of monitoring data”. In: *2012 38th IEEE Photovoltaic Specialists Conference*. 2012, pp. 001551–001555. DOI: 10.1109/PVSC.2012.6317890.

[36] Sascha Lindig et al. “Performance Analysis and Degradation of a Large Fleet of PV Systems”. In: *IEEE Journal of Photovoltaics* 11 (July 2021), pp. 1312–1318. DOI: 10.1109/JPHOTOV.2021.3093049.

[37] D Jordan, J Wohlgemuth, and Sarah Kurtz. “Technology and Climate Trends in PV Module Degradation”. In: Jan. 2012, pp. 3118–3124. DOI: 10.4229/27thEUPVSEC2012-4DO.5.1.

[38] Jeroen Larrivee. *An analysis of degradation rates of PV power plants at the system level*. 2013.

[39] Dirk Jordan et al. “Compendium of photovoltaic degradation rates”. In: *Progress in Photovoltaics: Research and Applications* 24 (Feb. 2016), n/a–n/a. DOI: 10.1002/pip.2744.

[40] Kristopher Davis et al. “Multi-Pronged Analysis of Degradation Rates of Photovoltaic Modules and Arrays Deployed in Florida”. In: *Progress in Photovoltaics Research and Applications* 21 (Feb. 2012). DOI: 10.1002/pip.2154.

[41] Dirk Jordan et al. “Photovoltaic fleet degradation insights”. In: *Progress in Photovoltaics: Research and Applications* 30 (Apr. 2022). DOI: 10.1002/pip.3566.

[42] Scott Adler et al. “Degradation Analysis of Utility-Scale PV Plants in Different Climate Zones”. In: *IEEE Journal of Photovoltaics* PP (Dec. 2020), pp. 1–6. DOI: 10.1109/JPHOTOV.2020.3043120.

[43] Marios Theristis et al. “Nonlinear Photovoltaic Degradation Rates: Modeling and Comparison Against Conventional Methods”. In: *IEEE Journal of Photovoltaics* 10 (May 2020), pp. 1112–1118. DOI: 10.1109/JPHOTOV.2020.2992432.

[44] Omar Albadwawi et al. “Investigation of Bifacial PV modules degradation under desert climatic conditions”. In: *2020 47th IEEE Photovoltaic Specialists Conference (PVSC)*. 2020, pp. 1505–1509. DOI: 10.1109/PVSC45281.2020.9300439.

[45] Dirk C. Jordan et al. “PV Degradation – Mounting & Temperature”. In: *2019 IEEE 46th Photovoltaic Specialists Conference (PVSC)*. 2019, pp. 0673–0679. DOI: 10.1109/PVSC40753.2019.8980767.

[46] Klaus Kiefer et al. “A Degradation Analysis of PV Power Plants”. In: Sept. 2010, pp. 5032–5037. DOI: 10.4229/25thEUPVSEC2010-5BV.4.26.

[47] IEA Pvps. “Task 13 Performance, Operation and Reliability of Photovoltaic Systems. Soiling Losses – Impact on the Performance of Photovoltaic Power Plants”. In: (Dec. 2022).

[48] George Makrides et al. “Energy yield prediction errors and uncertainties of different photovoltaic models”. In: *Progress in photovoltaics: research and applications* 21.4 (2013), pp. 500–516.

[49] *ISO 9060:2018, Solar energy — Specification and classification of instruments for measuring hemispherical solar and direct solar radiation*. International Organization for Standardization (ISO), 2018. URL: https://www.iso.org/obp/ui/#iso:std:iso:9060:ed-2:v1:en.

[50] *What are the different classes of pyranometers?* Accessed: October 2022. URL: https://trackso.in/knowledge-base/what-are-the-different-classes-of-pyranometers/.

[51] Sandia National Laboratories. *Sandia Module Temperature Model*. Accessed Ocotber 2022. URL: https://pvpmc.sandia.gov/modeling-steps/2-dc-module-iv/module-temperature/sandia-module-temperature-model/.

[52] Dirk Jordan and Sarah Kurtz. “The Dark Horse of Evaluating Long-Term Field Performance — Data Filtering”. In: *Photovoltaics, IEEE Journal of* 4 (Jan. 2014), pp. 317–323. DOI: 10.1109/JPHOTOV.2013.2282741.

[53] European Union. *PVGIS Photovoltaic Geographical Information System*. Accessed October 2022. 2020. URL: https://joint-research-centre.ec.europa.eu/pvgis-photovoltaic-geographical-information-system_en.

[54] European Union. *PVGIS data sources & calculation methods*. Accessed October 2022. 2020. URL: https://joint-research-centre.ec.europa.eu/pvgis-photovoltaic-geographical-information-system/getting-started-pvgis/pvgis-data-sources-calculation-methods_en.

[55] Ana Gracia Amillo, Thomas Huld, and Richard Müller. "A New Database of Global and Direct Solar Radiation Using the Eastern Meteosat Satellite, Models and Validation". In: *Remote Sensing* 6.9 (2014), pp. 8165–8189. URL: https://www.mdpi.com/2072-4292/6/9/8165.

[56] M. Castelli et al. "The HelioMont method for assessing solar irradiance over complex terrain: Validation and improvements". In: *Remote Sensing of Environment* 152 (2014), pp. 603–613. ISSN: 0034-4257. DOI: https://doi.org/10.1016/j.rse.2014.07.018. URL: https://www.sciencedirect.com/science/article/pii/S0034425714002673.

[57] PVSyst. *Sandia Model for PV modules*. Accessed Ocotber 2022. URL: https://www.pvsyst.com/help/index.html?sandia_model.htm.

[58] Ibrahim Reda and Afshin Andreas. "Solar position algorithm for solar radiation application". In: *Solar Energy* 76 (May 2004), pp. 577–589. DOI: 10.1016/j.solener.2003.12.003.

[59] Ibrahim Reda and Afshin Andreas. "Solar position algorithm for solar radiation applications". In: *Solar Energy* 76.5 (2004), pp. 577–589. DOI: https://doi.org/10.1016/j.solener.2003.12.003. URL: https://www.sciencedirect.com/science/article/pii/S0038092X0300450X.

[60] Eduardo Pigueiras, L. Narvarte, and J. Munoz. "Tracking and back-tracking". In: *Progress in Photovoltaics: Research and Applications* 19 (Sept. 2011), pp. 747–753. DOI: 10.1002/pip.1085.

[61] Mark A. Mikofski et al. "Bifacial Performance Modeling in Large Arrays". In: *2019 IEEE 46th Photovoltaic Specialists Conference (PVSC)*. 2019, pp. 1282–1287. DOI: 10.1109/PVSC40753.2019.8980572.

[62] Hugo Sánchez et al. "The effect of clearance height, albedo, tilt and azimuth angle in bifacial PV energy estimation using different existing algorithms". In: Nov. 2020.

[63] Bill Marion et al. "A Practical Irradiance Model for Bifacial PV Modules". In: *2017 IEEE 44th Photovoltaic Specialist Conference (PVSC)*. 2017, pp. 1537–1542. DOI: 10.1109/PVSC.2017.8366263.

[64] M. Lamers et al. "Temperature effects of bifacial modules: Hotter or cooler?" In: *Solar Energy Materials and Solar Cells* 185 (May 2018), pp. 192–197. DOI: 10.1016/j.solmat.2018.05.033.

[65] Dirk Jordan et al. "Reducing Interanalyst Variability in Photovoltaic Degradation Rate Assessments". In: *IEEE Journal of Photovoltaics* PP (Oct. 2019), pp. 1–7. DOI: 10.1109/JPHOTOV.2019.2945191.

[66] Dirk Jordan, Michael Deceglie, and Sarah Kurtz. "PV degradation methodology comparison — a basis for a standard". In: June 2017, pp. 1–6. DOI: 10.1109/PVSC.2017.8366644.

[67] Sandia National Laboratories. *Sandia Cell Temperature Model*. Accessed Ocotber 2022. URL: https://pvpmc.sandia.gov/modeling-steps/2-dc-module-iv/cell-temperature/sandia-cell-temperature-model/.

[68] Marion. "Influence of Atmospheric Variations on Photovoltaic Performance and Modeling Their Effects for Days with Clear Skies: Preprint". In: *Conference Record of the IEEE Photovoltaic Specialists Conference* (June 2012). DOI: 10.1109/PVSC.2012.6318300.

[69] Kent Whitfield and C. Osterwald. "Procedure for determining the uncertainty of PV module outdoor performance". In: *Progress in Photovoltaics: Research and Applications* 9 (Mar. 2001), pp. 87–102. DOI: 10.1002/pip.356.

[70] N. Martin and J.M. Ruiz. "Calculation of the PV modules angular losses under field conditions by means of an analytical model". In: *Solar Energy Materials and Solar Cells* 70.1 (2001), pp. 25–38. ISSN: 0927-0248. DOI: https://doi.org/10.1016/S0927-0248(00)00408-6. URL: https://www.sciencedirect.com/science/article/pii/S0927024800004086.

[71] Mariella Rivera Aguilar and Christian Reise. “Silicon Sensors vs. Pyranometers – Review of Deviations and Conversion of Measured Values”. In: Sept. 2020. DOI: 10.4229/EUPVSEC20202020-5BV.3.3.
[72] *Clear-sky index*. Accessed: January 2023. URL: https://ebrary.net/183058/environment/clear_index#aftercont.
[73] A. P. Dobos. “PVWatts Version 5 Manual”. In: (Sept. 2014). DOI: 10.2172/1158421. URL: https://www.osti.gov/biblio/1158421.

A APPENDIX

A.1 System A

A.1.1 Daily analysis

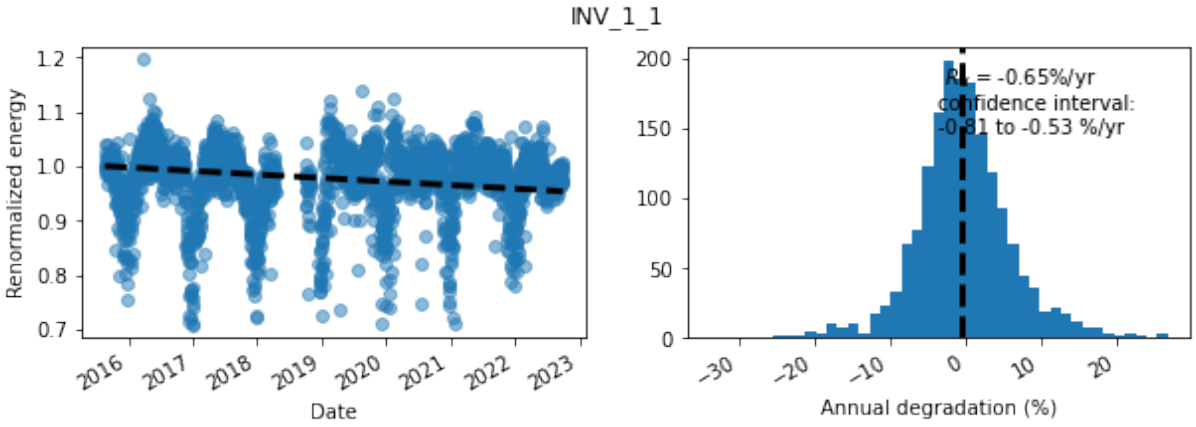

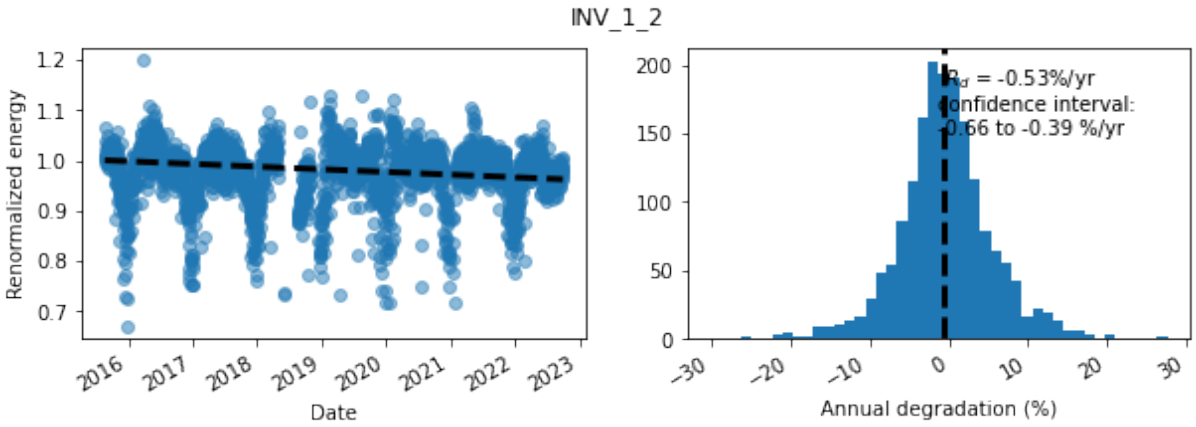

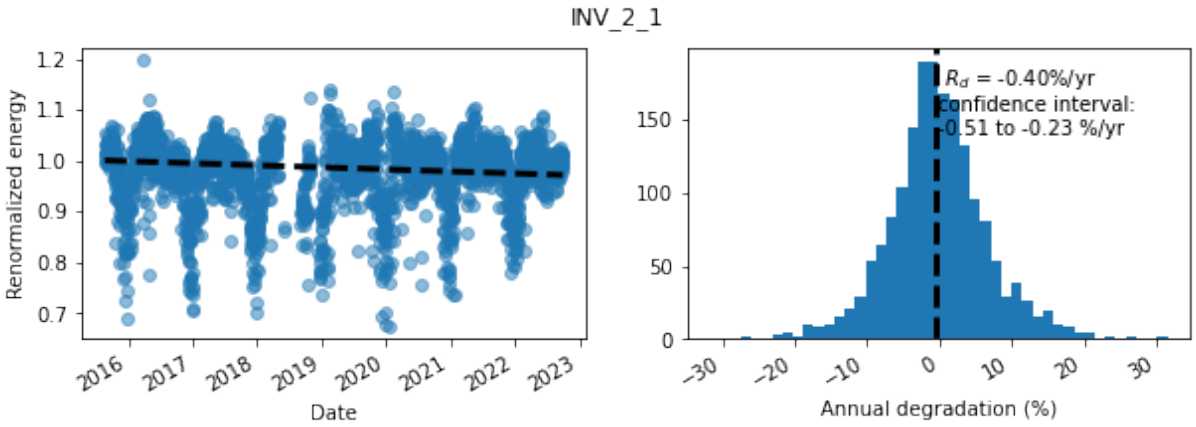

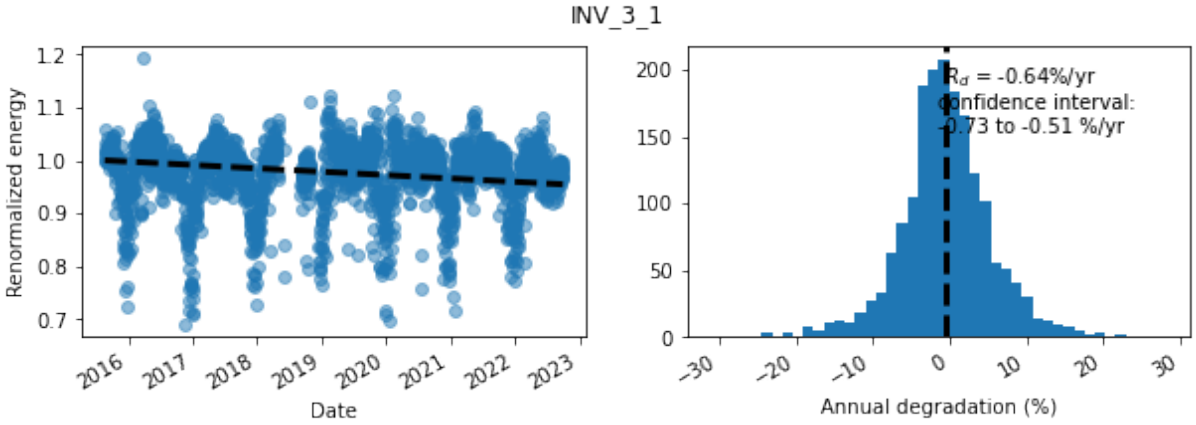
INV_3_1
Renormalized energy
Date
R_d = -0.64%/yr
confidence interval:
-0.73 to -0.51 %/yr
Annual degradation (%)

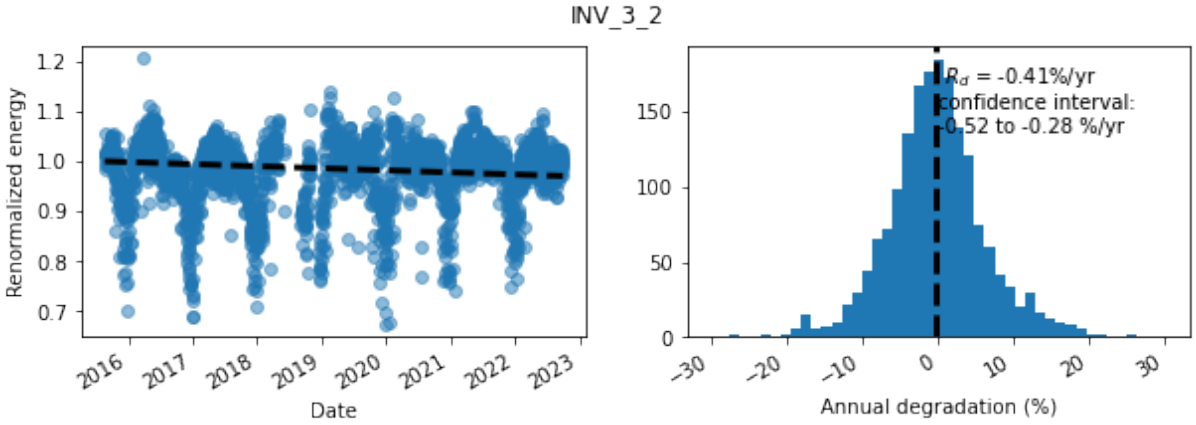
INV_3_2
Renormalized energy
Date
R_d = -0.41%/yr
confidence interval:
-0.52 to -0.28 %/yr
Annual degradation (%)

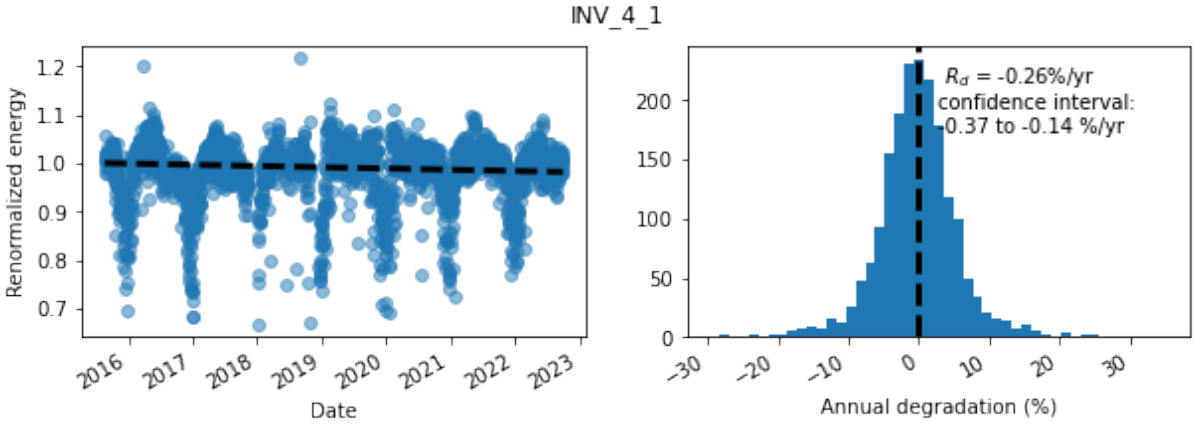
INV_4_1
Renormalized energy
Date
R_d = -0.26%/yr
confidence interval:
-0.37 to -0.14 %/yr
Annual degradation (%)

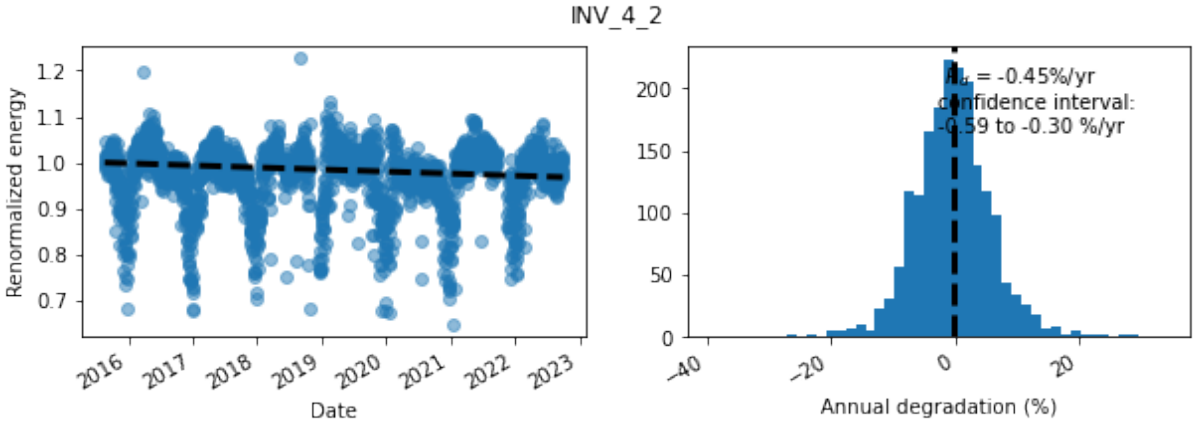
INV_4_2
Renormalized energy
Date
R_d = -0.45%/yr
confidence interval:
-0.59 to -0.30 %/yr
Annual degradation (%)

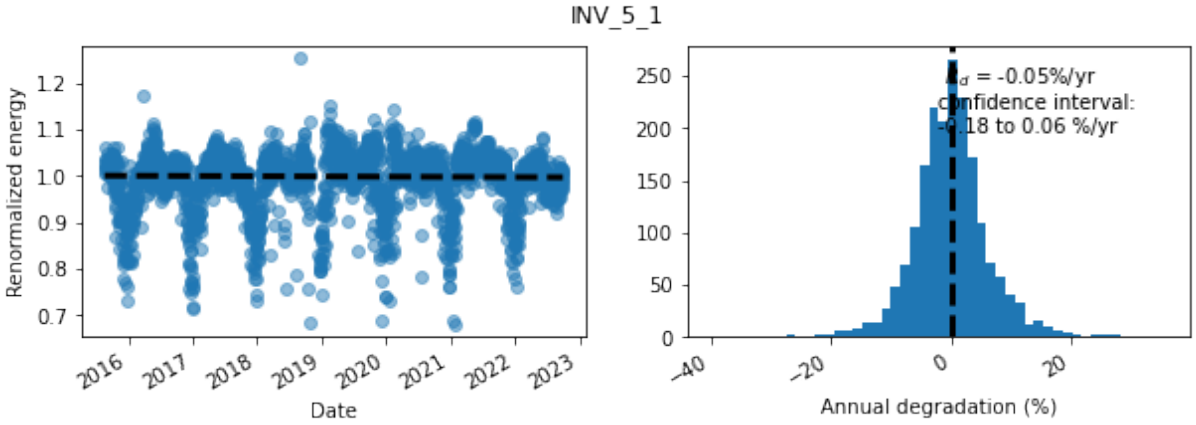
INV_5_1
Renormalized energy
Date
R_d = -0.05%/yr
confidence interval:
-0.18 to 0.06 %/yr
Annual degradation (%)

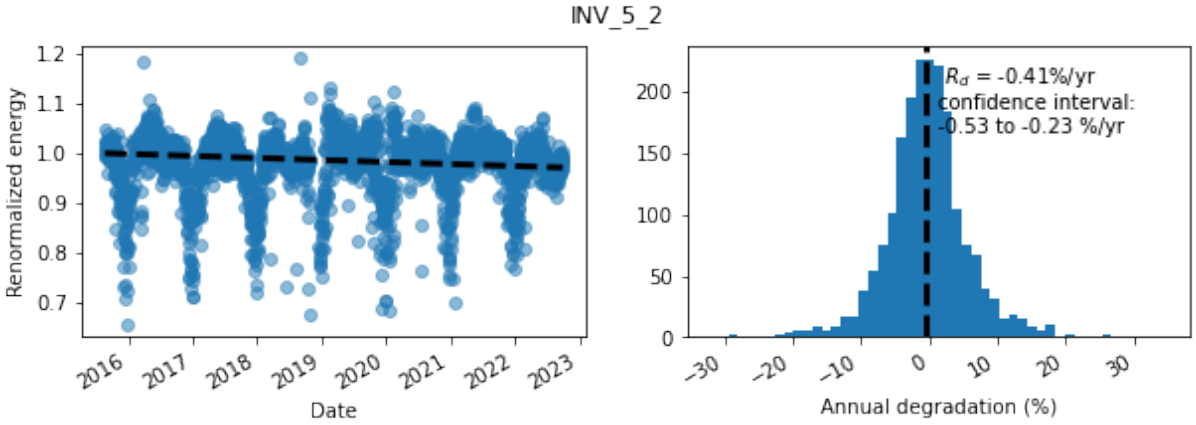
INV_5_2
Renormalized energy
Date
R_d = -0.41%/yr
confidence interval:
-0.53 to -0.23 %/yr
Annual degradation (%)

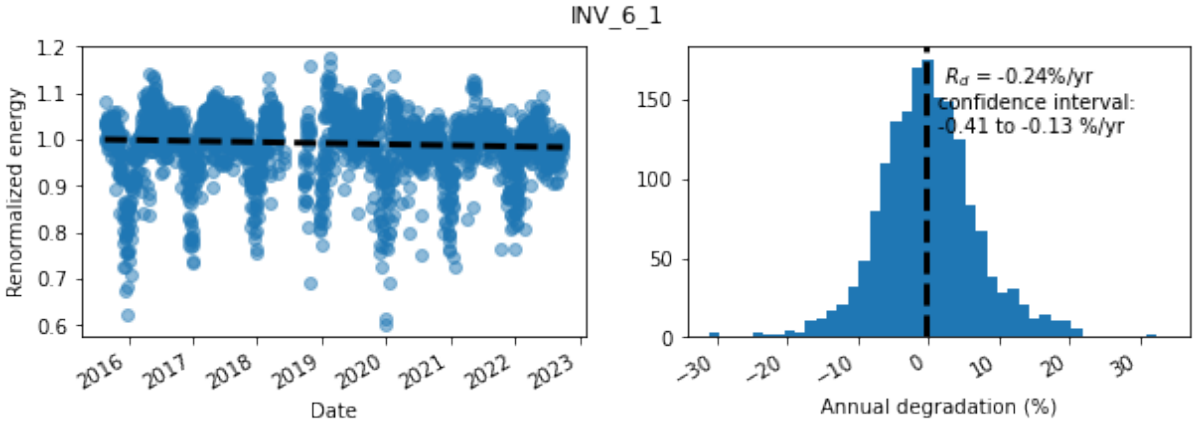
INV_6_1
Renormalized energy
Date
R_d = -0.24%/yr
confidence interval:
-0.41 to -0.13 %/yr
Annual degradation (%)

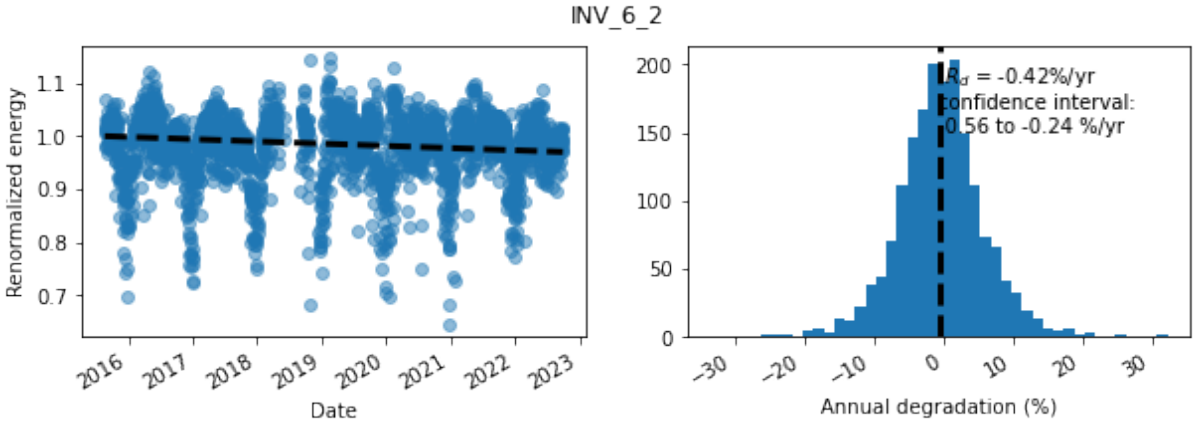
INV_6_2
Renormalized energy
Date
R_d = -0.42%/yr
confidence interval:
-0.56 to -0.24 %/yr
Annual degradation (%)

A.1.2 Detailed analysis

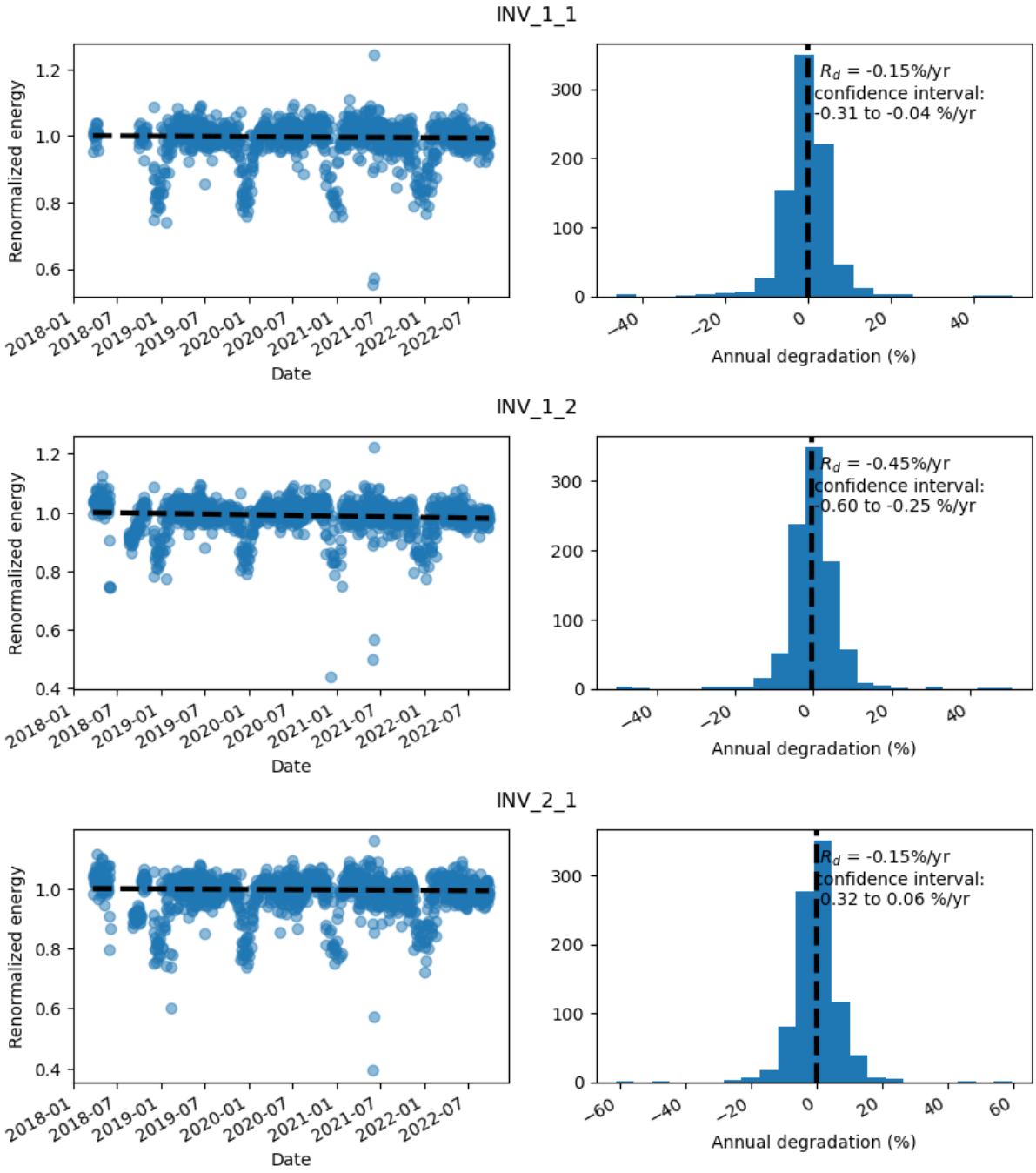

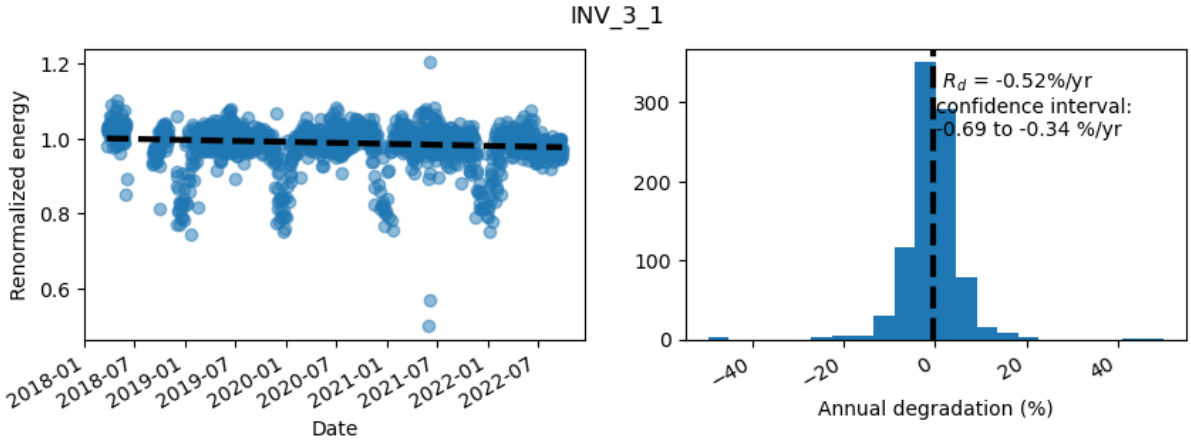
INV_3_1
Renormalized energy
Date
R_d = -0.52%/yr
confidence interval:
-0.69 to -0.34 %/yr
Annual degradation (%)

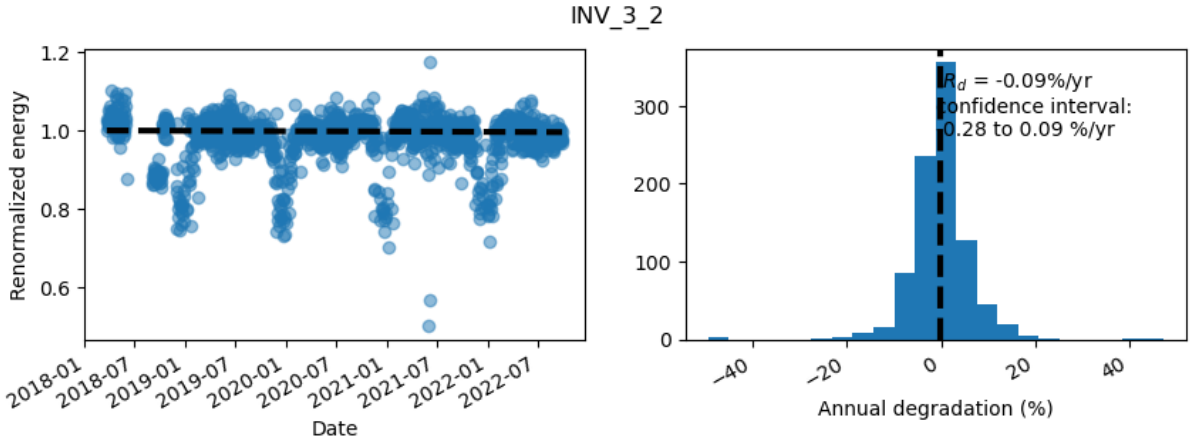
INV_3_2
Renormalized energy
Date
R_d = -0.09%/yr
confidence interval:
-0.28 to 0.09 %/yr
Annual degradation (%)

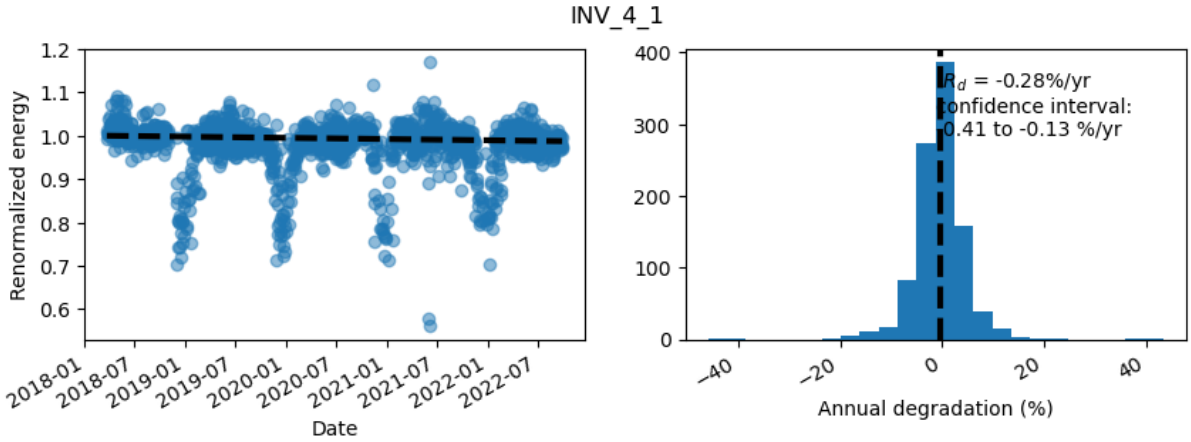
INV_4_1
Renormalized energy
Date
R_d = -0.28%/yr
confidence interval:
-0.41 to -0.13 %/yr
Annual degradation (%)

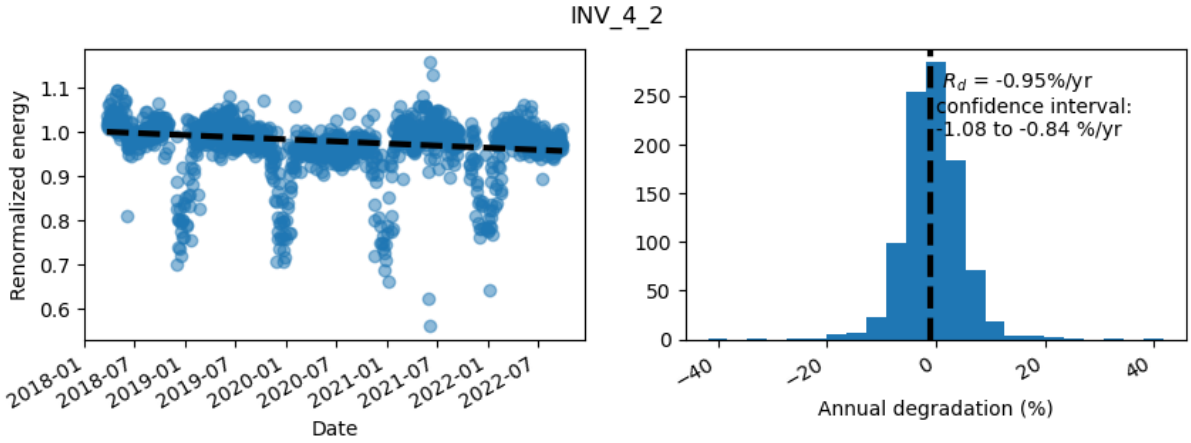
INV_4_2
Renormalized energy
Date
R_d = -0.95%/yr
confidence interval:
-1.08 to -0.84 %/yr
Annual degradation (%)

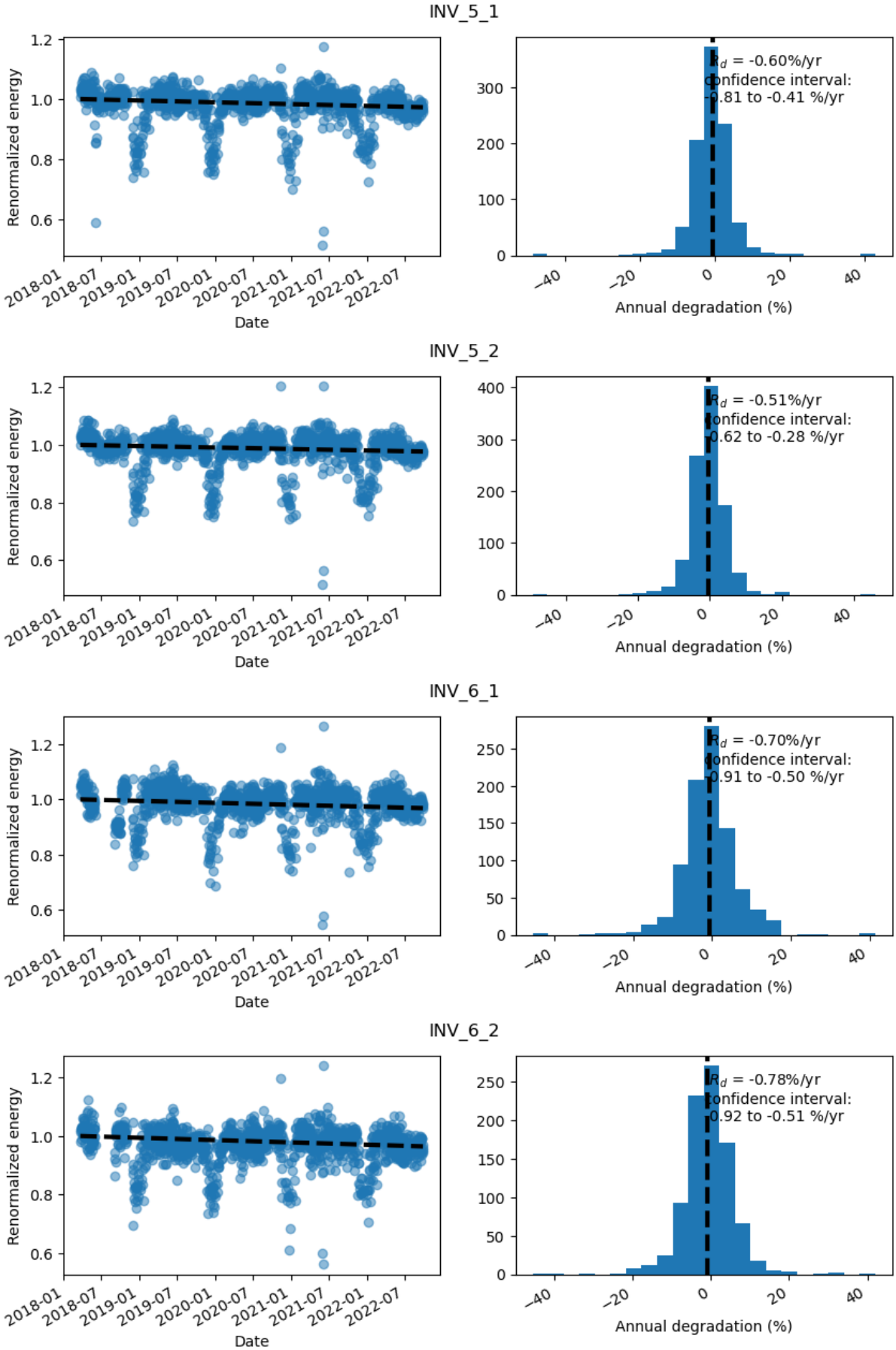
INV_5_1
Renormalized energy
Date
R_d = -0.60%/yr
Confidence interval:
-0.81 to -0.41 %/yr
Annual degradation (%)
INV_5_2
Renormalized energy
Date
R_d = -0.51%/yr
Confidence interval:
-0.62 to -0.28 %/yr
Annual degradation (%)
INV_6_1
Renormalized energy
Date
R_d = -0.70%/yr
Confidence interval:
-0.91 to -0.50 %/yr
Annual degradation (%)
INV_6_2
Renormalized energy
Date
R_d = -0.78%/yr
Confidence interval:
-0.92 to -0.51 %/yr
Annual degradation (%)

A.2 System B

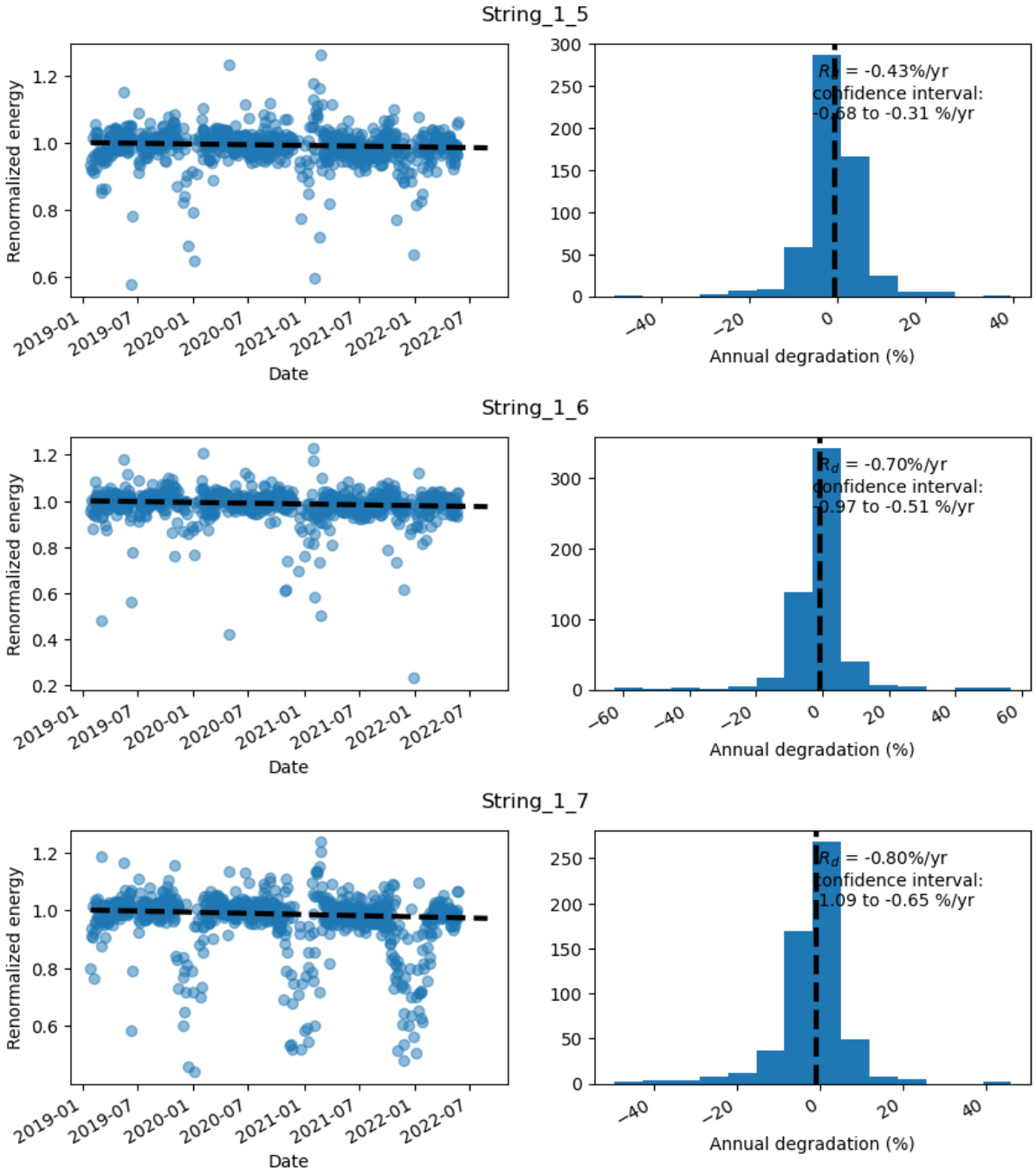
String_1_5
Renormalized energy
Date
Annual degradation (%)
R_d = -0.43%/yr
confidence interval:
-0.68 to -0.31 %/yr
String_1_6
Renormalized energy
Date
Annual degradation (%)
R_d = -0.70%/yr
confidence interval:
-0.97 to -0.51 %/yr
String_1_7
Renormalized energy
Date
Annual degradation (%)
R_d = -0.80%/yr
confidence interval:
-1.09 to -0.65 %/yr

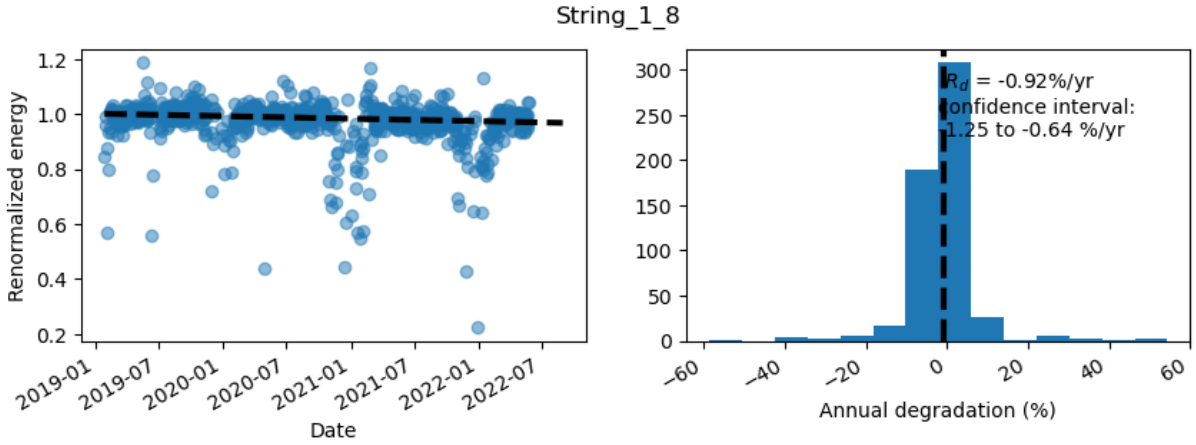
String_1_8
Renormalized energy
Date
R_d = -0.92%/yr
confidence interval:
-1.25 to -0.64 %/yr
Annual degradation (%)

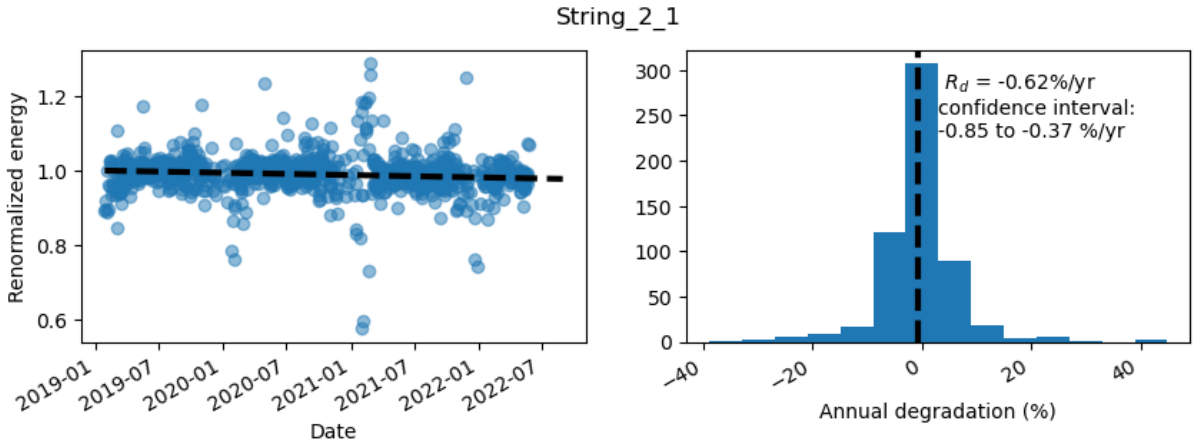
String_2_1
Renormalized energy
Date
R_d = -0.62%/yr
confidence interval:
-0.85 to -0.37 %/yr
Annual degradation (%)

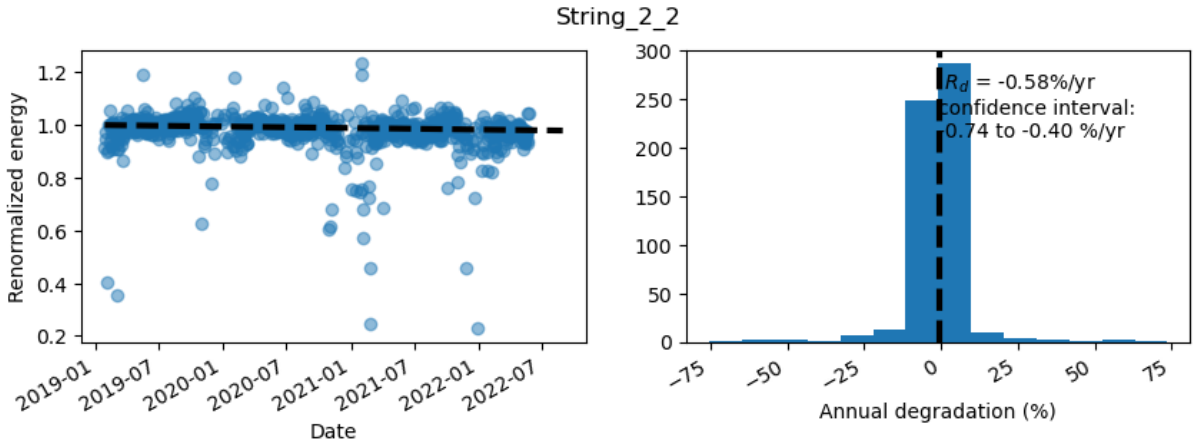
String_2_2
Renormalized energy
Date
R_d = -0.58%/yr
confidence interval:
-0.74 to -0.40 %/yr
Annual degradation (%)

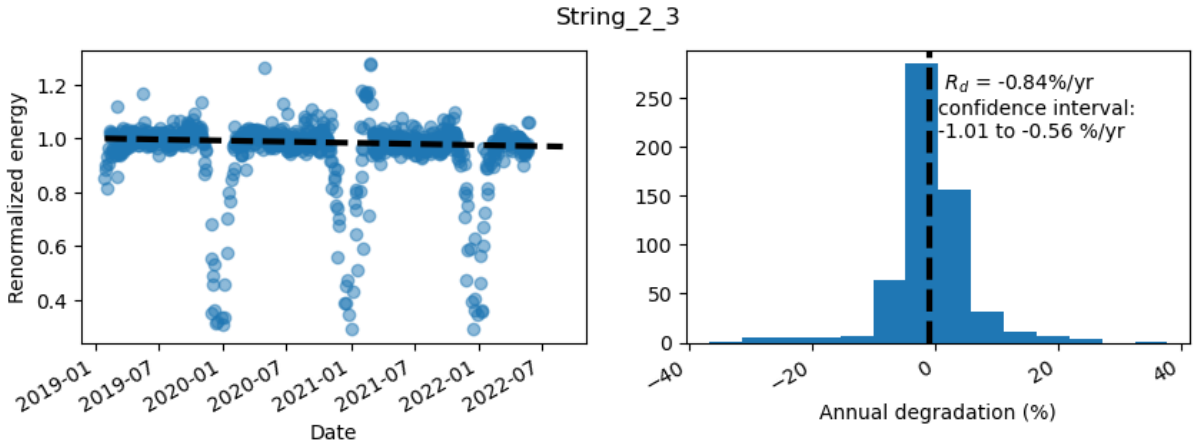
String_2_3
Renormalized energy
Date
R_d = -0.84%/yr
confidence interval:
-1.01 to -0.56 %/yr
Annual degradation (%)

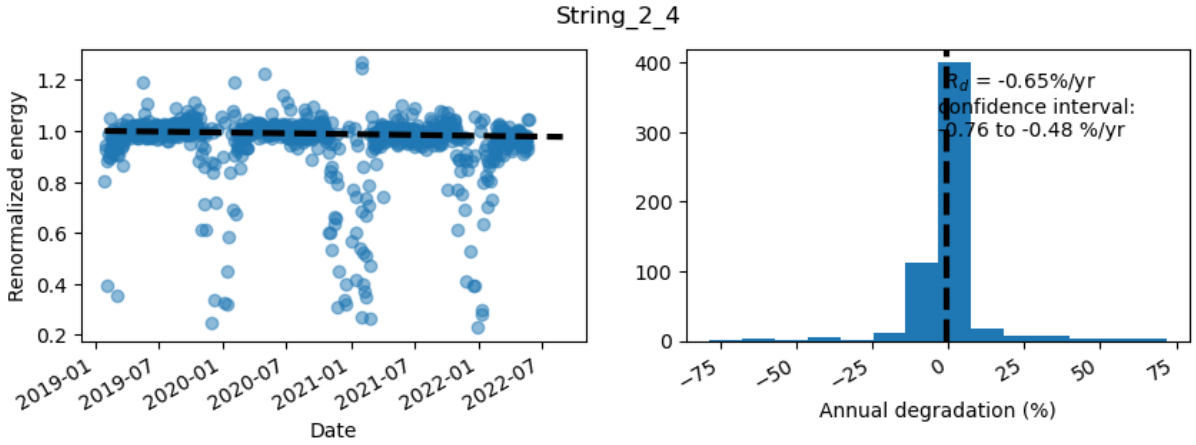
String_2_4
Renormalized energy
Date
R_d = -0.65%/yr
confidence interval:
-0.76 to -0.48 %/yr
Annual degradation (%)

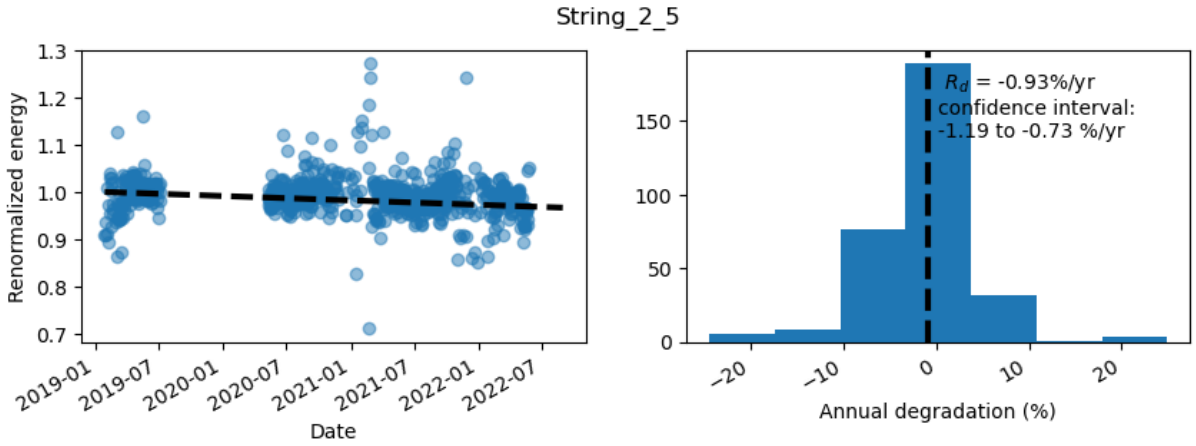
String_2_5
Renormalized energy
Date
R_d = -0.93%/yr
confidence interval:
-1.19 to -0.73 %/yr
Annual degradation (%)

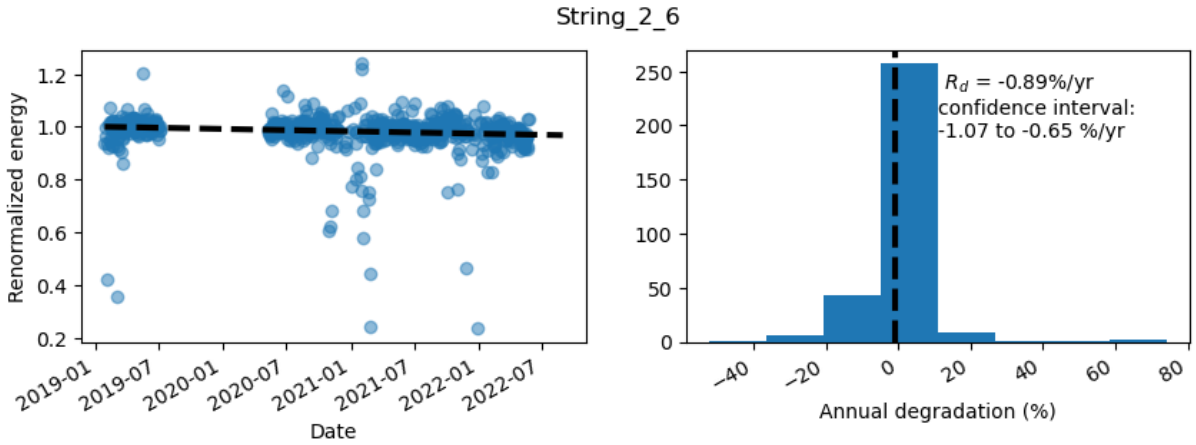
String_2_6
Renormalized energy
Date
R_d = -0.89%/yr
confidence interval:
-1.07 to -0.65 %/yr
Annual degradation (%)

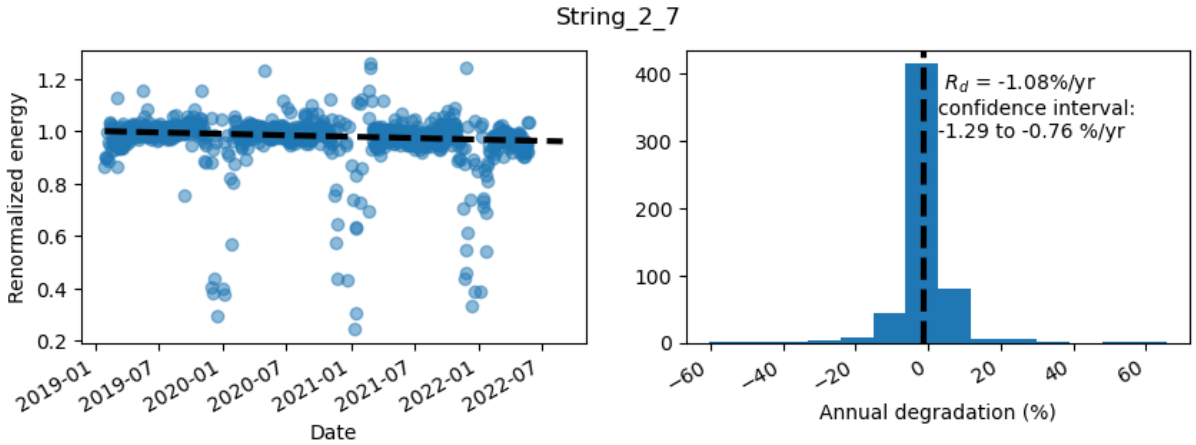
String_2_7
Renormalized energy
Date
R_d = -1.08%/yr
confidence interval:
-1.29 to -0.76 %/yr
Annual degradation (%)

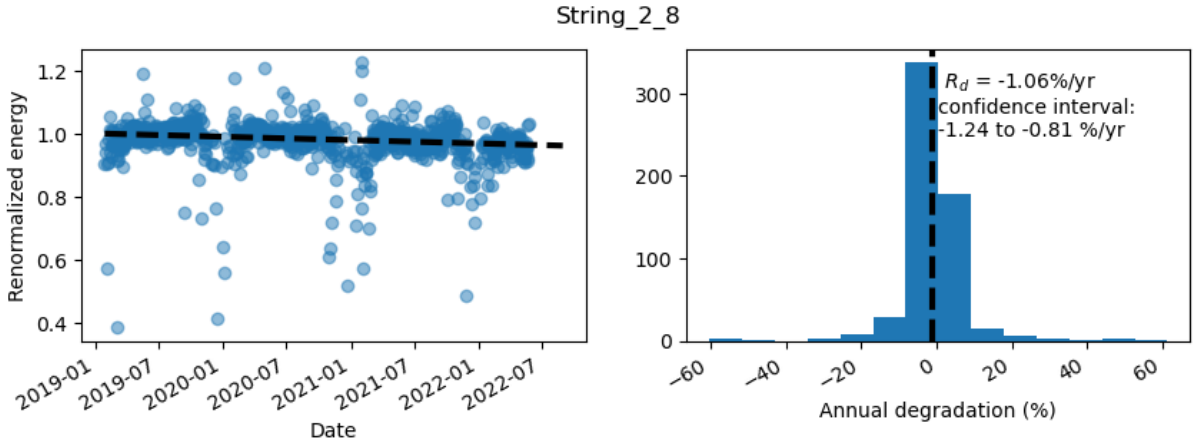
String_2_8
Renormalized energy
Date
R_d = -1.06%/yr
confidence interval:
-1.24 to -0.81 %/yr
Annual degradation (%)

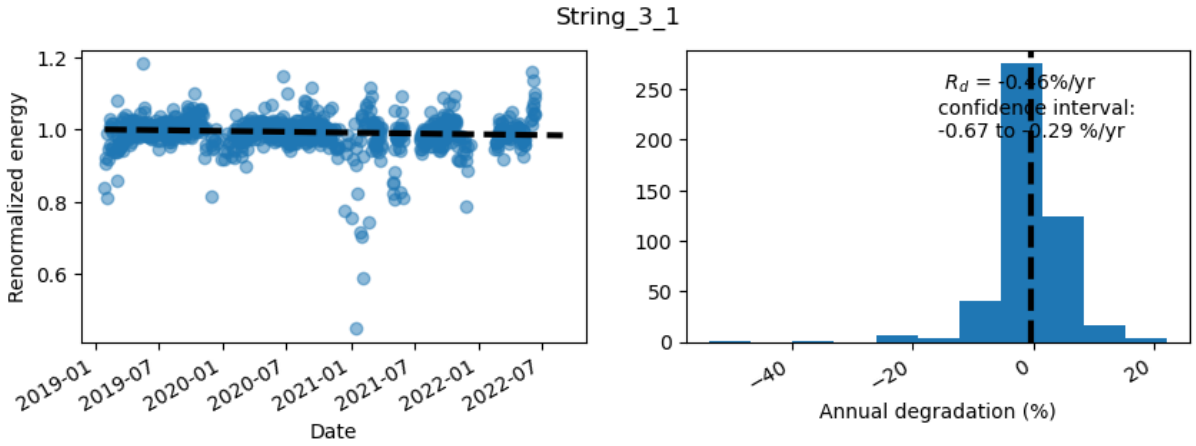
String_3_1
Renormalized energy
Date
R_d = -0.46%/yr
confidence interval:
-0.67 to -0.29 %/yr
Annual degradation (%)

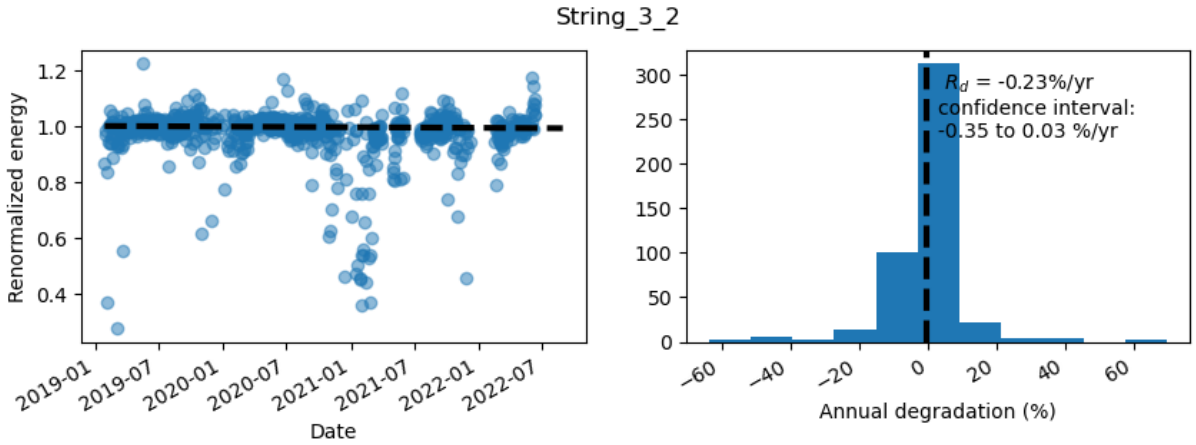
String_3_2
Renormalized energy
Date
R_d = -0.23%/yr
confidence interval:
-0.35 to 0.03 %/yr
Annual degradation (%)

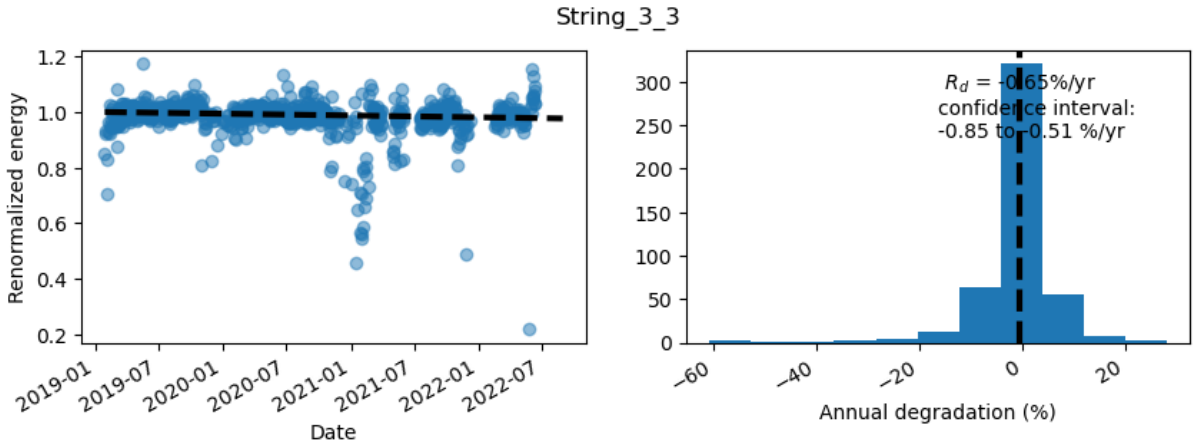
String_3_3
Renormalized energy
Date
R_d = -0.65%/yr
confidence interval:
-0.85 to -0.51 %/yr
Annual degradation (%)

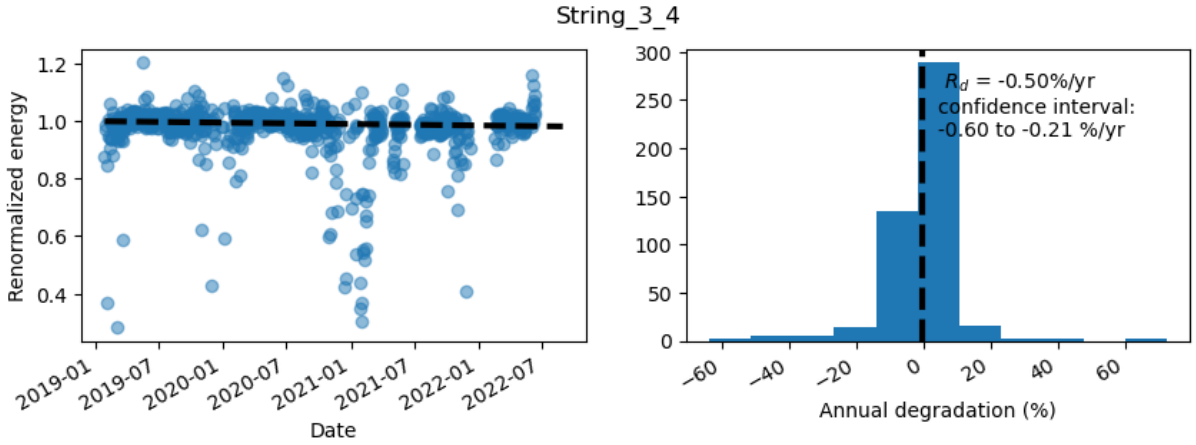
String_3_4
Renormalized energy
Date
R_d = -0.50%/yr
confidence interval:
-0.60 to -0.21 %/yr
Annual degradation (%)

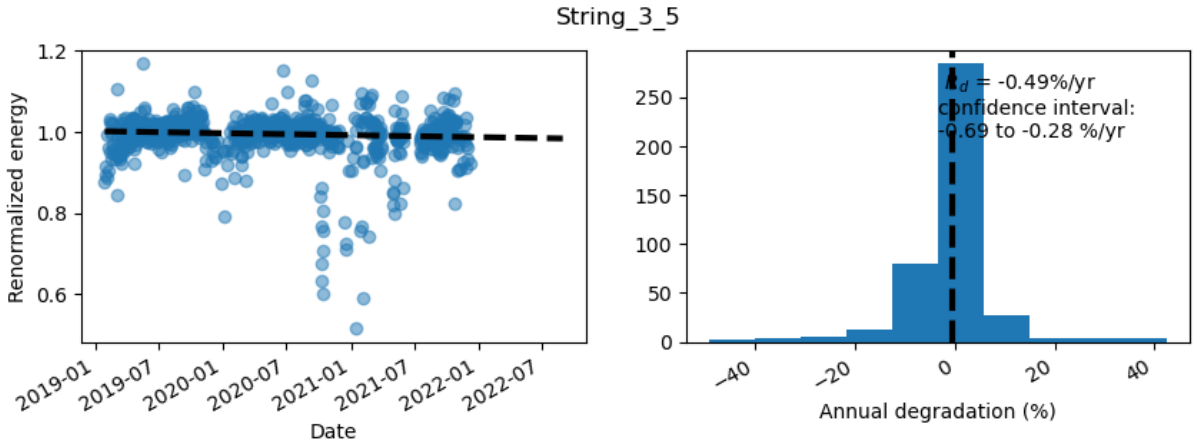
String_3_5
Renormalized energy
Date
R_d = -0.49%/yr
confidence interval:
-0.69 to -0.28 %/yr
Annual degradation (%)

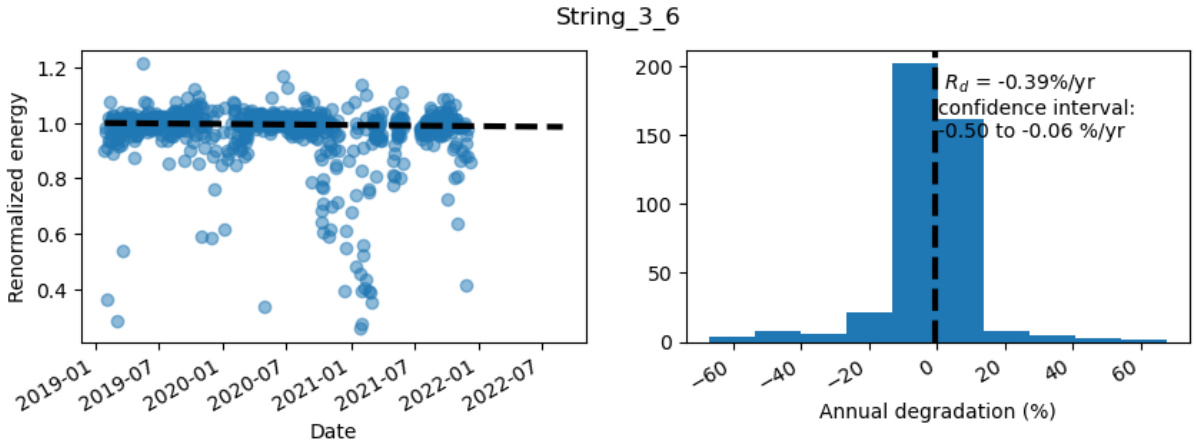
String_3_6
Renormalized energy
Date
R_d = -0.39%/yr
confidence interval:
-0.50 to -0.06 %/yr
Annual degradation (%)

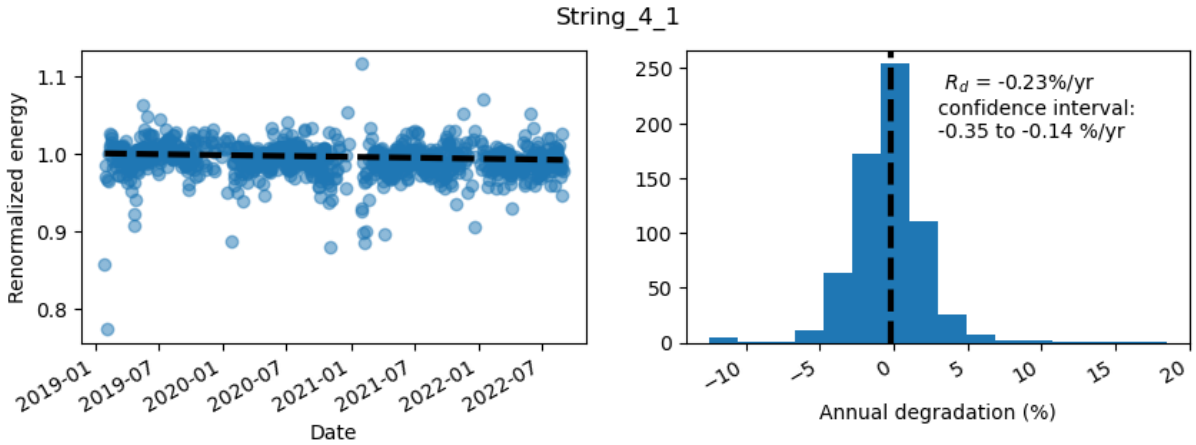
String_4_1
Renormalized energy
Date
R_d = -0.23%/yr
confidence interval:
-0.35 to -0.14 %/yr
Annual degradation (%)

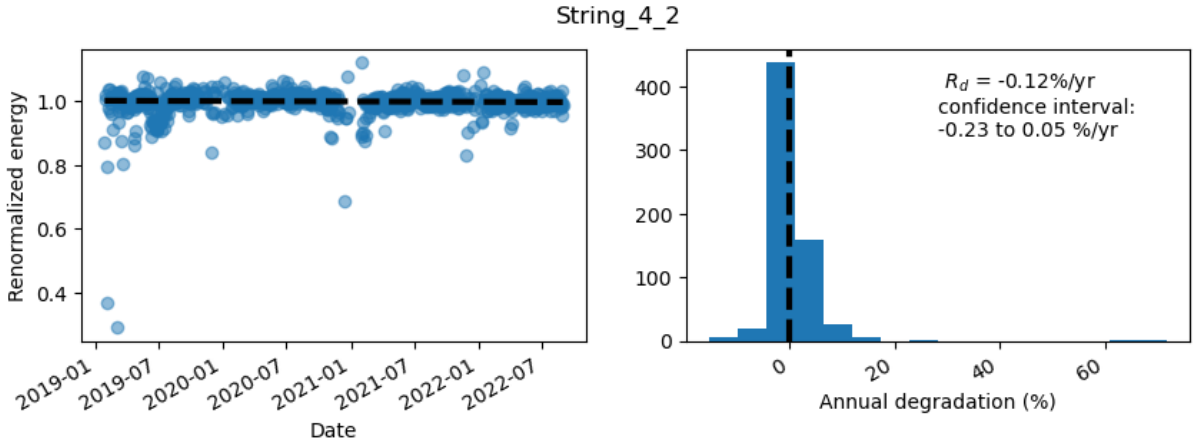
String_4_2
Renormalized energy
Date
R_d = -0.12%/yr
confidence interval:
-0.23 to 0.05 %/yr
Annual degradation (%)

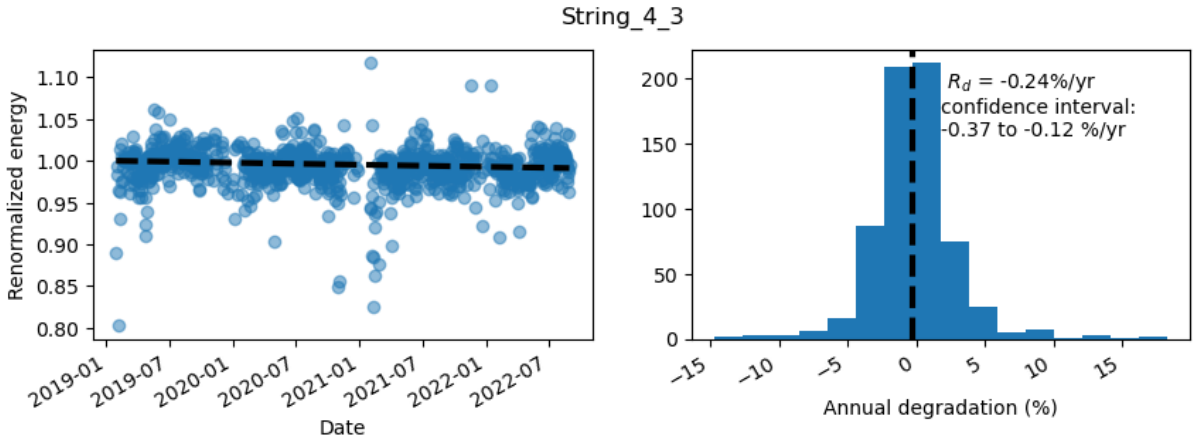
String_4_3
Renormalized energy
Date
R_d = -0.24%/yr
confidence interval:
-0.37 to -0.12 %/yr
Annual degradation (%)

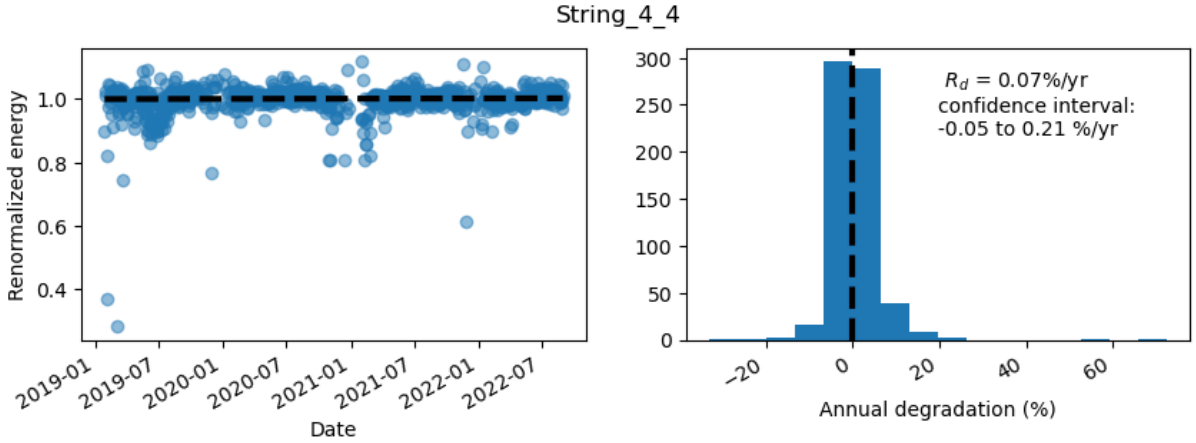
String_4_4
Renormalized energy
Date
R_d = 0.07%/yr
confidence interval:
-0.05 to 0.21 %/yr
Annual degradation (%)

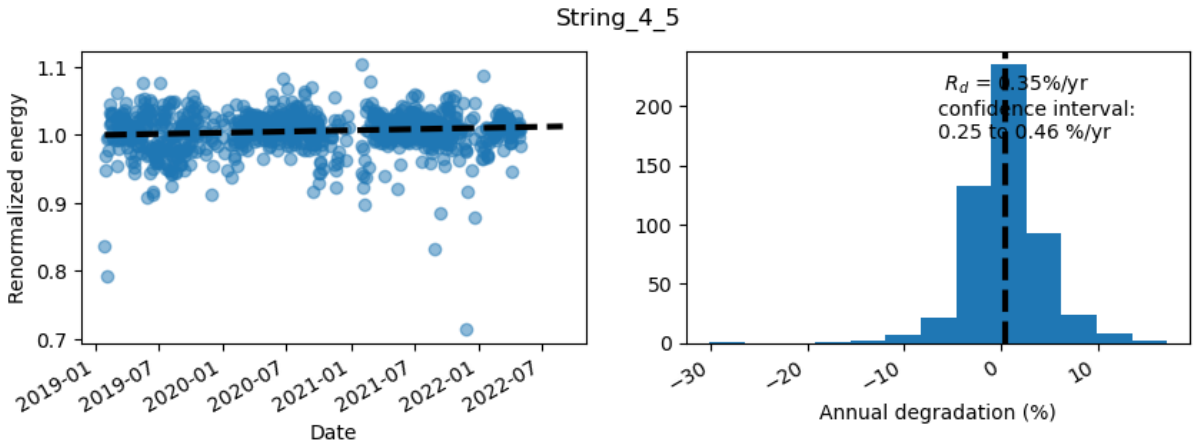
String_4_5
Renormalized energy
Date
R_d = 0.35%/yr
confidence interval:
0.25 to 0.46 %/yr
Annual degradation (%)

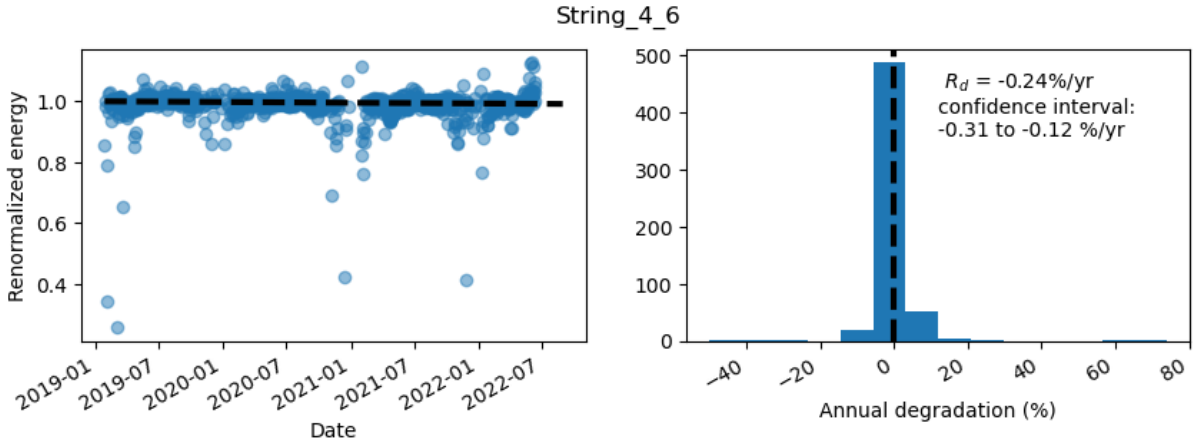
String_4_6
Renormalized energy
Date
Annual degradation (%)
R_d = -0.24%/yr
confidence interval:
-0.31 to -0.12 %/yr

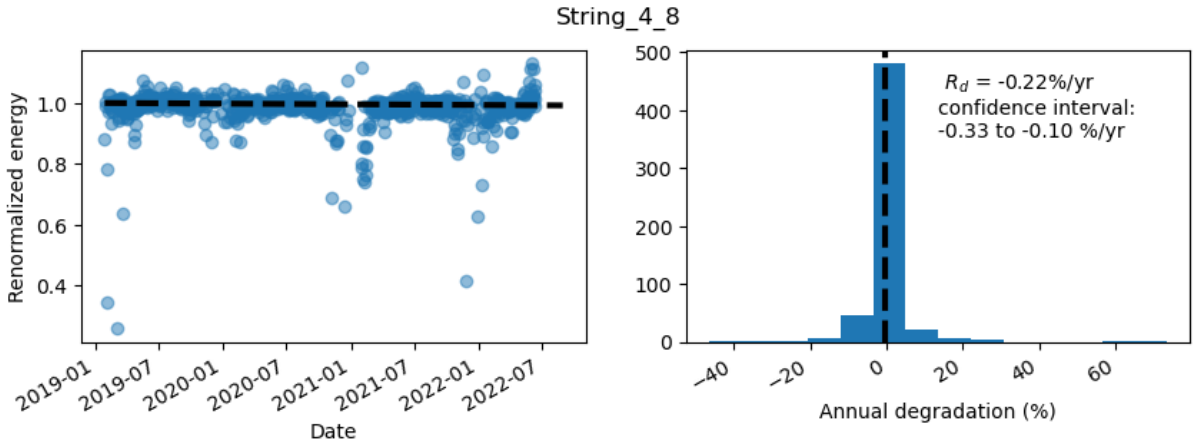
String_4_8
Renormalized energy
Date
Annual degradation (%)
R_d = -0.22%/yr
confidence interval:
-0.33 to -0.10 %/yr

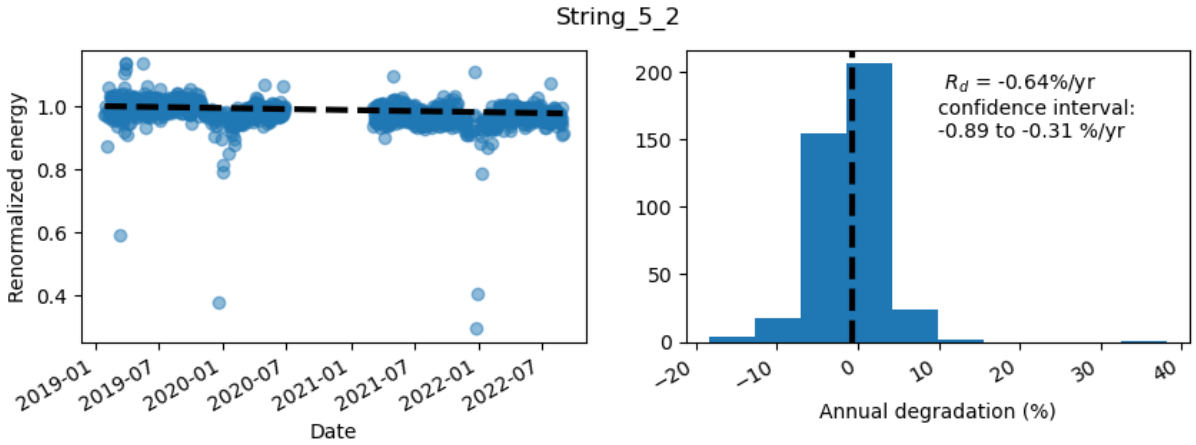
String_5_2
Renormalized energy
Date
Annual degradation (%)
R_d = -0.64%/yr
confidence interval:
-0.89 to -0.31 %/yr

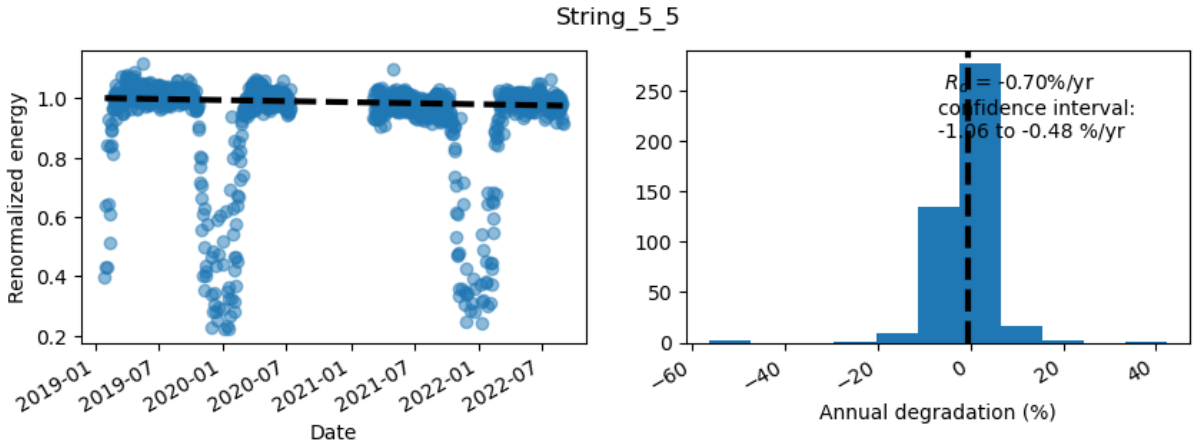
String_5_5
Renormalized energy
Date
Annual degradation (%)
R_d = -0.70%/yr
confidence interval:
-1.06 to -0.48 %/yr

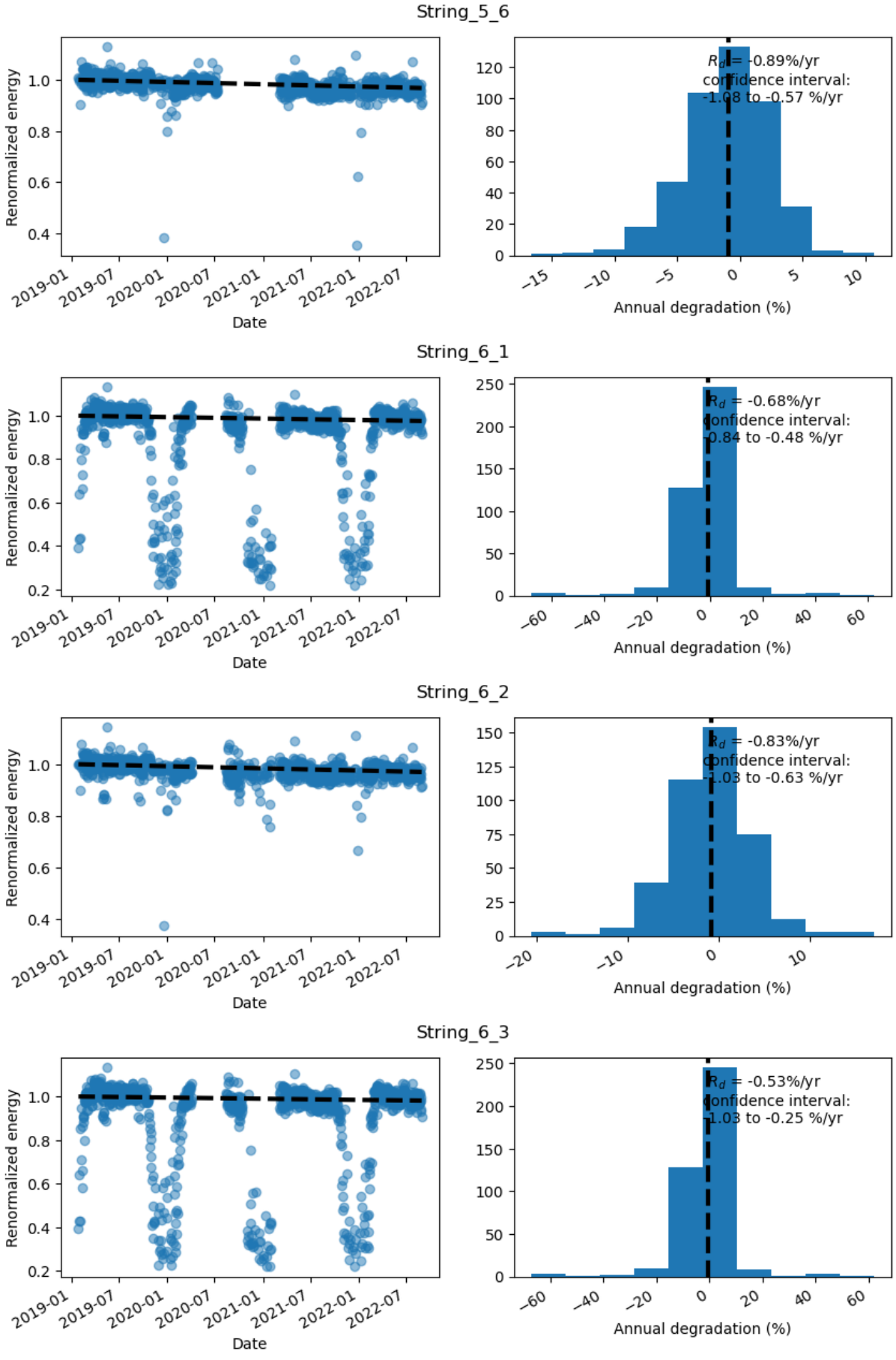
String_5_6
Renormalized energy
Date
R_d = -0.89%/yr
confidence interval:
-1.08 to -0.57 %/yr
Annual degradation (%)
String_6_1
Renormalized energy
Date
R_d = -0.68%/yr
confidence interval:
-0.84 to -0.48 %/yr
Annual degradation (%)
String_6_2
Renormalized energy
Date
R_d = -0.83%/yr
confidence interval:
-1.03 to -0.63 %/yr
Annual degradation (%)
String_6_3
Renormalized energy
Date
R_d = -0.53%/yr
confidence interval:
-1.03 to -0.25 %/yr
Annual degradation (%)

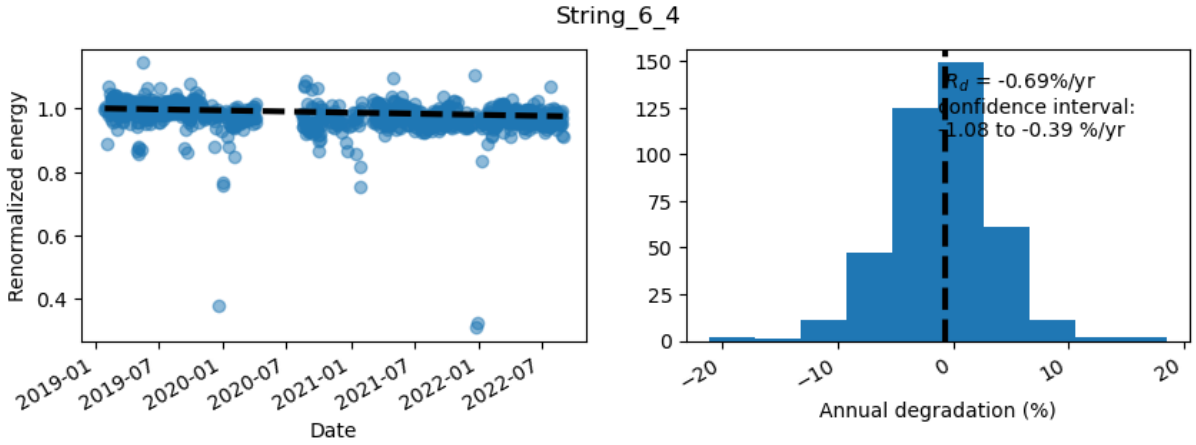
String_6_4
Renormalized energy
Date
R_d = -0.69%/yr
confidence interval:
-1.08 to -0.39 %/yr
Annual degradation (%)

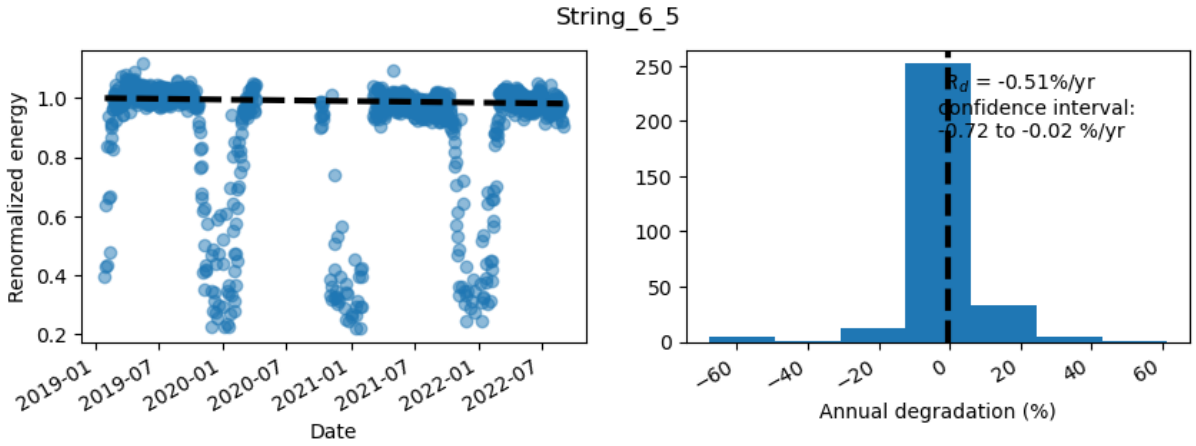
String_6_5
Renormalized energy
Date
R_d = -0.51%/yr
confidence interval:
-0.72 to -0.02 %/yr
Annual degradation (%)

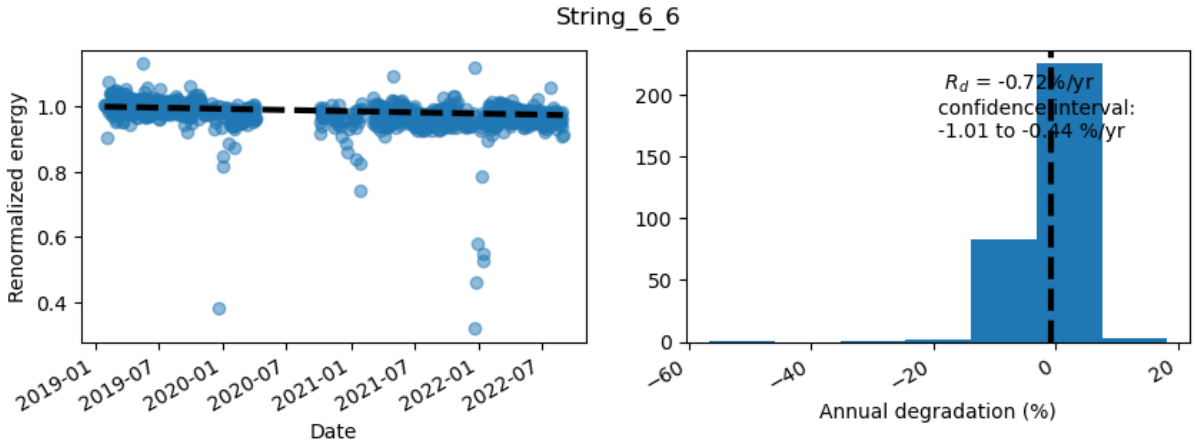
String_6_6
Renormalized energy
Date
R_d = -0.72%/yr
confidence interval:
-1.01 to -0.44 %/yr
Annual degradation (%)

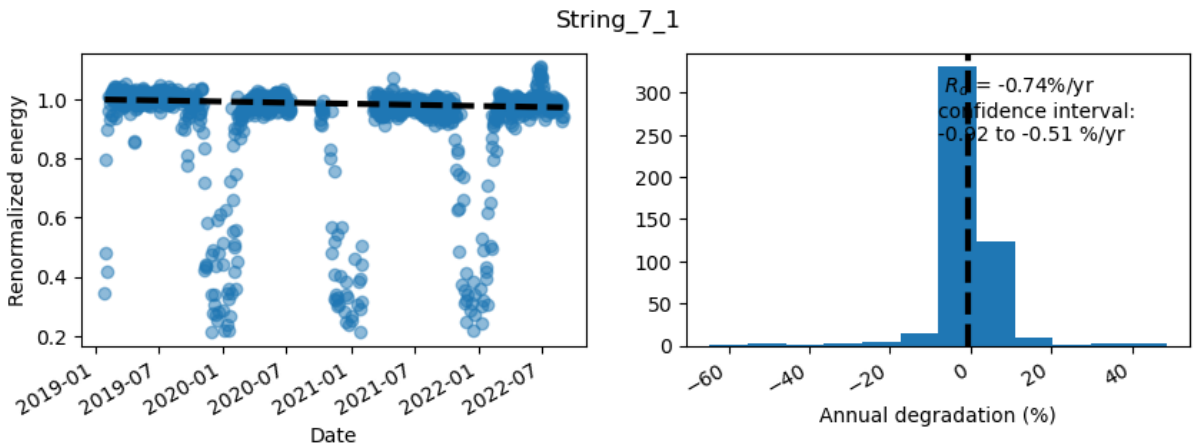
String_7_1
Renormalized energy
Date
R_d = -0.74%/yr
confidence interval:
-0.92 to -0.51 %/yr
Annual degradation (%)

String_7_2

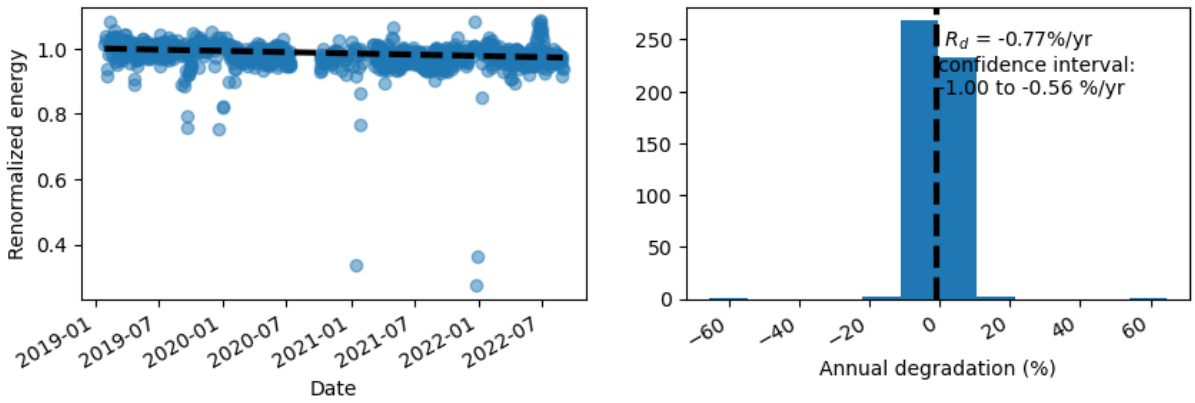

String_7_3

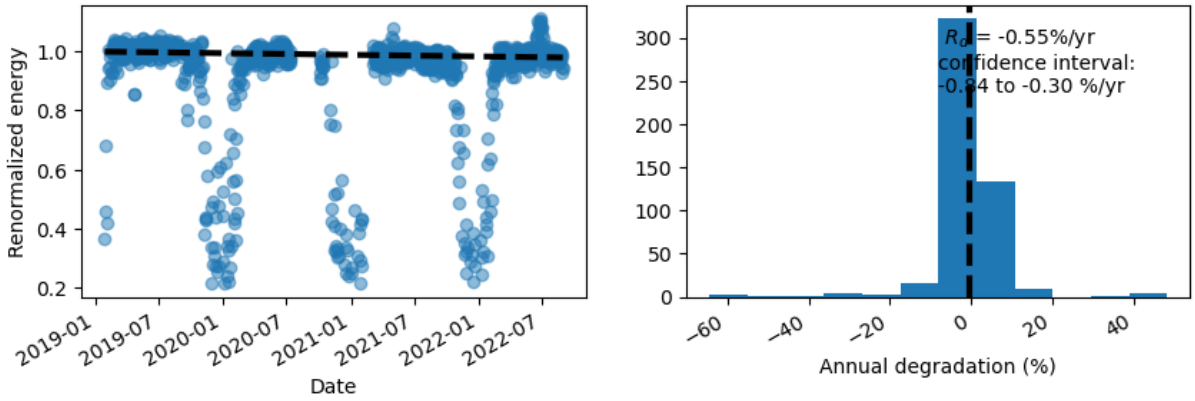

String_7_4

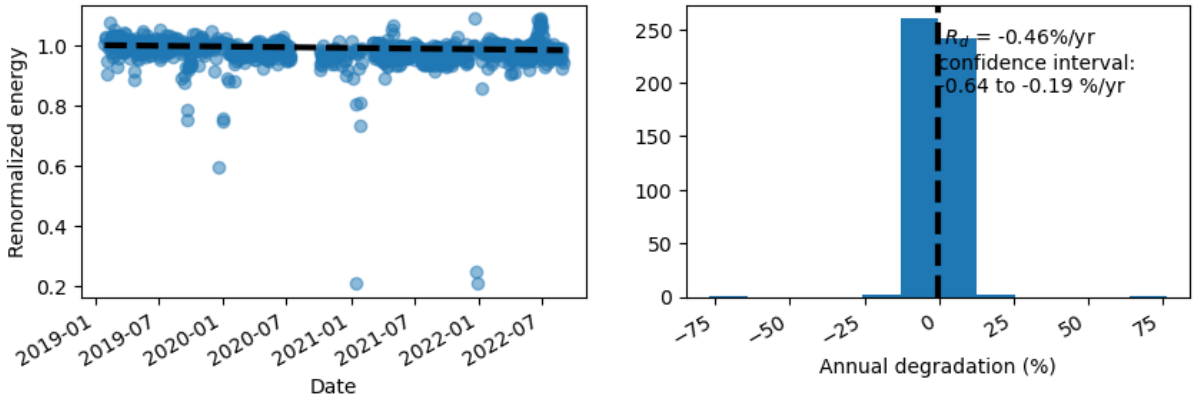

String_7_5

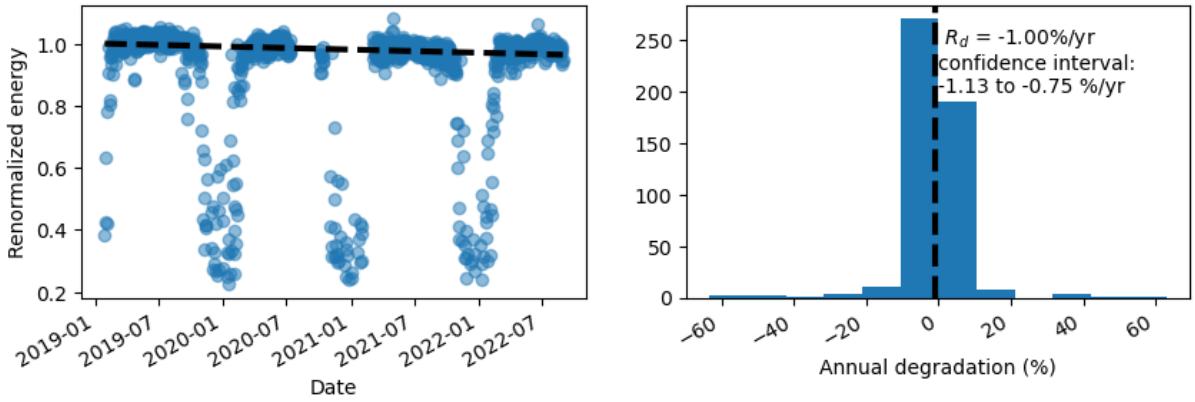

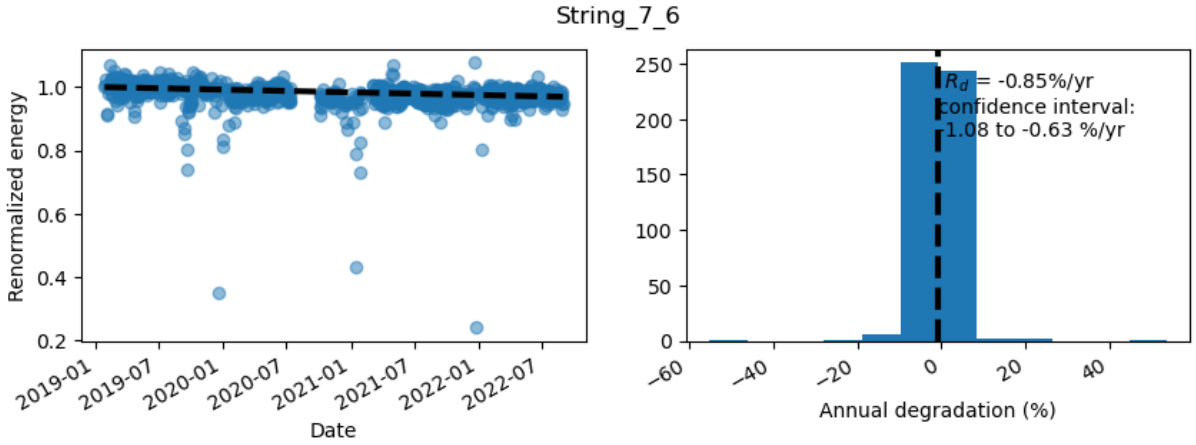
String_7_6
Renormalized energy
1.0
0.8
0.6
0.4
0.2
2019-01
2019-07
2020-01
2020-07
2021-01
2021-07
2022-01
2022-07
Date
250
200
150
100
50
0
−60
−40
−20
0
20
40
R_d = -0.85%/yr
confidence interval:
-1.08 to -0.63 %/yr
Annual degradation (%)

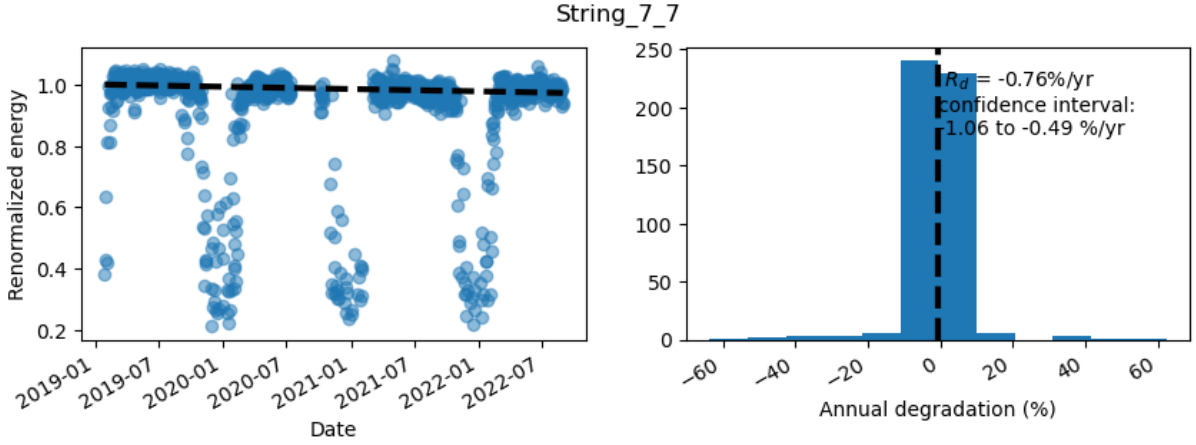
String_7_7
Renormalized energy
1.0
0.8
0.6
0.4
0.2
2019-01
2019-07
2020-01
2020-07
2021-01
2021-07
2022-01
2022-07
Date
250
200
150
100
50
0
−60
−40
−20
0
20
40
60
R_d = -0.76%/yr
confidence interval:
-1.06 to -0.49 %/yr
Annual degradation (%)

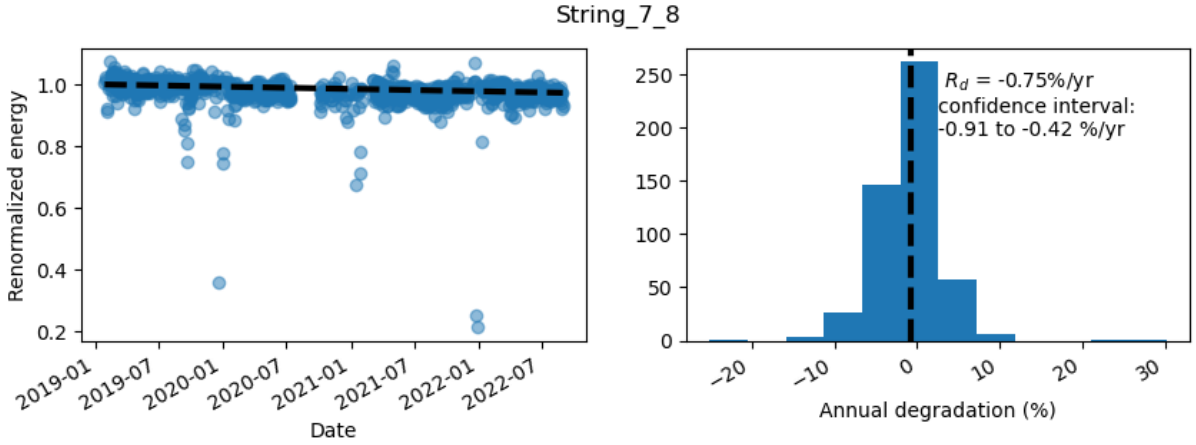
String_7_8
Renormalized energy
1.0
0.8
0.6
0.4
0.2
2019-01
2019-07
2020-01
2020-07
2021-01
2021-07
2022-01
2022-07
Date
250
200
150
100
50
0
−20
−10
0
10
20
30
R_d = -0.75%/yr
confidence interval:
-0.91 to -0.42 %/yr
Annual degradation (%)

Technical
University of
Denmark

Ørsteds Plads Building 348
2800 Kgs. Lyngby

www.elektro.dtu.dk/